Composite PEGDA Scaffolds for UV-Bioprinting of Decellularized Plant Cells

Rose Boudria

Ottawa-Carleton Institute for Biology

University of Ottawa

Ottawa, Canada

Faculty of Science

Department of Biology

July, 2024

ABSTRACT

Regenerative medicine for tissue repair is an important and intensive area of research. The ultimate goal of regenerative medicine is to repair or replace tissues in patients who have suffered from traumatic accidents or degenerative diseases, often by utilizing biomaterial scaffolds or matrices to direct or stimulate cell growth. There are numerous approaches to producing 3D matrices that support the growth of mammalian cells. One method of creating a biomaterial scaffold is through the use of decellularized plant cells. Decellularization is the process of removing all the cells from plant tissue, leaving behind a cellulosic scaffold that involves cellulose, hemicellulose, pectin and lignin. The Pelling lab has previously demonstrated that natural plant-derived cellulose scaffolds can be produced by employing common decellularization approaches, which support 3D cell culture. Here, we focus on bringing together plant decellularization techniques with 3D bioprinting to create decellularized plant scaffolds with controllable architectures. More specifically, this project focuses on the decellularization of the BY-2 cell line, a Japanese line that originates from the tobacco plant. The resulting cellulose is then mixed with polyethylene glycol diacrylate (PEGDA), to create a biocompatible ink, which can be incorporated into the Lumen-X 3D bio-printer. Scaffolds are then custom printed, offering a versatility of possible scaffold shapes and pore sizes, making them suitable for different applications in tissue engineering. Additionally, our goal is to show that mammalian cells can successfully attach to and colonize these scaffolds. We specifically used NIH 3t3 fibroblast cells because they are well-established and widely used models for studying cell attachment, proliferation, and tissue formation. Their robust and consistent growth characteristics make them ideal for evaluating the biocompatibility of novel biomaterials like the plant-derived scaffolds. If successful, these structures could be a great support for newly formed tissues in the receiving organism. In our *in vivo* study, we implemented these scaffolds, 1 cm in length and 3mm in thickness, subcutaneously in rats at three different time points: 4 weeks, 8 weeks, and 12 weeks. This study aims to further demonstrate the potential of these plant-derived scaffolds in regenerative medicine, particularly in tissue repair and regeneration.

ACKNOWLEDGMENT

Firstly, I would like to extend my heartfelt gratitude to Dr. Andrew Pelling for welcoming me into his lab and for his mentorship throughout my academic journey. I am deeply grateful to Dr. Ziba Jaberansari for the opportunity to contribute to the Pelling Lab and for her pivotal leadership and support. Special thanks to Krystal Walker for her invaluable assistance with the animal study and thesis writing. Your expertise and encouragement have been immensely helpful.

I also appreciate my colleagues: Lauren Couvrette, Arman Bayat, Nicolette Mogilever, Dr. Maxime Leblanc Latour, Dr. Will Collins, and Dr. Aysegul Dede Eren, for their collaboration and support over the past three years. Each of you is a brilliant scientist with a bright future ahead!

Je tiens à exprimer ma plus profonde gratitude à mes parents, Paule et Dan, pour leur soutien infaillible tout au long de mes études. Les trajets quotidiens entre Sarsfield et le campus universitaire ont été longs, mais vos encouragements ont tout rendu possible. Je remercie également mes grands-parents, Don et Maryann Boudria, non seulement de m'avoir inspiré par leur générosité et leur Sagesse, mais aussi pour leur soutien financier, tout au long de mes études. Merci à mes frères, Michel et Simon, pour leur soutien et leur compréhension durant ce parcours. Merci d'avoir supporté les deux ans d'impatience de votre soeur. Votre présence a été une source de réconfort et de force!

Je suis profondément reconnaissante à mon petit ami, Guillaume, qui partage non seulement le même domaine que moi, mais qui a également été indispensable, en fournissant des idées pour mon projet. Son soutien, y compris pour la relecture de ma thèse, a été inestimable. Enfin, à mes meilleurs amis Skylar, Cassandra et Virginie, merci de croire en moi et d'être toujours là. Votre amitié a été une source de force et de motivation! 😊

TABLE OF CONTENTS

LIST OF FIGURES

LIST OF ABBREVIATIONS

- 3D- Three Dimensional
- PEGDA- Polyethylene Glycol Diacrylate
- UV- Ultraviolet
- BY-2- Tobacco Bright Yellow-2
- PBS- Phosphate-Buffered Saline
- SDS - Sodium dodecyl sulfate
- kPa – Kilopascal
- DNases – Deoxyribonuclease
- LAP – Photoinitor Lithium Phenyl-2,4,6-Trimethylbenzoylphosphinate
- $CaCl_2$ – Calcium Chloride
- PI – Propidium Iodide
- FOV – Fields of View
- FBS -Fetal bovine serum
- DMEM - Dulbecco's Modified Eagle's medium
- H&E – Hematoxylin and eosin
- MT – Masson's Trichrome

Chapter 1

Introduction to Plant Tissue Engineering

1.1 General Introduction

Regenerative medicine for tissue repair is an important and intense area of research[1]. The ultimate goal of regenerative medicine is to repair or replace tissues in patients who have suffered from traumatic accidents or degenerative diseases, often by utilizing biomaterial scaffolds or matrices to direct or stimulate cell growth[1]. There are numerous approaches for producing three-dimensional (3D) matrices that support the growth of mammalian cells [2].

3D matrices, also known as scaffolds, are essential for supporting the growth of cells by providing physical support. What makes these matrices truly remarkable is their ability to enable 3D cell culture, which more closely mimics the *in vivo* microenvironment compared to two-dimensional (2D) cell culture systems[3]. This is particularly relevant in tissue engineering and drug discovery, where a 3D cell culture system provides an ideal approach for developing scaffold-based constructs.

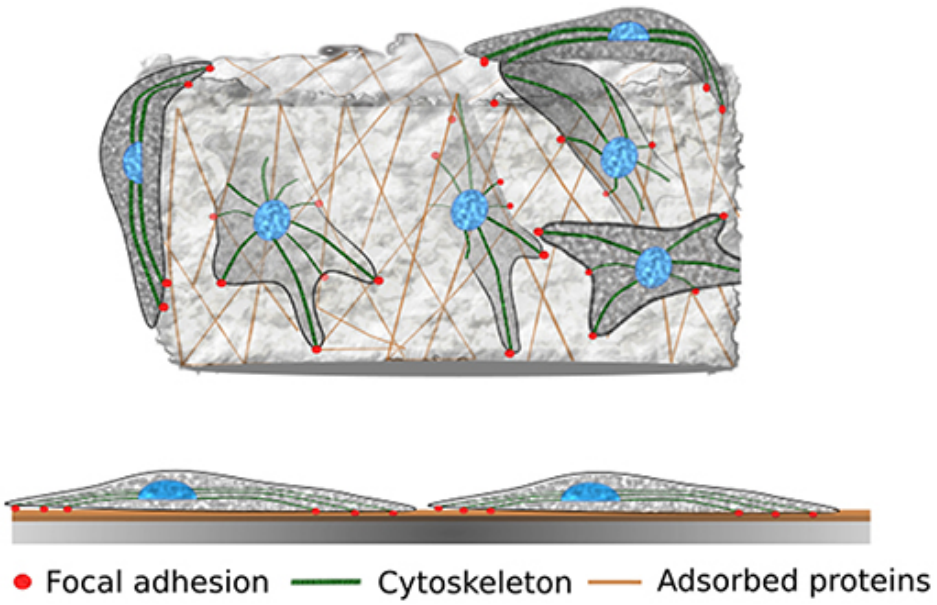

Figure 1: Exploring Cellular Behavior with a 3D Substrate vs. 2D Substrate.
This figure delves into the contrasting environments experienced by cells cultured on a 3D porous substrate vs. a conventional 2D substrate, exemplified by Petri dishes. On 3D porous substrates, cells inhabit both the surface and interior, offering a more realistic mimicry of in vivo conditions compared to the flat confines of Petri dishes. Essential proteins from animal serum or cellular secretion adhere to the substrate's surface, aiding cell adhesion. Through focal adhesion, cells establish connections with the substrate, with material properties such as stiffness, defined as the resistance of a material to deformation under applied force, influencing cellular behaviour and morphology. This visual depiction highlights the dynamic interplay between cellular physiology and substrate characteristics, shedding light on the intricacies of tissue culture environments. Reproduced from Campuzano and Pelling, 2019 with permission from *Frontiers in Sustainable Food Systems*.

These constructs have immense potential for disease modelling, regenerative medicine, and studying the stem cell niche. By using 3D cell culture systems, researchers have made significant advancements in these fields, providing invaluable insights into cellular processes, and paving the way for future innovation[4–7].

1.2 Introduction to Biomaterials

Biomaterials are used in biomedical applications such as drug delivery, tissue engineering, and medical implants. These materials must elicit an appropriate immune response from the host to be considered biocompatible[8]. To make this determination, the material's immunogenicity, carcinogenicity, and mineralization must be considered[9].

These materials serve as integral components in a multitude of biomedical applications, encompassing drug delivery systems, tissue engineering constructs, and medical implants[10,11]. The field of biomaterial science continues to drive innovation, with ongoing efforts focused on enhancing biocompatibility, tailoring material properties to specific applications, and exploring innovative fabrication techniques[12,13]. Researchers are dedicated to exploring navel fabrication techniques and navigating the intricate interplay between material characteristics and biological responses.

Biomaterials can be derived from either natural or synthetic sources, each presenting unique advantages and disadvantages[14]. Through these endeavours, the goal is to improve patient outcomes across diverse clinical settings.

1.2.1 Natural Biomaterials

Natural biomaterials are derived from natural sources such as animal tissues, plant tissues, and microorganisms. Polymers, made of alginate, gelatine, collagen, and many other materials have already been used[15]. Collagen, sourced from animals, is a good example of a bio-compatible material that has been used to promote nerve regeneration and to support the adhesion and proliferation of endothelial and smooth muscle cells, as well as tendons [16–18]. Alginate, extracted from brown seaweed, has found wide application in the development of an array of composites for tissue engineering, drug delivery, wound healing, cartilage repair bone regeneration, and cancer therapy. Its appeal lies in its mild gelation by inserting divalent cations (e.g., Ca^{2+})[19–22]. Furthermore, gelatin, a neutral protein derived from collagen hydrolysis[23], has also left its mark, particularly in bioprinting techniques, where gelatin-based systems aid in mimicking native tissue[24]. Silk fibroin is another natural biomaterial that has been used in the medical community. Its unique properties have led to its incorporation into medical implants, such as an injectable hydrogel, demonstrating remarkable potential in wound healing and tissue repair[25]. This versatile material holds promise for a range of applications, from reconstructive surgery to drug delivery systems, thanks to its biocompatibility. Additionally, Chitosan, a natural polymer derived from chitin, emerges as a compelling candidate for biomedical applications. Ongoing research explores its potential in diverse fields as a biomaterial, for use in skin regeneration, cartilage repair, gene delivery, sensors, treatment, and diagnosis of diseases like cancer and cell imaging[26–29].

Therefore, natural biomaterials play a significant role in the development of nervous system repair. They provide biochemical cues that guide cellular behaviour, promoting stem cell differentiation and axonal outgrowth. Among the array of biomaterials utilized, acellular tissue grafts, collagen, hyaluronan, fibrin, and agarose stand out, each contributing distinctively to the complex landscape of neural regeneration[30].

Cellulose stands as a vital cornerstone among natural biomaterials, celebrated for its widespread utility. It reigns supreme as the most abundant polymer on our planet, offering diverse

forms and functionalities[31]. In the realm of tissue engineering, cellulose-based biomaterials emerge as pivotal players, facilitating cellular adhesion while harnessing nanostructure to macroscale mechanical properties. This intricate interplay between nano and macro scales not only underscores cellulose's versatility but also enhances tissue functionality[32].

Furthermore, cellulose manifests in various forms, including those derived from bacteria such as Acetobacter and Gluconacetobacter species, which produce bacterial cellulose that has unique structural properties and high purity[33]. Bacterial cellulose finds applications as both a material component and a scaffold, particularly within the realm of biomedicine [34]. The advent of cellulose nanocrystals represents another great cellulose-based biomaterial where it is a groundbreaking innovation, with ongoing advancements in extraction methodologies and treatments aiming to meet the burgeoning demand for these materials at an industrial scale[31]. Carboxymethyl cellulose emerges as another stalwart within the cellulose pantheon, prized for its exceptional surface properties, mechanical strength, tunable hydrophilicity, and viscous properties[35,36]. Its widespread use underscores the profound impact cellulose derivatives continue to exert across diverse domains, propelling innovation and progress in materials science and beyond.

1.2.2 Synthetic Biomaterials

Synthetic biomaterials, on the other hand, are chemically synthesized in a laboratory[37]. They have the advantage of being tunable in terms of their properties and can be designed to meet specific mechanical requirements for targeted applications. Examples of synthetic biomaterials include poly (lactic-co-glycolic acid) (PLGA), poly (glycolic acid) (PGA), and polyethylene glycol (PEG)[38–40]. PLGA and PEG are excellent options for creating biocompatible and biodegradable polymeric devices that can be used for drug delivery purposes because they are polymers that can exhibit a wide range of erosion times, have tunable mechanical properties and are also FDA-approved[41]. Moreover, PEG can be utilized to bind with other molecules, thereby opening new avenues for various therapeutic applications[42].

The properties of biomaterials can vary greatly depending on their source and processing method. For example, polymers can have different mechanical properties depending on the source tissue or animal species. Processing methods such as crosslinking can also influence the mechanical properties of natural and synthetic biomaterials. Porosity is another important factor in biomaterial design, as it can affect cell attachment and growth[15].

1.3 Introduction to Plant Biomaterials

One method of creating a biomaterial scaffold is through the use of decellularized plant cells[43–45]. Decellularization is the process of removing all the cells from a tissue, leaving behind a cellulosic scaffold[46]. The scaffold is made up of mainly polysaccharides such as cellulose, hemicellulose, lignin, and pectin[47,48.] Cellulose and hemicellulose contribute to its strength and rigidity, providing structural support for cells to adhere and grow[49,50]. Lignin adds further stability and durability, enhancing the scaffold's ability to maintain its shape and integrity over time[51]. Pectin, meanwhile, promotes porosity within the scaffold, allowing for the exchange of nutrients, gases and waste products essential for cell proliferation[52,53]. After being shaped and processed, the scaffold can then be seeded with mammalian cells and cultured in vitro or implanted in vivo to

promote tissue repair and regeneration[54,55]. The use of plant-derived cellulosic scaffold has several potential advantages over animal-derived extracellular matrix, such as a lower risk of immune rejection.[43,54,56–59].

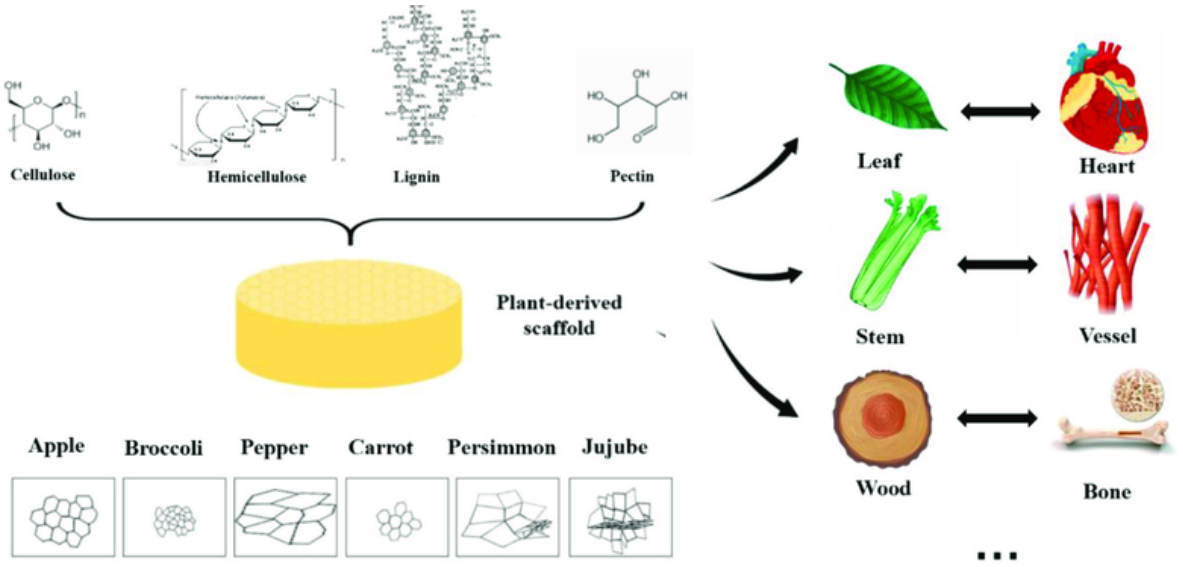

Figure 2: Composition of Decellularized Plants.
This figure depicts the structural composition of plants post-decellularization, highlighting the resemblance between plant scaffolds and human organs. The intricate network of pores and their sizes bear striking similarities to those found in biological tissues. Upon decellularization, plants yield a residual matrix comprising cellulose, hemicellulose, lignin, and pectin. Notably, variations in porosity and pore morphology among different plant species underscore their potential versatility in diverse applications, mirroring the diversity of organs they may emulate. Reproduced from Zhu and Lin, 2021 with permission from *Frontiers in Bioengineering and Biotechnology*.

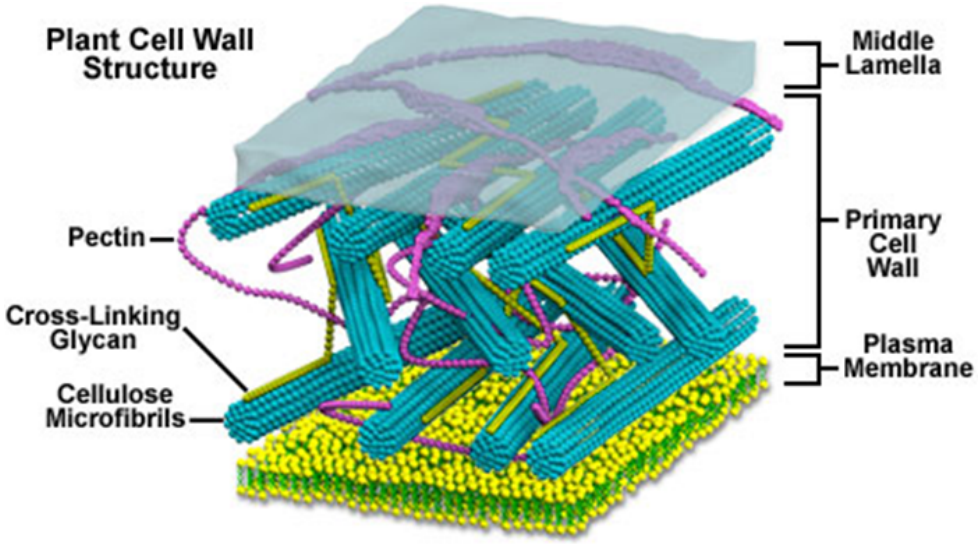

Figure 3: Plant Cell Wall Structure.
This schematic diagram illustrates the intricate architecture of the plant cell wall. The outermost layer, the Middle Lamella is primarily composed of pectin and acts as a glue between adjacent cells. Beneath it lies the Primary Cell Wall, which contains a complex network of cellulose microfibrils (blue) intertwined with cross-linking glycans (purple) and embedded in a matrix of pectins. The innermost layer, the Plasma Membrane, is depicted in yellow. The cellulose microfibrils provide structural support, while the cross-linking glycans and pectins contribute to the wall's flexibility and porosity. Reproduced from *Florida State University's Molecular Expressions Cell Biology Website.*

In tissue engineering within plant biology, one challenge is breaking down the cell wall while preserving the structural integrity of cellulose[60–62]. The plant cell wall is a complex structure composed of multiple layers, each with distinct biochemical components. The Middle Lamella, rich in pectin, provides adhesion between cells. The Primary Cell Wall, a composite of cellulose microfibrils, cross-linking glycans, and pectin, offers both strength and flexibility. The integrity of the cellulose microfibrils is crucial as they provide the main structural framework[63,64].

Plant-derived cellulosic scaffolds, a natural biomaterial, offer unique properties that make them particularly promising for regenerative medicine and tissue engineering[65]. These biomaterials are sustainable and environmentally friendly due to their renewable plant sources. The plant biomaterials also are highly biocompatible, as their natural composition includes mainly cellulose, which minimizes the risk of adverse immune responses[66]. These versatile biomaterials find

applications in various contexts, including wound healing, bone, and cartilage regeneration, and even organ transplantation, making them valuable resources for clinicians and researchers alike[67]. Challenges, such as fine-tuning mechanical properties and ensuring sterility, are areas of ongoing research, but the potential of plant-derived biomaterials to revolutionize tissue repair and regeneration is increasingly evident in the field of regenerative medicine[68]. The utilization of plants with diverse textures as matrices, techniques involving precision-cutting of specific shapes, or the creation of porosity scaffolds have all demonstrated efficacy but also present limitations. These constraints have spurred further exploration into alternative methods, such as bioprinting[69].

1.4 Introduction to Bioprinting

While decellularized plant-derived scaffolds have many benefits, the fixed geometry of such scaffolds is an important limitation[54,56]. Recently, 3D printing with biomaterials (bioprinting) has become a very popular tool for the creation of scaffolds with controlled shapes[70–72]. By using a specific type of 3D printer, a biomaterial scaffold can be created by printing layers of decellularized plant cells in a specific pattern to form the desired shape and size. Essentially, bioprinting is a process that involves layer-by-layer deposition of biologically formulated plant-derived cellulose ink. This method allows for precise control over the design and structure of the scaffold for different applications[73,74]. To maintain the structure of the scaffold, it is necessary to both customize it and reinforce it.

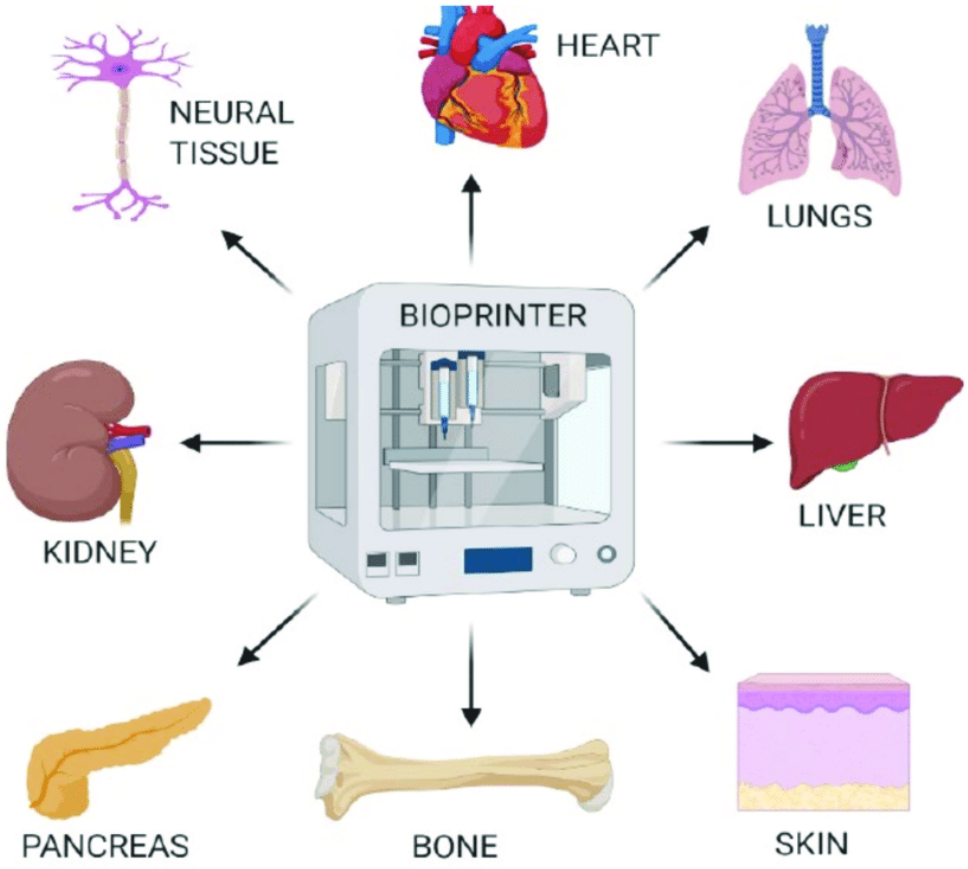

Figure 4: Demonstrating the Versatility of 3D-Bioprinting Technology in Crafting Diverse Tissue and Organ Designs.
Within this illustration, the profound adaptability of 3D-bioprinting technology is vividly depicted, showcasing its ability to intricately design and fabricate a wide array of tissues and organs using specialized bioink. Each design exemplifies the precision and customization achievable, underscoring the potential for revolutionizing regenerative therapies through tailored biomaterial fabrication. Reproduced from Vasanthan and Rajasingh, 2020 with permission from *Cells*.

With the multitude of approaches available for scaffold reinforcement, including the incorporation of reinforcing fibres, adjustments to scaffold architecture, utilization of nanostructured materials, integration of bioactive molecules, and the employment of crosslinking techniques, the field of tissue engineering offers a rich toolkit for tailoring scaffold properties to specific application needs[75,76]. Among these methods, crosslinking stands out as particularly promising for enhancing scaffold stability and mechanical strength, proving a versatile solution to address the diverse challenges encountered in tissue engineering endeavours.

1.4.1 Crosslinking 3D Bioprinter

We are focused on combining plant decellularization techniques with 3D bioprinting to create decellularized plant scaffolds with controllable architectures. Crosslinking is a method that is utilized a lot in bioprinting to fortify scaffolds, offering numerous approaches such as alginate and calcium chloride, which form stable crosslinks through ionic interactions[77]. Another notable method involves dynamic covalent inter-particle crosslinking, where covalent bonds are formed between microgel particles using hydrazone linkages[78]. Moreover, thermal crosslinking, an approach dependent on chemical processes, presents yet another avenue. This method achieved through the heating or cooling of polymer; holds promise for various applications. For instance, temperature-induced gelation with agarose emerges as particularly beneficial for fabricating hyaline cartilage[79].

Additionally, UV crosslinking offers an additional, highly effective covalent crosslinking method[80,81]. This involves using a biocompatible ink made by blending decellularized plant cells with polyethylene glycol diacrylate (PEGDA), which can be printed using ultraviolet (UV) curable technology. UV-crosslinking is a process in which a polymer is exposed to UV light to form covalent bonds between the polymer chains, resulting in a more stable and mechanically stronger material[82]. This process can be used to crosslink PEGDA, a water-soluble, biocompatible polymer, to create scaffolds[83]. One type of bioprinter is a 3D printing technology that can print and bond PEGDA using UV-crosslinking. By controlling the printing parameters and UV light intensity, the mechanical properties and pore size of the scaffolds can be optimized for specific tissue engineering applications. UV-crosslinking with PEGDA has been shown to be an effective method for creating mechanically stable scaffolds with high water retention, making it an attractive hydrogel[83–86].

Figure 5: Impact of UV Crosslinking on PEGDA Structure.

This figure illustrates the transformation of PEGDA from its liquid state to a scaffold structure following UV crosslinking within the bioprintner. The initial liquid stage of PEGDA is depicted alongside its post-crosslinking state under the influence of UV light within the printer, resulting in the formation of a scaffold shape.

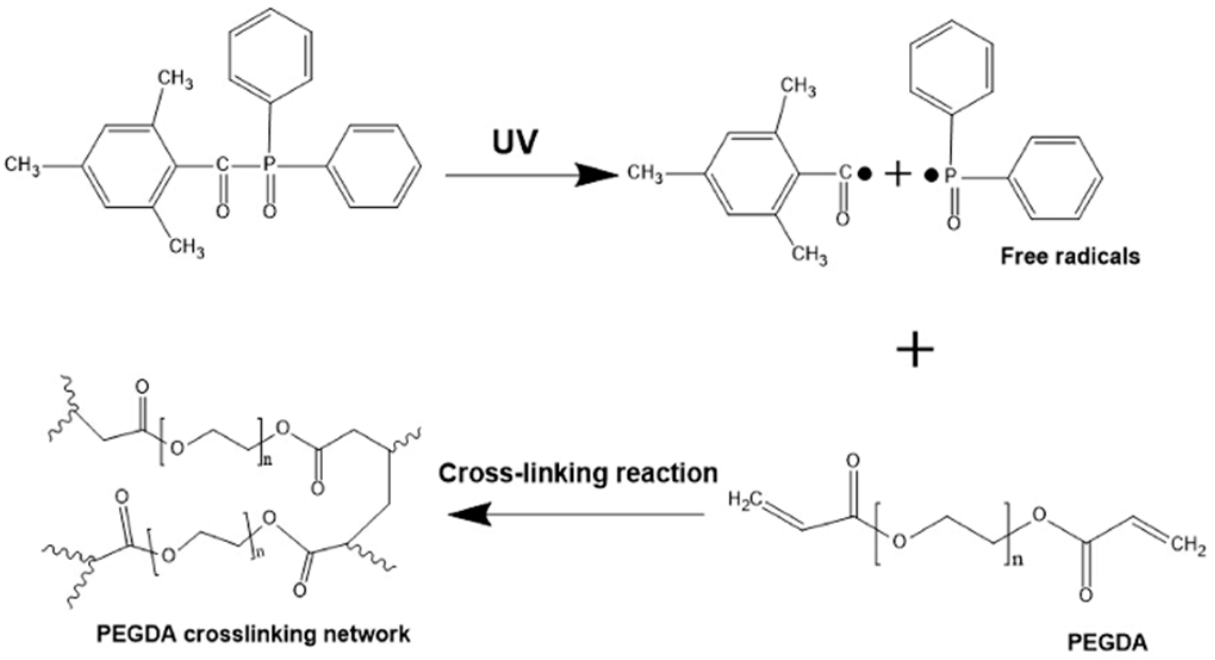

Figure 6: Impact of UV Crosslinking on PEGDA Polymer Reaction.

The illustration showcases the transformative effects of UV light exposure on the PEGDA polymer reaction, both before and after the process. In the presence of UV light, diphenyl (2,4,6-trimethylbenzoyl)-phosphine oxide (TPO) emerges as a pivotal component, absorbing light and generating free radicals. These radicals actively engage with monomer molecules, initiating the cleavage of carbon-carbon bonds (covalent bonds). The subsequent interplay of reaction monomers leads to the formation of expansive molecules that progressively elongate until two chains merge, making the completion and termination of the reaction. Reproduced from Yang, W. and Liu, L., 2015 with permission from *Micromachines (Basel)*.

1.4.2 Benefits of Incorporating Plant-Cellulose into Bioprinting

Incorporating decellularized plant cellulose into the 3D ink has some benefits. It offers structural support for cells to grow and proliferate, acting as a template for the formation of new tissue the decellularized plant-cellulose has a microporous structure that enhances the attachment of mammalian cells. This porous structure can absorb a large amount of biological fluids[87], making it an ideal environment for simulating the properties of living tissues[88]. Cellulose also provides the necessary mechanical properties to maintain the integrity of the scaffold, resulting in a more stable and durable structure. This innovative combination of bioprinting technology and plant-derived materials holds promise for advancing both regenerative medicine and sustainable biomanufacturing practices[89,90].

1.5 BY-2 Tobacco Cell Line

The Tobacco Bright Yellow-2 (BY-2) cell line (**Figure 6**) is a well-established tool in plant tissue culture and biotechnology research[55], making it an ideal candidate for this application. Initially developed for the mass production of raw materials for cigarettes, these cells have evolved into what is often referred to as the "HeLa cell" of plant biology[91]. Derived from *N.tabacum L.cv.* plants, they boast a remarkably short generation time, multiplying approximately 100-fold in a week. This rapid growth makes them ideally suited for large scale production[92]. BY-2 tobacco cells are formed through the initiation of callus culture, isolation of individual cells, and subsequent suspension culture in a liquid medium[93]. Their connection to each other is facilitated by plasmodesmata, even in the absence of physical attachment as seen in solid tissues[94]. Furthermore, BY-2 cells are easily transformable and maintainable in culture, demonstrating a high tolerance transformation with fluorescent proteins like the green fluorescent protein and its derivatives. This versatility makes them invaluable for targeting sequences, enabling researchers to direct studies towards specific subcellular locations for in vivo analysis[95].

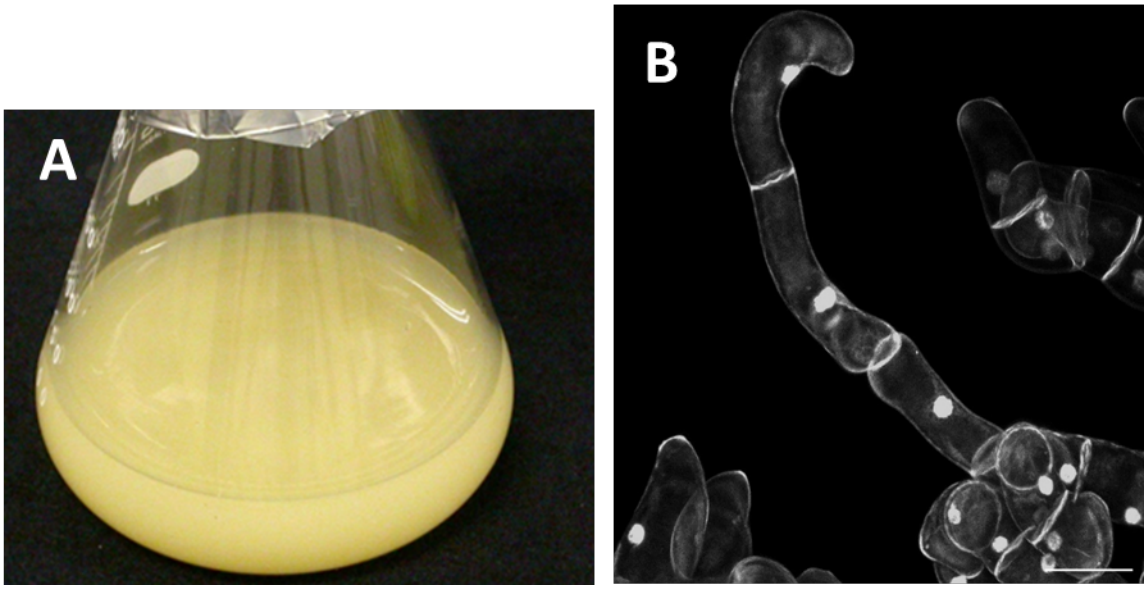

Figure 7: Cellular Architecture of Tobacco BY-2.

This illustration provides a visual representation of the intricate cellular structure of Tobacco BY-2. Scale bar B: 50 μm.

1.5.1 Decellularized BY-2

The porous structure and soft consistency of decellularized BY-2 cells offer a remarkable opportunity to fabricate scaffolds that closely resemble the properties of living tissues[96]. In a recent research study, both tobacco BY-2 cells and rice cells were decellularized using deoxyribonuclease I. The decellularization process not only retained approximately 36% of total protein but also demonstrated the ability to retain 33% of enhanced green fluorescent protein, underscoring the effectiveness of the technique for potential biomedical applications[55].

Furthermore, the unique porous structure and soft consistency of BY-2 cells make them particularly valuable in the field of tissue engineering[97]. The decellularization of BY-2 cells has emerged as a transformative technique, enabling the creation of scaffolds that closely mimic the properties of living tissues. This process involves strategically opening the cell membrane in a porous manner, facilitating the infiltration of detergents into the cells. This allows for the extraction of cellular content while preserving the structural integrity of the BY-2 cell, resulting in a decellularized plant structure that can serve as an optimal scaffold for various applications.

1.6 Conclusion

We hypothesize that adding BY-2 cells to PEGDA increases cellular infiltration and biocompatibility of the polymer which results in a better customizable scaffold for various tissue engineering purposes.

The advancements in bioprinting techniques and scaffold customization hold an important spot in the field of tissue engineering by integrating decellularized BY-2 cells into synthetic polymers provides a biomimetic scaffold abundant in crucial components facilitating mammalian cell adhesion. It's widely acknowledged that this matrix not only allows for cell attachment but also provides biochemical and biophysical cues to emerging cells and tissues[98]. As we continue to develop techniques to create scaffolds, we move closer to realizing the full potential of tissue engineering in revolutionizing healthcare and regenerative medicine.

Chapter 2

Decellularization Techniques for Plant-Derived Cellulose Scaffolds and 3D-Printed Methods to Optimize Custom Made Scaffolds.

2.1 Introduction

Tissue engineering is a field of biomedical engineering that involves creating functional three-dimensional (3D) tissues using cells, biomaterials, and biochemical cues. The aim is to create functional biological substitute biomaterials to repair or replace damaged tissues and organs in the human body[99]. The incorporation of the 3D concept into the structure is vital as it closely emulates the intricate architecture and functionality of native tissue[100,101]. These structures, often referred to as scaffolds, provide a supportive framework for cells to attach, proliferate, and differentiate; ultimately forming new tissue[102,103].

Plant-based scaffolds have several benefits similar to animal-derived scaffolds, except they are derived from a more "renewable" source[90,104,105]. Plant materials are biocompatible and sometimes have bioactive properties that aid in healing[106]. The native structure of certain plant tissues can be leveraged to guide cell alignment, making them a promising biomaterial for tissue engineering applications. To achieve the desired functionality, plant-based scaffolds can incorporate other cell types, soluble or matrix-bound growth factors, or adhesion molecules to ensure the efficacy of the implant[107]. However, there are still disadvantages to using plant-based scaffolds. One major challenge is the variability associated with plant production *in vitro*, which can result from differences in growing conditions, harvest times, or aseptic condition processing methods[108]. Additionally, the mechanical properties of plant-based scaffolds can be a limitation, since these materials often exhibit lower strength, flexibility, and durability compared to synthetic alternatives. This limits their use in certain applications that require high mechanical performance[109].

One innovative approach to creating plant-based scaffolds is decellularizing plant tissues, which involves removing all the cells contained in the plant tissue, leaving behind a sturdy cellulosic scaffold[43,56,110–115].By decellularizing plant tissues, one can preserve the structural integrity of the original tissue while creating an environment conducive to host cell infiltration without the risk of rejection due to cellular remnants[116]. Failure to fully decellularize plant tissues presents several challenges. Immunogenicity may emerge, where the presence of cellular components can trigger an immune response when implanted into the body[117]. Additionally, inflammation may occur as cellular debris can interfere with host cell attachment, proliferation, and differentiation[118–120]. Several labs have demonstrated that common decellularization approaches can produce plant-derived cellulose scaffolds that support 3D cell culture[121–123]. Various different techniques have been developed to ensure the complete elimination of cellular remnants [43,54,56–58,112,124]. While a lot of researchers mostly utilize detergent-based decellularization, other researchers have explored alternative approaches. For instance, some have employed Deoxyribonuclease (DNases) treatment to target genetic material removal[115]. Bleach has also proven effective in clearing plant constituents from leaves and stems[114]. Additionally, an alternative approach involves immersing leaves in water followed by treatment with a 5% NaOH solution heated to 90°C[113]. Moreover, the combination of high-pressure freezing has demonstrated efficacy in decellularizing plant cells, presenting another promising method in this field[125].

However, there are limitations to simply decellularizing a plant and using it in its natural structural state. Consider a decellularized apple[43,56], for example, which primarily consists of components like pectin (12%), lignin (2%), hemicellulose (5%), and cellulose (5%)[126]. Microscopically, the cellulose of the apple has ring shapes[56]. While it can be reshaped and sculpted, its internal structure remains immutable. Neither its stiffness nor flexibility can be adjusted, thus restricting the range of potential applications[56,126].

3D printing, also known as additive manufacturing, is a process of creating 3D objects layer by layer using a digital model[127,128]. The advent of this technology has allowed researchers to incorporate the benefits of cellulose's structure with the design capabilities offered by synthetic polymers. These composites are often referred to as printing ink, which is used to create an array of shapes and structures to meet the requirements of specific tissue engineering needs. These composite scaffolds can be manipulated to not only emulate the desired shape but also the stiffness and flexibility to make a perfect tissue match[74,129]. In 3D printing, the process entails layering multiple successive layers of the composite material, allowing for precise control and customization of the final product.

As mentioned in Chapter 1, this project focused on incorporating decellularized BY-2 plant cells derived from the species *Nicotaina tabacum* into the scaffold made with PEGDA, crosslinked using UV light[83,130]. The objective is to 3D print a scaffold rich in BY-2 decellularized plant cells, maximizing porosity to facilitate optimal penetration of mammalian cells and tissue regeneration. Additionally, the aim is to create a custom-made scaffold with the desired shape, stiffness, and flexibility to achieve a perfect tissue match.

Therefore, my project will focus on bringing together plant decellularization techniques with 3D bioprinting to create decellularized plant scaffolds with controllable architectures. More specifically, optimizing techniques for the decellularization of the BY-2 Tobacco cells, to harness their cellulose structure, involves refining methods to efficiently remove cellular components while preserving the integrity of the cellulose matrix. This will involve careful consideration of factors such as temperature, chemical composition, enzymes, and duration of treatment to achieve optimal results to suit the specific requirements of BY-2 Tobacco cell content extraction. To gauge the efficacy of these methodologies, we employ confocal microscopy to visualize the cell nuclei. The presence of residual nuclei within decellularized plant scaffolds indicates that the cytoplasmic content was not completely removed. This could be detrimental, potentially triggering immune

responses when deployed *in vivo* because the incompleteness may result in the retention of cellular remnants or bioactive molecules. The immune system will recognize these remnants as foreign bodies or antigens which can lead to inflammatory responses or even the rejection of the implant[110]. The resulting product would then be blended with PEGDA to create a biocompatible ink, which will be incorporated in the Lumen-X 3D bio-printer. Scaffolds will then be printed, and their biological resistance and compatibility will be assessed. This seamless blend of methods and materials marks a promising step forward in tissue engineering, utilizing natural resources. In addition, after optimizing a good scaffold, a comprehensive understanding of scaffold mechanical properties is essential for ensuring successful tissue regeneration[131].

Young's Modulus is a fundamental concept extensively utilized in tissue engineering, providing valuable insights into the mechanical properties of materials, particularly their stiffness and elasticity, which are critical for the suitability of implants for specific anatomical locations. Variations in Young's Modulus allow the customization of implants to cater to diverse physiological requirements[132]. The elasticity of the scaffold is pivotal, delineating its ability to withstand external forces while reverting to its original state post-deformation[133]. In a previous study, scaffolds for heart valve replacement were developed to mimic the mechanical behaviour of human heart valves by tailoring their mechanical properties based on Young's Modulus. Utilizing photolithographic patterning, they introduced anisotropic mechanical properties into PEG hydrogels. These engineered hydrogels, containing specific peptides, influenced the behaviour of encapsulated valvular interstitial cells, impacting their elongation, extracellular matrix deposition, and hydrogel degradation[134].

Young's Modulus varies significantly among different tissues, reflecting their unique mechanical properties and functional roles within the body. For example, bone tissue exhibits a high Young's Modulus, typically around 7,600 to 20,000 kPa, due to its need to support and protect the body[135]. In contrast, softer tissues like skin have much lower values, typically between 5 and 1

000 kPa[136]. Muscle tissue ranges from 8 to 17 kPa, while the brain is the softest, with Young's modulus between 0.1 to 1 kPa[137]. Understanding these variations is crucial for tissue engineering because it enables the design of implants and scaffolds that mimic the mechanical properties of native tissues, enhancing their functionality and longevity while minimizing the risk of rejection or failure[138–141].

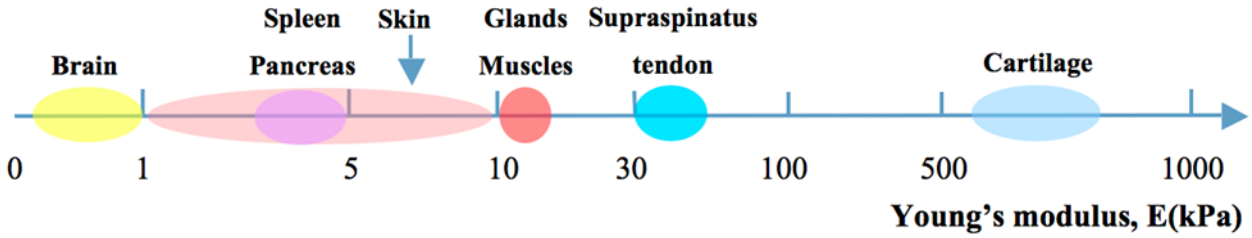

Figure 8: Young's modulus of natural soft tissues and organs in Kilopascal (kPa).

Reproduced from Liu, J and Schilling, A., 2015 with permission from *International Journal of Molecular Sciences*.

Calculating Young's Modulus and understanding the underlying mechanics that define it are important for accurate material characterization[142]. Young's Modulus is derived from a mathematical formula where stress is measured overstrain. Stress is the force applied per unit area of the material, and strain is the deformation or displacement of the material relative to its original length. Young's Modulus, therefore, quantifies the stiffness of a material by indicating how much it will deform under a given load. A higher Young's Modulus means the material is stiffer and less prone to deformation, while a lower value indicates a more flexible material[143]. The equation is as follows:

$$E = \frac{\sigma}{\epsilon}$$

Where E is the Young's Modulus, σ is the uniaxial stress, and ϵ is the strain[144].

Young's Modulus assumes a pivotal role in the realm of 3D bioprinting, influencing scaffold properties through precise control over printing parameters[145–147]. Young's Modulus results indicate the mechanical characteristics of the scaffold, affecting its elasticity and softness.

The printer settings including crosslinking methods, enable tailored adjustments to scaffold properties[148]. In a recent study focused on developing complex tissue construct resembling osteochondral tissue, researchers utilized a 3D printer to create a hydrogel bioink. This bioink, consisting of GelMA (gelatin methacrylate), dopamine-functionalized GelMA, and acrylate β-cyclodextrin, not only enhances mechanical strength but also enables sustained drug release. This remarkable achievement is made possible by the ability to modify 3D printing parameters that were assessed using Young's Modulus. This showcases the profound impact of precise control over scaffold properties in advancing tissue engineering[149.]

In our study, using the PEGDA Start PhotoInk from Cellink in the 3D bioprinter Lumen-X, we explored the impact of UV crosslinking time on scaffold properties. Extending the exposure time yields a stiffer, less elastic scaffold, while shorter exposure durations result in softer, more elastic scaffolds. The stiffness can be altered by increasing the duration of exposure between layers. A minimum length of 0.5 seconds is required to achieve complete crosslinking. [150,151].

The adoption of additive manufacturing technology allows for homogeneous crosslinking by sequentially printing and crosslinking hydrogel bioinks layer-by-layer. This versatility is changing Young's Modulus, which empowers researchers to fine-tune scaffold properties to meet the demands of specific tissue engineering applications, facilitating advancements in regenerative medicine and implant design. Through the 3D printer, researchers can modulate the parameters of scaffolds and alter them according to their desires.

2.2 Material and Methods

2.2.1 Establishment of Tobacco BY-2 Culture

BY-2 cells are commonly used in laboratory studies and have a high propagation rate of 80 to 100-fold per week. The cells will be passaged every week to maintain an appropriate cell concentration and to not saturate the media. The cells will be cultured on a rotary shaker at 130 rpm, at 27 degrees Celsius, in the dark[91]. Growing the cells in the dark prevents photosynthesis, allowing them to focus on cellular growth and division, which is crucial for maintaining their high propagation rate[152].

2.2.2 Optimization of BY-2 Decellularization Method

The goal of this process is to create a concentrated material with a maximum BY-2 cellulose yield. In this study, I tested three different methods to achieve this:

The First Method involves a customized maceration technique originating from an established protocol (Yeung, 1998). This method includes a mixture of glacial acetic acid, 30% hydrogen peroxide, and water to permeabilize the cell wall and destroy the protoplast and cell membrane. The maceration mixture was added to a BY-2 cell pellet and incubated in a 50°C water bath, overnight. Afterward, the cells were washed with distilled water and incubated in double distilled water (ddH2O) overnight, on a shaker set at 130 rpm, at room temperature. After every washing step, the supernatant was removed through centrifugation at 4000 rpm for 5 minutes, leaving behind a cell pellet. This step removes all cytoplasmic and protoplast content, resulting in a visibly white pellet. The pellet was then added to a 0.1% SDS (Sodium Dodecyl Sulfate) solution from Fisher (BP166-500) and agitated on a shaker for 1-2 days at room temperature. The SDS was refreshed daily by removing the old solution via centrifugation at 4000 rpm for 5 minutes and adding fresh SDS solution. After the second day, the cells were added to Calcium Chloride ($CaCl_2$) 100 mM and incubated on a shaker at 130rpm for 2 days to wash off the SDS. The $CaCl_2$ solution was also removed by centrifugation at 4000 rpm for 5

minutes. The sample was then washed in 1X phosphate-buffered saline (PBS) (MP Biomedicals) for 1 day and ddH2O for 2 days.

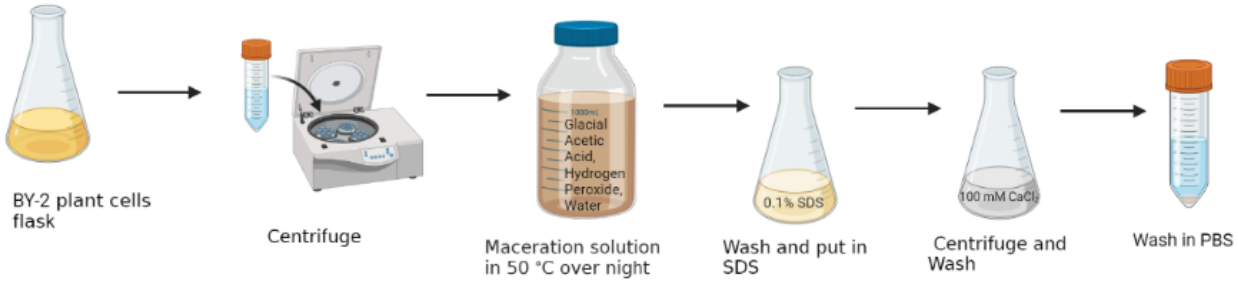

Figure 9: Decellularization – Method 1. Created with Biorender.com

The Second Method builds upon the first method, introducing an approach: Instead of SDS, Deoxyribonuclease (DNases) at a concentration of 0.25 g/L were used. The DNases were added directly to the cell pellet and incubated at room temperature overnight. The following day, the DNase-tested solution was centrifuged for 5 minutes at 4000 rpm to remove the DNases. DNases break down the deoxyribonucleic acid (DNA) fragments in the plant cells to help decellularize[153].

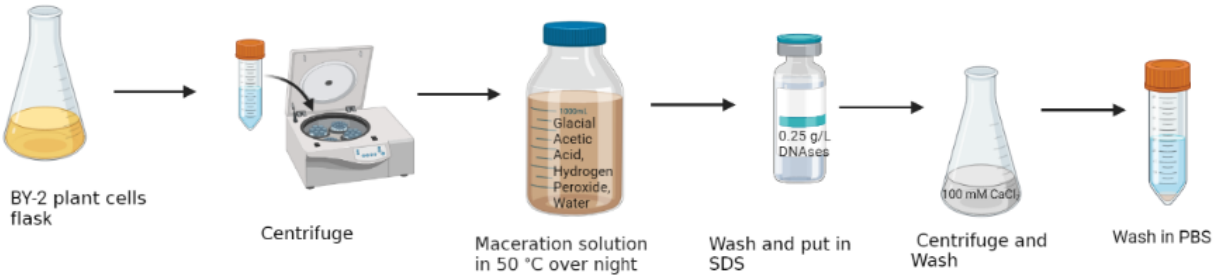

Figure 10: Decellularization – Method 2. Created with Biorender.com

For the Third Method, the cell pellet was frozen and thawed to lyse the cells, achieved by freezing and rewarming[154]. Adding this step helps to avoid the use of chemical agents, thereby minimizing potential residual toxicity. The frozen cells were thawed at room temperature for 12 hours, then centrifuged at 4000 rpm for 5 minutes to remove any leftover water from the ice or media. SDS (0.25 %) was then added to the pellet. The cells were then incubated for four days with

daily solution change. After centrifugation, the cells were incubated in $CaCl_2$ 100 mM overnight and washed twice with water.

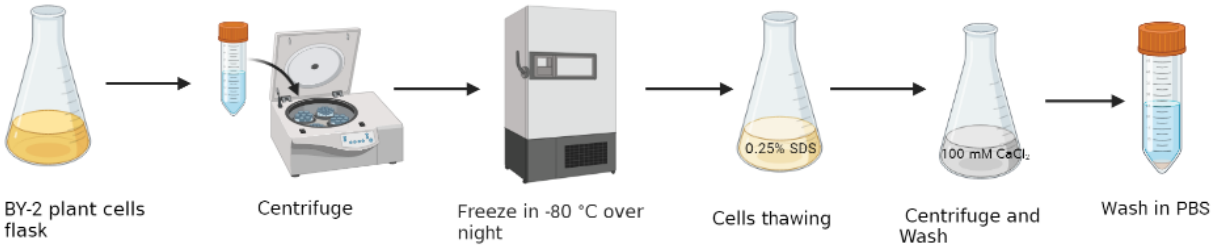

Figure 11: Decellularization – Method 3. Created with Biorender.com

2.2.3 Immunofluorescence Staining

After testing the three decellularized methods, all cell pellets were stained with Hoechst 33342 (Thermo Fisher H3570), to investigate any remaining protoplast and cell nuclei. To facilitate imaging, a 10-minute incubation of Hoechst dye (0.05 mg/ml) was carried out on the decellularized cell pellet, followed by a single wash with PBS.

2.2.4 Optical Microscopy

Confocal imaging was performed using an A1R high-speed laser scanning confocal system on a TiE inverted optical microscope platform (Nikon, Canada) with appropriate laser lines and filter sets. Transmitted light images were acquired on an inverted TiE microscope (Nikon, Canada) with phase contrast optics. Before imaging, the plant cell was positioned between a coverslip and slide, and samples were imaged with a 40X lens. The images presented are Maximum Intensity Projections. All images were analyzed using ImageJ software.

2.2.5 Fabrication of the Plant Cell Hydrogel Base

The plant cell hydrogel base was prepared by first mixing PEGDA with BY-2 cells in a mass ratio of 2:1. This mixture was thoroughly vortexed to ensure uniform distribution. To eliminate any visible air bubbles, the solution was left to stand for an hour at 4°C until no bubbles were visible. Finally, to maintain stability and prevent premature polymerization, the hydrogel base was stored at 4°C.

2.2.6 Construction of the Hydrogel Plant Base Scaffold

To construct the hydrogel plant base scaffold, a crosslinker is needed to establish the cellulose networks[155]. We used PEGDA Start PhotoInk (Cellink), which contains PEGDA polymers and the photoinitor lithium phenyl-2,4,6-trimethylbenzoylphosphinate (LAP). Scaffold construction was performed using the Lumen-X Bio-printer from Cellink. Printer settings were adjusted to include a 10-second UV light exposure at a wavelength of 405 nm, with double exposure time for the first layer to ensure a robust base formation. The software Thinkcad was employed to design and customize scaffold shapes as per experimental specifications.

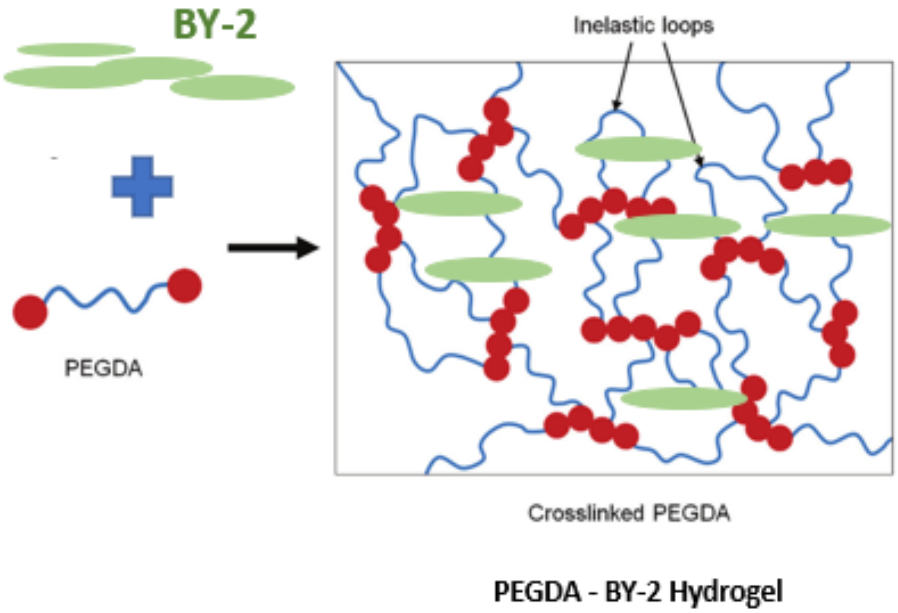

Figure 12: The mixture of BY-2 and PEGDA before and after UV crosslinking.

2.2.7 Mechanical Properties

The Young's Modulus of the 2 different formulations (the PEGDA and BY-2 scaffold and the PEGDA alone) were measured after bioprinting and cross-linking samples with UV light using the UniVert testing machine (CellScale) at a crosshead speed of 3 mm/min. For all samples, Young's modulus was devised from the linear region of the strain curve, as shown in **Figure 13**, and the compression strengths were recorded as the amount of stress at 10 % total strain. We do not go beyond the linear elastic region to avoid entering the plastic deformation region, where the material would undergo irreversible changes. The values reported here are the average of 10 specimens for each formulation. Samples preparation is the same as those used in the *in vitro* assay: scaffolds were sterilized with 70% ethanol overnight followed by 7 thorough saline washing.

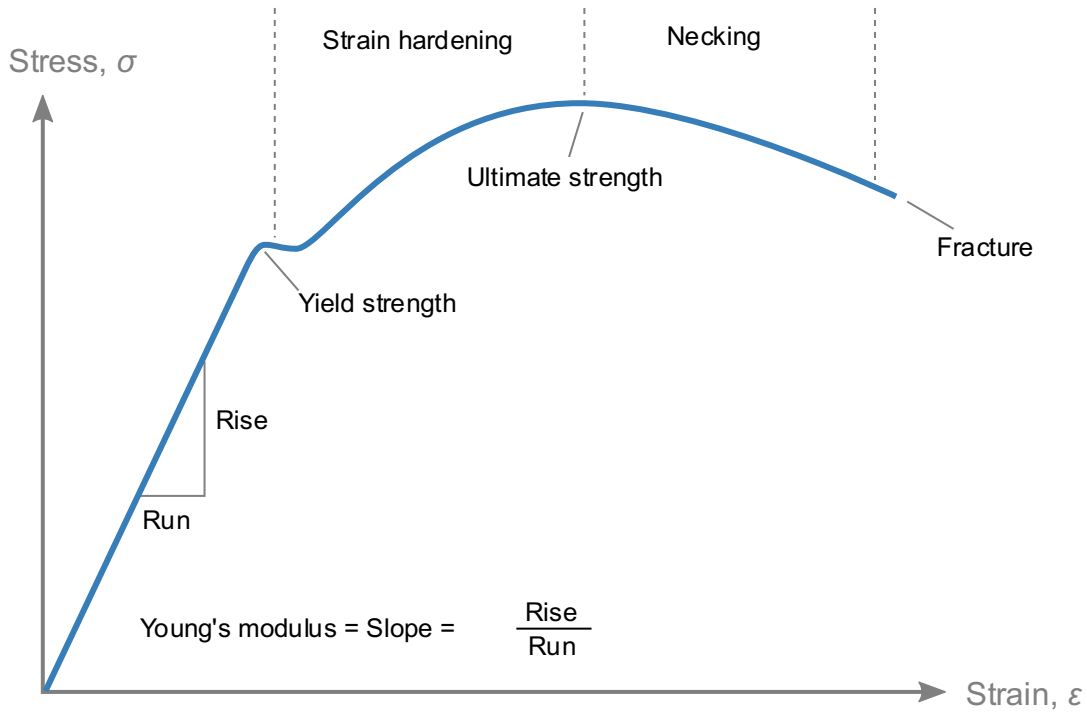

Figure 13: **Stress-Strain Curve for Ductile Material.**

The Young's modulus is derived from the linear elastic region of the curve, where the material exhibits proportional stress and strain. Beyond this region, the material enters the plastic

deformation region, where permanent deformation occurs, and thus it is not considered for calculating Young's modulus.

2.2.8 Statistical Analysis

Student's *t* tests were utilized for comparing two samples in all analyses. Statistical significance was obtained by using Graphpad Prism Software, with significance donated by an asterisk (*) indicating a P-value < 0.05.

2.3 Results and Discussion

2.3.1 Optimization of the Decellularized Method

We assessed the different decellularization methods, as shown in **Figure 14**. The goal of this experiment was to find the most efficient way to remove the cellular content. We specifically tested for nuclear remnants by staining with Hoechst. Hoechst 33342 is a blue, fluorescent dye that binds to the adenine-thymine region of Deoxyribonucleic acid (DNA)[156]. Hoechst is used as a control to assess the effectiveness of the decellularization process. There should be no remaining DNA in the cells following decellularization.

The presence of Hoechst stain in **Figure 14B** and **14C** (first and second methods respectively) indicated that the nuclear content remains intact. However, in **Figure 14D**, there were no visible nuclei, indicating successful removal of cellular nuclei using the third protocol. This result aligns with our tissue engineering goals, as the absence of cellular nuclei in the decellularized material is desired to prevent immune response and facilitate tissue regeneration. The presence of intact cell nuclei indicates that the decellularization process was not effective in disrupting the cell wall. The third method was not only successful in removing all the nuclear content but also did not disturb the structural integrity of the cell wall, as evident when comparing **Figure 14A** (control, live BY-2) and **7D** (completely decellularized BY-2).

Therefore, method 3 is the most effective decellularization technique. This method involved replacing either the maceration (from method 1) or DNase steps (from method 2) with freezing at -80°C overnight without the use of a cryoprotectant. The freezing of the cell cytoplasm induces the formation of ice crystals, disrupting the wall (microtears). The porous cell wall provides an entry point for SDS, a detergent that further permeabilizes the cell wall and allows for efficient extraction of cellular contents. Methods 1 and 2 both have the SDS step, which was superseded by a maceration step, and for method two an addition DNases step. These methods have proven insufficient in eliminating all cellular contents, as evidenced in **Figures 14B** and **14C**, where residual plant nuclei BY-2-shaped cells were observable**.**

Preserving cell wall integrity while eliminating cellular content is paramount for fabricating customizable, biocompatible scaffolds essential for tissue engineering applications. The structure in **Figure 14D** remains intact and shows no nuclei, validating the effectiveness of this chosen methodology.

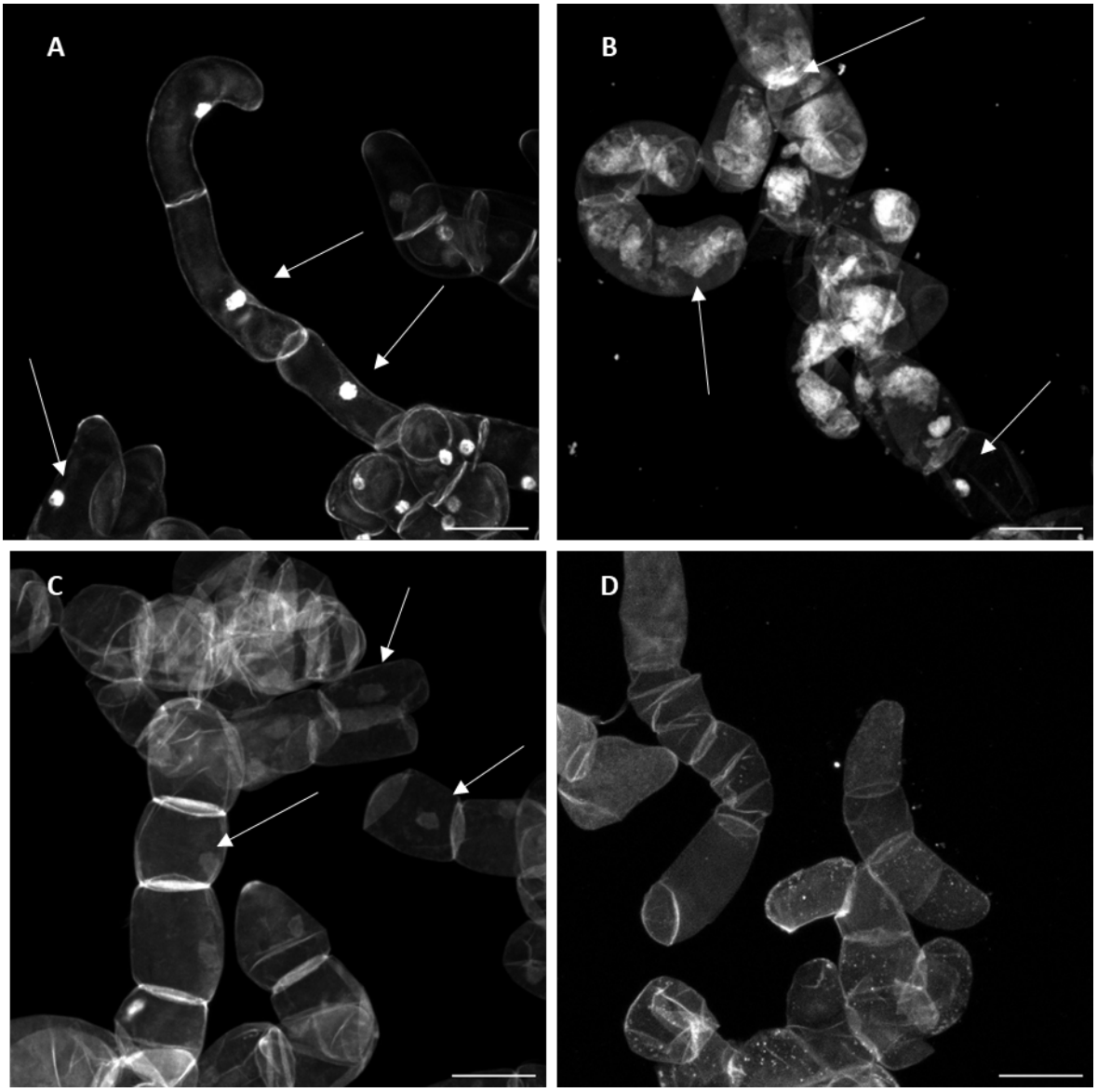

Figure 14: Comparison of different decellularization approaches.

Image A shows Hoechst staining to investigate any remaining protoplast and cell nuclei. The first method consists of maceration in a solution of SDS 0.1%, shown in **Image B**. The second method of decellularization, uses DNases and SDS 0.1% as seen in **Image C**. The third method of decellularization, combines the freezing of the cells and the use of SDS 0.1% shown in **Image D**. Arrows indicate residual nuclei in the plant cells. In **Image D**, all nuclei are gone, indicating complete decellularization. Image analysis was performed using ImageJ software. Scale bar = 50 um, captured using a 40X lens.

2.3.2 Optimization of the Scaffold Ink

The primary objective is to maximize the incorporation of decellularized BY-2 cells within the scaffold, aiming to enhance the formation of micropores throughout the structure. This strategic approach is pivotal for promoting cellular infiltration and facilitating the development of a biomimetic microenvironment [157,158]. However, it is imperative to ensure that the scaffold remains printable throughout the fabrication process. Achieving this delicate balance necessitates meticulous attention to the formulation of the bioink, optimizing the concentration and distribution of BY-2 cells to promote uniform deposition and structural integrity.

Figure 15A showcases a successful print, indicating the potential for further enhancement by increasing the incorporation of decellularized BY-2 cells. After numerous iterations, a 2:1 mass ratio of PEGDA to BY-2 is the optimal formula, striking the desired balance between printability and cellular incorporation, as demonstrated in **Figure 15B**. However, as depicted in **Figure 15C**, excessive BY-2 content resulted in a poorly printed scaffold. Since our objective is to maximize BY-2 cell density within the scaffold while maintaining printing quality, **Figure 15B** is the ideal scaffold ratio for this project. **Figures 15D** and **15E** show what the scaffold should look like in the software Tinkercad.

Moreover, the crosslinking agent, PEGDA and LAP photoinitiator, play a critical role in facilitating the crosslinking process initiated by UV light exposure. The judicious selection of the amount of PEGDA in the PEGDA: BY-2 mass ratio is essential to ensure sufficient crosslinking density, thereby imparting stability and strength to the scaffold architecture. This ensures the robust layer-by-layer assembly of the scaffold, preventing structural deformation and maintaining dimensional accuracy throughout the printing process. By meticulously controlling the crosslinking parameters, including UV exposure time and intensity, we can further enhance the reliability and reproducibility of scaffold fabrication, ultimately yielding high-quality tissue constructs tailored to meet precise therapeutic requirements.

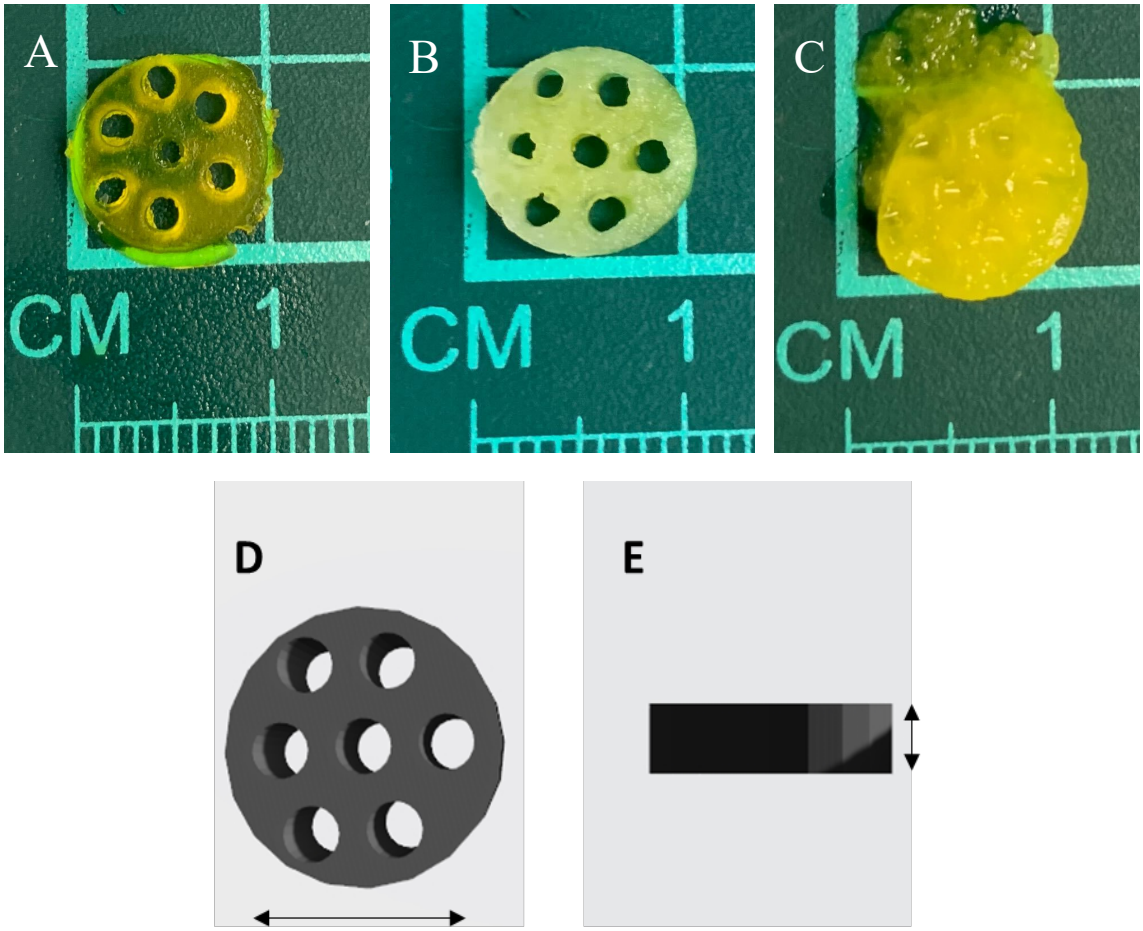

Figure 15: Optimization of BY-2 and PEGDA Scaffold Mass Ratios.
This figure illustrates the impact of varying ratios of PEGDA to decellularized BY-2 on scaffold properties. The yellow coloration is due to the photoinitiator LAP in the PEGDA ink. The goal is to achieve a scaffold that is constant and has open pores, maintains a good shape, and maximizes the incorporation of BY-2 decellularized plant cells. Scaffold **A** represents a ratio of 3:1 PEGDA to BY-2, Scaffold **B** showcases a ratio of 2:1, and Scaffold **C** demonstrates a ratio of 1:1. Image **D** and Image **E** show the 3D model designed using the software Tinkercad, with Image **D** scaled to 1 cm in length and Image **E** scaled to 3mm in thickness.

Now that we have established an optimal formulation for one shape, the next challenge was to explore various scaffold shapes. Customizable scaffolds hold immense promise for advancing tissue engineering and regenerative medicine[159]. We then set to evaluate our capability to fabricate hydrogel scaffolds of different shapes and pore sizes as shown in **Figure 16**, a task facilitated by 3D bioprinting - a pivotal tool in this process[160]. Unlike traditional scaffold fabrication methods, such as casting or molding, bioprinting enables the layer-by-layer deposition of bioinks containing PEGDA and Decellularized BY-2 allowing for precise control over scaffold architecture, uniform distribution of the bioink, and the creation of heterogenous scaffold[161,162].

We first designed the haystack shape**,** shown in **Figure 16A**, featuring larger pore sizes within the scaffold, providing ample space for cell infiltration. This feature is particularly advantageous for applications requiring robust cell integration and tissue formation, such as in the regeneration of volumetric tissues like skin or adipose tissue [163,164].

We also designed cylindrical shaped scaffolds shown in **Figure 16B,** with larger pores. Such a design could be particularly suitable for applications where enhanced fluid exchange and cell infiltration are desired. A more porous structure is good for the diffusion of waste products out of the scaffold as well[165].

On the other hand, **Figure 16C** presents a scaffold with smaller, more densely packed pores. This finer pore structure is conducive to providing mechanical support and guidance for cell growth and neurite extension, making it well-suited for applications involving neural tissue regeneration, such as spinal cord repair[112]. The small pores can serve as channels for guiding the growth of neuronal processes and facilitating the formation of neural networks within the scaffolds. Additionally, the scaffold's cylindrical shape mimics the anatomical structure of the spinal cord, further enhancing its compatibility for implantation and integration with the host tissue.

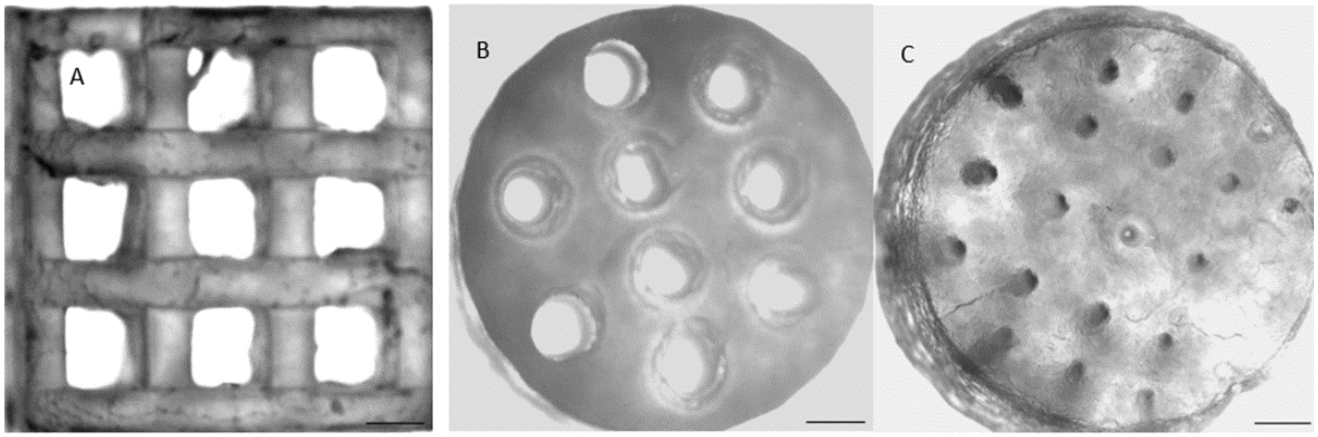

Figure 16: Hydrogel Scaffolds Design.

Hydrogel scaffolds were designed with various pore sizes, using the Lumen-X bioprinter and viewed through stereoscope microscopy. Scaffold **A** showcases a haystack shaped 10x10 mm with 9 pores of 2x2 mm each. Scaffold **B** showcases a cylinder-shaped scaffold with a circumference of 3.17 cm with 9 porous of 3.7 mm of circumference. Scaffold **C** showcases a cylinder-shaped scaffold with a circumference of 3.17 cm with 21 pores of 1.2 mm of circumference. All scaffolds are 3mm in height. Scale bar = 1 mm. Designs were made with the software Tinkercad.

2.3.3 Young's Modulus

Understanding Young's modulus in tissue engineering is important for comprehending tissue behaviour, particularly given the diverse compositions of various scaffolds, which can significantly affect their level of resistance and elasticity[166,167]. As mentioned in the introduction, the bioprinting method allows for the customization of Young's modulus. **Figure 17A** demonstrates the impact of varying UV light exposure time on the formulation of PEDGA + BY-2 scaffolds, as photo-crosslinking can be adjusted to modulate Young's modulus[168,169]. The graph depicts exposure times of 4s, 10s, and 12s, chosen based on preliminary experiments that indicated these durations would provide a broad range of mechanical properties. Notably, Young's modulus distinct changes; at 4s, it registers a lower average of 34.45 ± 9.82 kPa; at 10s, an average of 57.67 ± 9.72 kPa is observed; and the 12s, the average rise to 65.88 ±8.04 kPa. These findings underscore the tunability of the bioprinting process, enabling precise control over scaffold properties to meet specific application requirements.

As mentioned in **Figure 8** of the introduction, Young's modulus varies across different tissues. **Figure 17A** extends this principle by showcasing the variability achievable within tissues. By correlating with **Figure 8**, we discern that lower UV exposure time may mimic tendon properties 30 to 50 kPa, with higher exposure times could emulate cartilage or even bone characteristics. Altering ultraviolet light exposure times allows the designer to change the density and softness of the scaffold without or in addition to the 3D printing process. Additionally, **Figure 17A**, shows that the materials become harder with increased UV light exposure. Significant differences are observed between expose times of 4s and 10s, as well as between 4s and 12s, with p-values smaller than 0.0001. These findings, obtained through Student *t*-test analysis, highlight the potential to create various tissue types by adjusting UV light exposure durations.

In **Figure 17B**, the comparison between PEGDA alone and PEGDA combined with BY-2 decellularized plant cells reveals an important insight. PEGDA alone exhibits considerable variation, with an average Young's modulus of 46.85 ± 29.95 kPa. In comparison, PEGDA

combined with BY-2 cells shows more consistent Young's modulus values, with an average of 57.67 ±9.72kPa. The PEGDA combined with the BY-2 cells scaffold is more resilient and consistent, while PEGDA alone is more prone to brittleness and exhibits greater variability. The range of values for the PEGDA alone scaffold is much higher than for the PEGDA+BY-2 scaffold. Given our objective of creating a hydrogel, we aim to maximize elasticity to ensure the scaffold can withstand pressure within the body without fracturing[170,171].

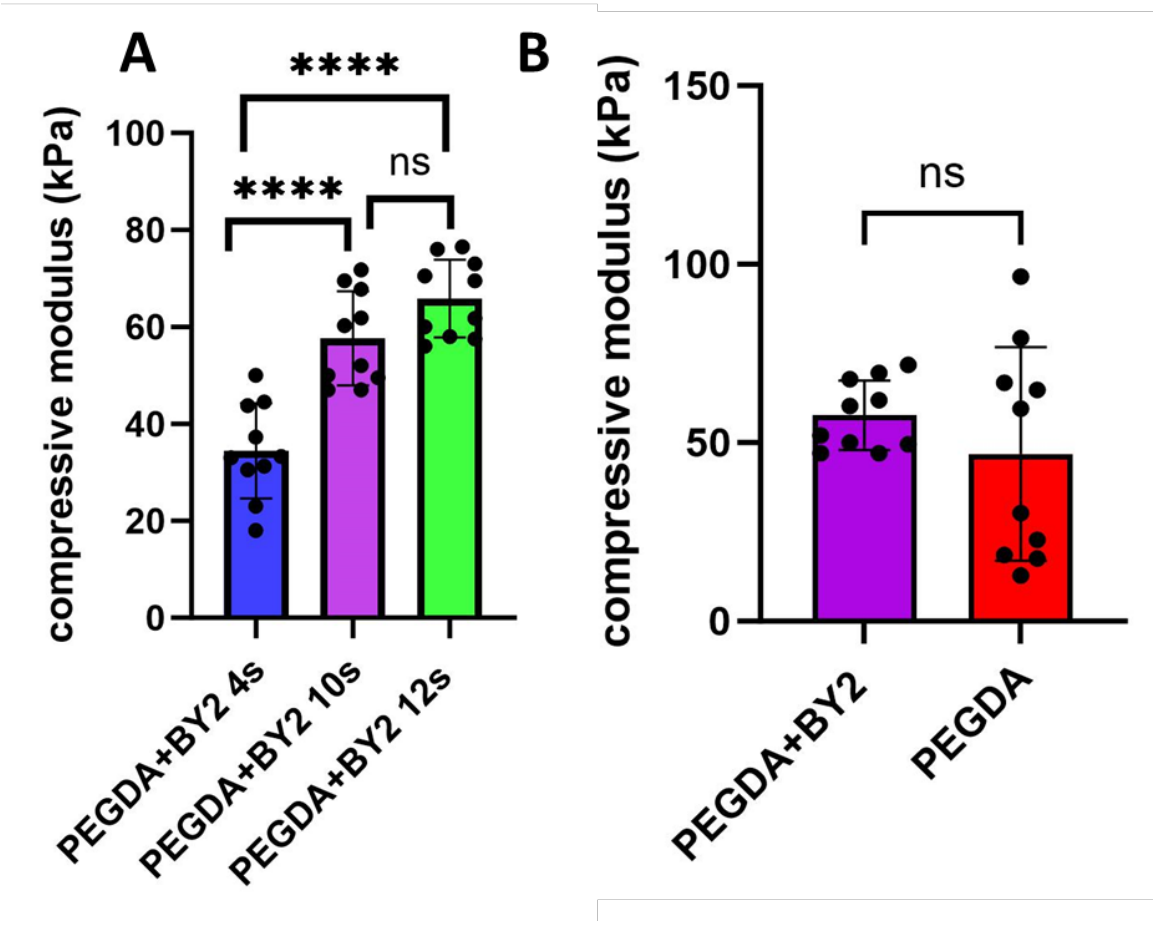

Figure 17: Comparison of Young's Modulus in Various Scaffolds.

Graph A illustrates the impact of different UV light exposure durations (4, 10 and 12 seconds) from the Lumen-X bioprinter on Young's modulus of the scaffolds. Graph B showcases the comparison between scaffolds composed of PEGDA only and PEGDA combined with BY-2 decellularized cells under a 10-second UV light exposure. These assessments were conducted using the UniVert testing machine (CellScale) with the stress measured at 10 % total strain and a speed of 3 $mm.min^{-1}$. Each was tested with 10 scaffolds.

In this figure, "ns" stands for "not significant," indicating that the differences observed were not statistically significant. Conversely, "****" denotes a highly significant difference with a p-value less than 0.0001.

2.4 Conclusion

In conclusion, our study highlights the critical importance of optimizing decellularization methods and scaffold ink formulations in tissue engineering endeavours. Through meticulous experiments, we established a good decellularization technique (method 3), which effectively removed cellular content while preserving structural integrity. This technique, which involves freezing at –80 degrees without cryoprotectants, proved to be the most efficient method of decellularization for our intended application.

Our exploration into scaffold ink optimization underscored the delicate balance between printability and cellulose incorporation. By fine-tuning the mass ratio of PEGDA to decellularized BY-2 cells, we achieved an optimal formula (2:1 ratio) that maximized the amount of cellulose within the scaffold while ensuring printing quality. This achievement was crucial for creating scaffolds with desirable properties, such as robustness and microporosity, facilitating mammalian cell integration for future *in vitro* and *in vivo* work.

Our investigation into Young's modulus provided valuable insights into scaffold elasticity and resilience. Through precise control over UV exposure times during the bioprinting process, we demonstrated the tunability of scaffold properties, enabling the creation of scaffolds with tailored mechanical characteristics suitable for diverse tissue types.

Overall, our findings underscore the versatility and potential of 3D bioprinting technology in fabricating customizable scaffolds for tissue engineering and regenerative medicine. By combining advanced fabrication techniques with a deep understanding of scaffold properties, we can pave the way for the development of innovative tissue constructs tailored to meet specific therapeutic needs. Having determined the optimal formulation, the next step involves *in vitro* testing. This includes cell culture on the scaffold to assess biocompatibility and evaluation of cell proliferation using a live/dead assay to monitor cell evolution overtime on the scaffold.

Chapter 3

Exploring the Biocompatibility and Versatility of 3D Printed Plant-Based Scaffolds in Tissue Engineering: Insights from In Vitro Experiments

3.1 Introduction

Three-dimensionally (3D) printed plant-based scaffolds are a new innovative approach in tissue engineering, offering a multitude of potential applications. To pursue this goal, *in vitro* experiments must be conducted to understand how cellular attachment, growth, and survival will be impacted; prior to conducting *in vivo* studies[172].

As mentioned above, this chapter is focused on validating *in vitro* biocompatibility of our scaffolds, as it is a mandatory step that must be completed before progressing to *in vivo* studies. Cell proliferation and viability in said scaffolds will be studied, to confirm that an organism could potentially safely adopt it as a tissue building matrix. This shows us insights into cell communication and regulation, which are fundamental for tissue development and maintenance[173]. By carefully seeding cells onto the scaffold surface, we can observe whether they successfully adhere and proliferate on the material, or if they reject it as a growing support. This will provide valuable information on cell-scaffold interactions[174,175]. Evaluating the behaviour of actin within the cells on the scaffold provides a deeper understanding of the cell morphology and cytoskeleton organization. Actin is a fundamental component of the cytoskeleton, playing a crucial role in maintaining cell shape, enabling movement, and facilitating intracellular transport[176]. By staining actin, we can visualize the cytoskeleton's structure and organization, which indicates whether the scaffold processes suitable surface chemistry for cell attachment, proliferation, and differentiation[177,178,179]. Additionally, assessing scaffold quality through staining is vital. While Congo Red staining is commonly used to visualize amyloids, it is also valuable for staining cellulose in scaffolds, aiding in the identification of the cellulose within decellularized BY-2 [180–184]

. Assessing scaffold quality involves determining the integrity, composition, and distribution of scaffold components, which can influence cell behaviour and tissue regeneration outcomes[185–187].

Monitoring cell proliferation over time offers insights into their growth dynamics and behaviour on the scaffold substrate, further elucidating the scaffold's suitability for tissue engineering applications[131,188–190]. A reliable method for this assessment involves calculating proliferation from day 1 onwards and assessing the ratio of live to dead cells[56]. This assay helps determine whether the scaffold promotes cell viability. Conducting such assays before *in vivo* experiments is crucial as it informs us about the scaffold's potential integration into the mammalian body. If the cells fail to survive the experiments, it indicates poor biocompatibility, eliminating the opportunity for *in vivo* testing[190,191].

A previous study explored decellularized plant tissue as a scaffold for 3D *in vitro* neural stem cells (NSC) culture, showing that plant cellulose scaffolds supported NSC attachment, proliferation, and increased expression of neuron-specific markers, enhancing differentiation compared to 2D polystyrene cultures [112]. These findings suggest a plant-derived cellulose scaffolds are promising for neural tissue engineering and direction NSC differentiation[112]. 3D *in vitro* models better mimic the complex cellular interactions of native tissues compared to 2D models, therefore reducing the need for animal testing and addressing ethical concerns associated with such practices. Although still in development, 3D engineered tissue models show promise in drug testing, therapy screening, and studying disease mechanisms[192].

This study will conduct *in vitro* experiments on 3D printed scaffolds to test the biocompatibility by assessing cell adhesion with NIH 3T3 cells. NIH 3T3 mouse embryonic fibroblast cell line was chosen for their significant role in tissue healing and extracellular matrix placement[193]. These cells are widely used globally because they grow well, are well-characterized, and have been employed in numerous scaffold studies, including those involving plant-based scaffolds[194–198]. NIH 3T3 cells are well-known for their robust growth properties and

reproducibility, making them an ideal choice for assessing biocompatibility in various experimental settings[199].

Additionally, a live/dead assay will evaluate cell proliferation, providing a comprehensive understanding of *in vitro* assays. By only validating the presence of cells in the scaffolds, we cannot make conclusions about their capacity to maintain and promote cell life. A live/dead assay aims to validate that the said cells are indeed proliferating in time and colonizing the scaffold with new healthy cells. This will allow us to compare our different scaffold formulations and see if some will improve cell survival in time.

3.2 Materials and Methods

3.2.1 Mammalian Cell Culture

NIH 3T3 cell lines from mouse fibroblasts were used as the primary cell model (ATCC, Cedarlane). These cells were cultured under standard conditions using high-glucose DMEM (Cytiva Hyclone), supplemented with 10% fetal bovine serum (FBS) (Hyclone Laboratories Inc.) and 1% penicillin/streptomycin (100 U/mL and 100 µg/mg respectively) (Hyclone Laboratories Inc.). Cultures were maintained at 37 °C with 5% of CO_2. To ensure optimal growth and viability, sub-culturing was performed upon reaching approximately 80% confluence.

3.2.2 *In Vitro* Cell Culture on Cellulose Scaffolds

Building upon the decellularized BY-2 scaffold discussed in Chapter 2, the NIH 3T3 cell line was employed for *in vitro* cell culture experiments on these scaffolds. Each scaffold was placed in the well of a twelve-well plate. To avoid contamination, all scaffolds were sterilized with 70% ethanol overnight followed by seven saline washes. Afterward, the scaffold was rinsed with culture media and incubated for 1 hour before media removal. A total of $9*10^4$ cells were deposited on

each scaffold in a volume of 90µL and incubated for 3 hours at 37°C. 1mL of culture media was then added to each well and changed every second day of incubation.

The experiment employed two types of scaffolds: one consisting solely of PEGDA and the other combining PEGDA with decellularized BY-2 cells. Both scaffolds were a haystack shaped 10x10 mm with 9 pores of 2x2 mm each.

The experiment setup spanned a duration of 10 days, during which the scaffolds were collected on day 1, 5, and 10 for immunofluorescence staining, imaging, and cell quantification. This approach allowed for a comprehensive evaluation of cell attachment, proliferation, and scaffold biocompatibility over time.

3.2.3 Immunofluorescence Staining

The NIH 3T3 cells were stained to visualize the actin cytoskeleton and nucleus of mammalian cells. To achieve this, scaffolds were first gently washed with 1X phosphate buffered-saline (PBS) (Fisher) and fixed in 10% formaldehyde for 15 minutes at room temperature (RT) (Sigma-Aldrich). Scaffolds were then washed for 3x10 minutes in 1X PBS and permeabilized with 0.05% Triton X-100 (Mp chemicals), at 37°C for 3 min. Two additional washes were done for 15 minutes each in 1X PBS + sodium azide and FBS.

Actin staining was performed using phalloidin conjugated to Alexa Fluor 488 (Invitrogen) at a concentration of 10 µg/ml, and nuclei were labelled with 7.14 µg/ml DAPI (Invitrogen) incubating together at RT for 30 minutes. Cells were then washed in 1X PBS + 0.05% Tween-20.

Additionally, 20 µg/ml Congo Red (Sigma) was used to stain the cellulose for 5 minutes. Finally, the samples were then mounted in Vectashield mounting media (BioLynX VECTH1000) for visualization.

Cell viability was also assessed using a live/dead assay. They were stained with 10 µg/ml Hoechst 33342 (Invitrogen) and 1µg/ml Propidium iodide (PI) (Invitrogen), for 15 minutes, at 37°C. Cells were then washed 1X PBS, at 37°C, for 5 minutes. Following staining, the cells were fixed with 10% formalin (Sigma-Aldrich) to preserve the staining pattern.

3.2.4 Optical Microscopy

Confocal imaging was performed using A1R high-speed laser scanning confocal system (Nikon) on a TiE inverted optical microscope platform with appropriate laser lines and filter sets. Transmitted light images were acquired on an inverted TiE microscope (Nikon, Canada) with phase contrast optics. Before imaging, the scaffolds were placed on coverslips with mounting media (Vectashield H-1000). The samples were imaged with 4X, 10X and 40X lenses, and the images presented throughout this chapter are Maximum Intensity Projections. The brightness of the fluorophore signal was enhanced to improve the contrast of structures. All images were analyzed using ImageJ software.

3.2.5 Statistical Analysis

Student's *t* tests (paired) were utilized for comparing two samples in all analyses. Statistical significance was obtained by using Graphpad Prism Software, with significance donated by an asterisk (*) indicating a P-value < 0.05.

3.3 Results and Discussion

3.3.1 Triple Stain Test

The aim of our experiments was to assess biocompatibility, this was achieved by first evaluating cell adhesion and proliferation. NIH 3T3 mammalian cells were seeded at a density of $100x10^6$ cells per ml. Following a 7-day incubation period, the cells exhibit attachment and elongation, particularly within the porous regions of the scaffold. The scaffold was intentionally designed, and 3D printed using Tinkercad software. It featured a haystack shape with dimensions of 10x10 mm and containing 9 pores, each measuring 2x2 mm. These pores were purposefully incorporated to enhance cell infiltration and influence the distribution of cells on the scaffold.

The actin staining technique provided valuable insights into the cell attachment and distribution in the scaffolds. Cell attachment and distribution on a scaffold are important in tissue engineering, as they impact the integration of the scaffold with the tissue and the functional capacity of the repaired tissue[178,200,201].

Figure 18 demonstrates the attachment of the cells onto the scaffold, using Congo Red to stain cellulose, phalloidin to stain actin filaments, and DAPI to stain cell nuclei. Specifically, **Figure 18A** offers a view of the scaffold's porous structure, emphasizing the effective cell colonization within these pores. Qualitative observations revealed a higher density of cells attaching to the inner surface of the pores, compared to the top surface of the scaffold, highlighting the importance of the scaffold's geometric feature and size.

Meanwhile, **figure 18B** provides a higher magnification view of the actin stain, facilitating the visualization of cell morphology and cytoskeleton organization[177,178]. **Figure 18C** shows a detailed view of the stress fibres, which are prominent bundles of actin filaments within the cytoskeleton. These fibres play a crucial role in maintaining cell shape, generating contractile forces, and enabling cell motility.

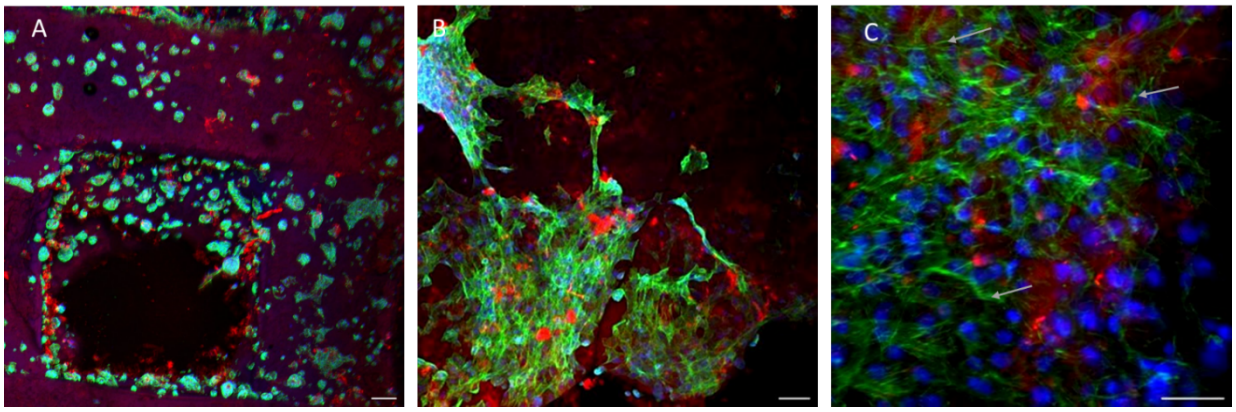

Figure 18: Growth of 3T3 Mouse Embryonic Fibroblasts on Hydrogel Scaffolds.

The cells were stained with DAPI (blue for nuclei), Phalloidin 488 (green for actin), and Congo Red (red for cellulose) on the PEGDA+BY-2 scaffold. **Image A** shows a wide-field (4X) view of the scaffold, highlighting its porous structure and the surrounding areas beside the pores, illustrating the distribution of cells across the scaffold. **Image B** provides a magnified view (10X) of the areas adjacent to the pores, detailing actin structures, while **Image C** offers a closer look (40X) of the same area, clearly showing the stress fibres (indicated by gray arrow). Confocal microscopy was used to capture the images, which were then analyzed using Nikon software and ImageJ, demonstrating successful cell attachment to the scaffold. Scale bar A: 200 µm, Scale bar B: 100 µm, Scale bar C: 50 µm.

3.3.2 Live/Dead Assay

To evaluate cell proliferation on PEGDA and PEGDA +BY-2 scaffolds, we assessed the number of cells on each scaffold on days 1, 5, and 10, by staining the cells on the scaffolds with Hoechst 3332 and Propidium Iodide (PI). In **Figure 19 A-C**, the two-colour filters were separated in the software Fiji, facilitating cell counting. Hoechst, capable of permeating cell membranes to label DNA in both living and dead cells, was employed to mark the total number of cells. Conversely, PI selectively infiltrates cells with compromised plasma membranes, highlighting only dead cells in red[202]. Importantly, the cells were not permeabilized prior to staining. This is crucial because it ensures that PI only labels dead cells with damaged membranes, providing an accurate measure of cell death. To determine the number of live cells, we counted them in 3 fields of view (FOV) per scaffold, using three scaffolds per condition (n=9 per condition) and repeated the experiment three times. The live cell count was obtained by subtracting the number of dead cells (PI-positive) from the total cell count (Hoechst-positive). This method provides an evaluation of cell viability and proliferation over time.

Previous research on PEGDA has demonstrated its capacity to support cell growth and development *in vitro*[203]. With that said, our goal was to assess whether the addition of BY-2 decellularized cells to PEGDA in hydrogel form would yield similar or improved outcomes to PEGDA alone. The experiment was repeated 3 times, and consistent trends were observed across all 3 iterations. While it appears that BY-2 may assist in cell attachment, this experiment did not reveal any negative impact associated with its inclusion. As shown in **Figure 19A**, PEGDA and PEGDA + BY-2 were compared using the student's T-test each time point was assessed; day 1 and day 5 show that PEGDA +BY-2 has significantly more growth than PEGDA alone, with $p=0.0196$ and $p=0.0004$ respectively. At day 10 $p= 0.128$, there were no statistically significant differences observed.

The assessment of cell proliferation involves comparing cell counts at day 1, day 5, and day 10, utilizing both live and dead cell data. **Figure 19B** presents the PEGDA only scaffold, while **Figure 19C** illustrates the scaffold with PEGDA and decellularized BY-2 plant cells. Notably significant differences were observed between live and dead cells at day 1 for both PEGDA ($p = 0.0046$) and PEGDA + BY-2 ($p = 0.0001$). Similarly, at day 5, significant differences were noted for PEGDA ($p = 0.0295$) and PEGDA + BY-2 ($p < 0.0001$). However, by day 10, while statistically significant differences were found for PEDGA + BY-2 ($p= 0.0377$), no significant differences were observed for PEGDA alone, although it showed a similar trend. Those consistent findings suggest that the presence of BY-2 does not negatively impact the scaffold, further supporting its compatibility with the 3D printed scaffold. **Images 19C, 19D and 19E** depict the differences observed at each time point for the PEGDA + BY-2 condition.

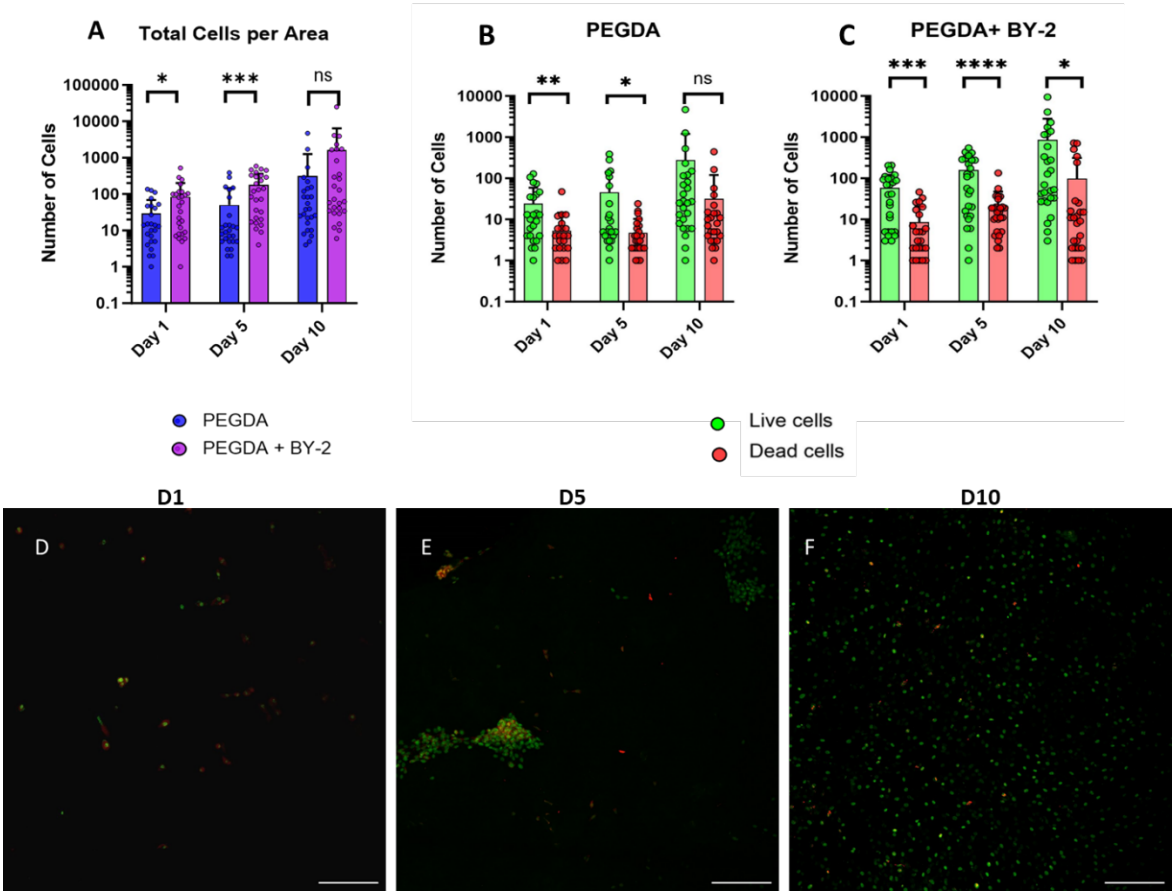

Figure 19: Live/Dead Assay.

Graph A shows the number of cells attached to the PEGDA scaffold compared to PEGDA +BY-2 scaffolds in a 1.6 μm^2 FOV at multiple time points (day 1, 5, and 10), with the scale presented in logarithmic format. Hoechst 33342 (green) staining for all cells and PI (red) for dead cells. Graphs **B** and **C** showcase the live and dead cells between the 3 different time points (day 1, 5, and 10). Each band represents the average of three FOVs analyzed on three different scaffolds, for three experiment repetitions. Figure D-F demonstrates representative examples of confocal microscopy images (40X) of PEGDA+BY-2 scaffolds at each time point. Confocal microscopy captured images, followed by analysis using Nikon software and ImageJ. Scale bar for Figures D, E and F: 200 µm.

3.4 Conclusion

In conclusion, this assessment involves meticulous evaluation of scaffold properties through *in vitro* assays, ensuring the suitability of these scaffolds for *in vivo* implantation. Before transitioning to *in vivo* experiments, it is crucial to evaluate the biocompatibility of materials. This underscores the importance of robust biological tests, such as assessing cell attachment through actin and nuclei staining, as well as live/dead assays, which aid in determining cell proliferation and biocompatibility.

A previous study on inverse opal extracellular matrix scaffolds demonstrated improved survival, viability, and paracrine activities of stem cells, leading to enhanced vascular network formation and recovery in critical limb ischemia models[204]. This highlights the significance of scaffold architecture in promoting cell viability and integration, a factor that parallels the goals of our 3D-printed plant-based scaffolds in ensuring cellular attachment, growth, and successful tissue integration[204].

In vivo testing refers to experiments conducted within a living organism, typically using animal models. These tests are crucial because they provide comprehensive insight into the biological interactions of the scaffold within a complex living system, which cannot be fully replicated *in vitro*. *In vivo* testing involves evaluating the scaffold's integration, its effect on surrounding tissues, and its overall biocompatibility and functionality within the organism.

Animal *in vivo* testing is performed to validate the applicability of biomedical materials and gain insight into whether they will perform as expected in a human being. This step is essential to identify any potential adverse reactions, such as immune responses, inflammation, or toxicity, which may not be apparent during *in vitro* testing.

Based on the results obtained in this chapter, I can assert that the 3D printed plant-based scaffold demonstrates biocompatibility *in vitro,* as evidenced by the absence of adverse outcomes during cell culture experiments

Chapter 4

Exploring the Biocompatibility and Versatility of 3D Printed-Based Scaffolds in Tissue Engineering: Insights from In Vivo Experiments

4.1 Introduction

Conducting *in vivo* assays for biomaterials is a cornerstone of tissue engineering. Prior *in vitro* work is essential to ensure the preparation and viability of materials before they are tested in living organisms[205]. The 3Rs- Replacement, Reduction, and Refinement- are fundamental principles guiding ethical research involving animals[206–210]. Replacement involves using alternative methods or technologies to replace the use of animals in experiments[211–213]. Reduction focuses on minimizing the number of animals used, optimizing study designs, and employing advanced data analysis techniques to obtain comparable levels of information with fewer animals[214]. Finally, Refinement aims to enhance animal welfare by improving housing, handling, and experimental procedures to minimize pain, suffering, and distress thereby ensuring better conditions for the animals involved in research[215–217].

Once those 3Rs are thoroughly considered and the *in vitro* process is approved by the Animal Care Committee, we can proceed with *in vivo* assays, still adhering to the principles of the 3Rs. Various types of *in vivo* studies can be conducted using different animals and procedures in tissue engineering. For example, one study transplanted embryonic feline CNS tissue into chronic spinal cord lesions in adult cats to evaluate the potential of using these transplants for spinal cord repair[218]. Another study performed an open-heart procedure to implant engineered tissue with myogenic progenitor cells into the atrioventricular groove of a rat heart, aiming to create an electrical conduit as an alternative to pacemakers for pediatric heart block patients[219].

Recent *in vivo* research has also explored 3D printing. For example, the fabrication of porous 3D-printed chitosan scaffolds for skin tissue regeneration demonstrated enhanced tissue restoration in diabetic rats compared to commercial patches and spontaneous healing[187,220].

Decellularized plant materials have shown significant promise as biomaterials for *in vivo* applications, owing to their biocompatibility and structural properties. For instance, in a recent study, cellulose scaffolds derived from decellularized apples were subcutaneously implanted in wild-type, immunocompetent mice[54]. Over an 8-week period, histological analysis revealed a diminishing foreign body response, along with active fibroblast migration, deposition of new collagen extracellular matrix, and robust blood vessel formation within the scaffold[54]. Another study utilized biomimetic bioceramic scaffolds inspired by succulent plants, fabricated with a 3D printing and implanted into the lateral femoral condyles of rabbits[221]. This research demonstrated that these scaffolds effectively promote cell distribution, interactions, and osteogenic differentiation, accelerating bone regeneration[221]. These findings underscore the scaffold's pro-angiogenic properties and its potential as an advanced biomaterial in tissue engineering and regenerative medicine.

This project will compare two types of 3D printed scaffolds: one made solely of PEG-diacrylate (PEGDA) and another incorporating decellularized BY-2 plant cells into the PEGDA, as discussed in chapters 2 and 3. The aim is to determine whether adding BY-2 decellularized plant cells enhances the biocompatibility of the PEGDA scaffold. Previous studies have shown that PEGDA hydrogels, when implanted subcutaneously in nude mice, maintained the fibroblast phenotype of encapsulated T31 human tracheal scar fibroblasts and promoted extracellular matrix secretion, demonstrating PEGDA's potential for supporting cell proliferation and growth in tissue engineering applications[222].

Our study will investigate whether cellulose can further improve the performance of PEGDA, given its established biocompatible properties. Over a 12-week period, we will observe the outcomes at 4, 8 and 12 weeks, comparing the results between rats implanted with the PEGDA only scaffold and those with the PEGDA scaffold combined with decellularized BY-2 plant cells.

4.2 Materials and Methods

4.2.1 Animals

All experimental procedures were approved by the Animal Care and Use Committee of the University of Ottawa. Female Sprague Dawley rats, aged 6-8 weeks and weighing 250-350 grams (N=24), were used in the study (bred at Charles River Laboratories). The animals were maintained at a constant room temperature of ±22°C and a humidity level of approximately 52% daily. They were fed a standard diet containing 18 grams of protein and were kept under a controlled 12 hours light/dark cycle. Rats are tickle trained the week before surgery and have playtime once a week until euthanasia, which involves the refinement in the 3Rs principles[223].

4.2.2 Cellulose Scaffold Preparation

Building upon the decellularized BY-2 scaffold discussed in Chapter 2, we prepared two types of scaffolds: one as control with only 3D printed PEGDA and the other 3D printed with PEGDA and decellularized BY-2 cells (cellulose). We chose a cylindrical scaffold shape with a circumference of 3.17cm with 9 pores, each with a circumference of 3.7 mm. The scaffolds were printed using the Lumen-X Bio-printer with UV light exposure set to 10 seconds. To minimize irritation, from sharp corners rubbing against the internal surfaces of the animals, we opted for cylindrical scaffolds instead of the previously used square scaffolds. Both types of scaffolds were prepared using the same method. They were washed with saline for 1 week to remove the photo-initiator. To ensure sterility, all scaffolds were sterilized with 70% Ethanol overnight, followed by 7 through saline washes.

4.2.3 Cellulose Implantation

Rats received pre-operative analgesia via a subcutaneous injection of Buprenorphine (0.05 mg/kg) on the morning of surgery, rats underwent anesthetic induction with 2% isoflurane O_2 at 2L/min, and maintenance at 3%. They were weighted, induced, and prepared for surgery with aseptic

techniques. Positioned on a heating pad, their eyes are protected with tear gel, and hydration is maintained with saline 10mg/kg. Skin preparation includes shaving, vacuuming, and scrubbing with 4% chlorhexidine gluconate. Buprenorphine HCl is administered at the midline of the neck, followed by a final aseptic scrubbing with Soluprep (2%chlorohexidine gluconate and 70% ethanol). Four 1 cm linear incisions are made lateral to the midline as indicated in Figure 1. The scaffolds are introduced into the subcutaneous space, and incisions are closed with 6-0 Prolene, and Bupivacaine 2% transdermal is applied. Each rat received 4 scaffolds, 2 on each side. Animals were recovered from anesthesia in a recovery incubator at 35ºC with oxygen, and they were monitored until they regained consciousness. They receive Buprenorphine SR 1mg/kg 4 hours after receiving their initial Buprenorphine HCl. Enrofloxacin (Baytril) 10ml/kg is administered for 3 days perioperatively. To prevent suture removal, animals are separated for 2-3 days post-operative, and given Nobbily Wobbly toys filled with food pellets and treats such as yogurt drops, banana chips, fruity bites, ABC fruit blend, mealworms and veggies-bites (all from Cadarlane Bio-Serve) placed in each cage to keep them occupied. Teats are replenished during post-op monitoring and discontinued when the rats are reintroduced. Post-operative care includes monitoring various indicators, including pain assessment through the grimace score, which evaluates facial expressions like orbital tightening, nose bulging, ear position, and whisker movement to detect discomfort in rodents. Additionally, porphyrin secretion, food intake, incision condition, activity levels,

respiratory function, weight loss, and dehydration are carefully observed to ensure effective recovery.

Figure 20: Implant numbering

This schematic illustrates the numbering of the implant sites on the rat's back. Four 1 cm linear incisions are made lateral to the midline, with each rat receiving four scaffolds, two on each side. The numbering of the implant sites is as follows: Site 1 and Site 3 on the left side, and Site 2 and Site 4 on the right side. The implants are positioned on the back to ensure they are harder for the rat to access post-operatively, reducing the likelihood of interference with the sutures and facilitating easier monitoring and evaluation. Additionally, this location is chosen because the back has fewer vital organs, making it easier to open and monitor the surgical sites while minimizing risk for the animal.

4.2.4 Scaffold Resections

At 4-, 8- and 12-weeks post scaffold implantation, 8 rats per time point were euthanized using isoflurane followed by CO_2 exposure and cardiac cut. The area over the implants was shaved, and subcutaneous layers were carefully separated to avoid implant damage, yielding a rectangle of skin containing the 4 implants. The implants were resected including a 1-2mm perimeter of healthy skin and transferred into 10% formaldehyde (Sigma-Aldrich) in 48 hours. Samples were then moved to 70% ethanol and stored at 4 degrees. If additional trimming was required, the implants

were post fixed in formalin for a further 48- hours before being transferred into ethanol storage. Finally, samples were embedded in paraffin by the PALM Histology Core Facility of the University of Ottawa.

4.2.5 Histological Analysis

Serial 4µm thick sections were cut from inside the scaffold and stained with hematoxylin-eosin (H&E) and Masson's trichrome (MT). This histological processing and staining were performed by the PALM Histology Core Facility of the University of Ottawa. For immunocytochemistry, the tissue sections were using the Leica Bond^{TM} system using a modification of protocol F that eliminates the post primary step when using rabbit antibodies on rat tissues. Sections stained with Rabbit anti-CD45 or Rabbit anti-CD31 were pre-tested using heat mediated antigen retrieval with Sodium Citrate buffer (pH 6.0, epitope retrieval solution 1) for 20 minutes. The sections were then incubated using 1:1600 dilution for anti-CD45 or 1:100 for anti-CD31 (both from abcam) for 30 minutes at room temperature and detected using an HRP conjugated compact polymer system. Slides were then stained using DAB as the chromogen, counterstained with Hematoylin, mounted and cover slipped. Micrographs were captured using Zeiss MIRAX MIDI Slide scanner equipped with 20X objective and analyzed using Zeiss ZEN software. A pathologist analyzed the images to evaluate cell infiltration, extracellular matrix deposition, and vascularization.

4.3 Results and Discussion

4.3.1 Explanation of the 4 Stains

In this study, we used four different stains to analyze the scaffolds.

Hematoxylin and Eosin (H&E): Hematoxylin stains cell nuclei a deep blue-purple, while eosin stains the extracellular matrix and cytoplasmic components in varying shades of pink and red, providing a clear contrast that highlights the tissue structure and cellular infiltration within the scaffolds[224].

Masson's Trichrome (MT): This stain is used to differentiate between various tissue components[225,226]. This method stains collagen fibres blue or green, muscle fibres red, cytoplasm light red or pink, and nuclei dark purple or black[227]. It is particularly useful for assessing the presence and organization of connective tissue, such as collagen, in tissue samples, providing clear and distinct colour contrasts to aid in the analysis of tissue structure and composition.

CD45 Staining: CD45, also known as leukocyte common antigen, is a protein expressed on the surface of all nucleated hematopoietic cells (white blood cells)[228]. We used an anti-CD45 antibody against this protein to highlight immune cells, providing valuable insights into the inflammatory response to the implanted scaffold. CD45-positive cells are stained brown.

CD31 Staining: CD31, also known as platelet endothelial cell adhesion molecule (PECAM-1), is a marker specific to endothelial cells that line blood vessels[229,230]. We used an anti-CD31 monoclonal antibody to stain these cells, providing clear evidence of new blood vessel formation within the scaffold.

4.3.2 Comparison Between PEGDA+ BY-2 and PEGDA

This experiment was conducted to compare PEGDA + BY-2 and PEGDA scaffolds to evaluate the potential benefits of incorporating decellularized BY-2 plant cells into 3D printed scaffolds. We studied 12 rats per condition, for a total of 24 animals. Each group was divided

between three time points: 4, 8 and 12 weeks of study (giving a total of 4 rats per time point). Each animal received four subcutaneous scaffold implants: the first twelve rats received PEGDA + BY-2 formulated scaffolds, while the remaining received PEGDA formulated scaffolds. We therefore had 4 rats receiving each type of scaffold for a total of three time points.

We provide in **Figure 21** a clear comparison between the structural integrity of PEGDA + BY-2 and PEGDA scaffolds over the 12-week period. The use of Masson's Trichrome (MT) stain reveals that the PEGDA+BY-2 scaffold maintains its cylindrical shape and porous structure (3.17 cm circumference with 9 porous, each 3.7 mm in circumference) at weeks 4, 8, and 12 (**Figure 21A**, **21B** and **21C**).

Upon closer inspection of the images, several observations can be made that lead to this conclusion. In the PEGDA+BY-2 scaffold images (**Figure 21A**, **21B**, and **21C**), the cylindrical shape is consistently preserved, and the pores remain well-defined and intact throughout the 12-week period. The MT stain shows a uniform blue coloration indicating the presence of collagen, which suggests that the scaffold maintains its structural integrity and supports extracellular matrix deposition.

In contrast, the PEGDA scaffold images (**Figures 21D**, **21E**, and **21F**) show signs of structural degradation. The cylindrical shape is less defined, and the pores are irregular and less distinct as time progresses. The MT stain reveals areas of disruption and gaps within the scaffold structure, indicating a breakdown of the material. The loss of the uniform blue coloration suggests compromised scaffold integrity, leading to a loss of its original shape and porous architecture.

This observation aligns with the findings in Chapter 2, where Young's Modulus results indicated that the PEGDA + BY-2 scaffold possesses superior mechanical properties compared to the PEGDA scaffold alone. The hydrogel-like properties of the PEGDA + BY-2 scaffold contribute to its resilience during the sectioning process, supporting its potential for use in

tissue engineering applications where structural integrity is important[231–233]. The higher mechanical stability of the PEGDA+ BY-2 scaffold, as evidenced by both Young's modulus measurements and the visual assessments in **Figure 21**, underscores its suitability for long-term implantation and functionality in biological environments. The consistent preservation of the scaffold's shape and pore structure over 12 weeks further supports its potential to provide a stable framework for cellular growth and tissue development, crucial for successful tissue engineering applications.

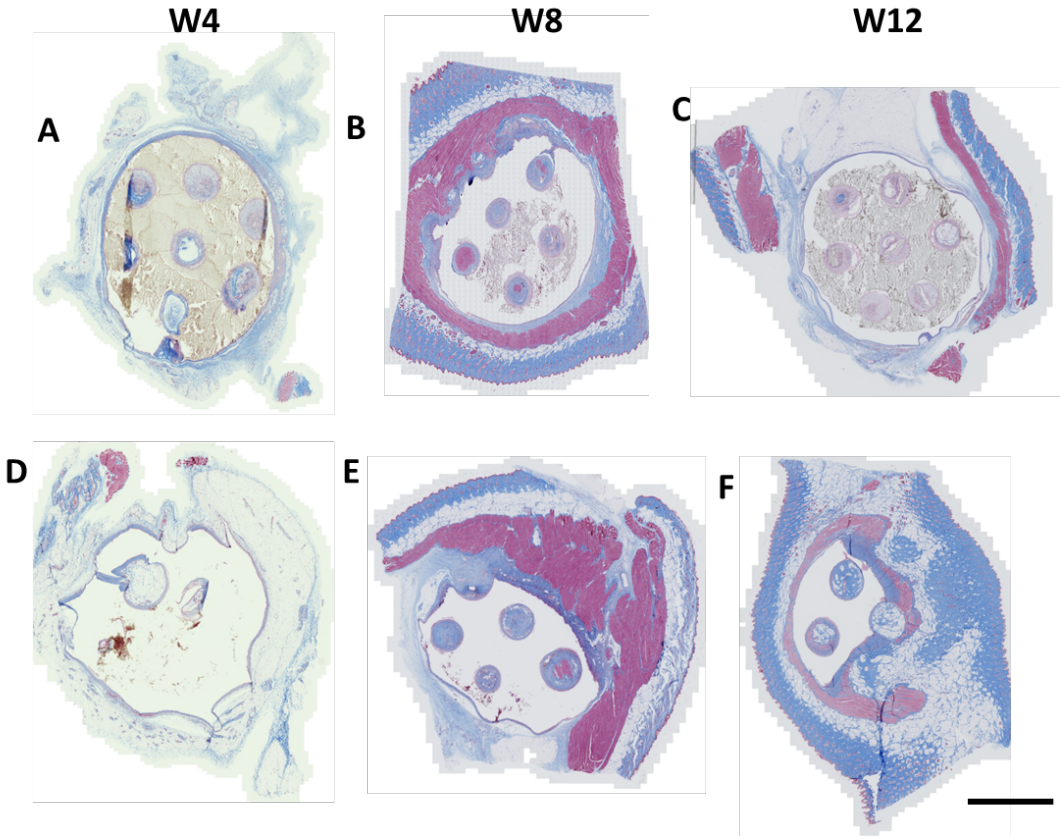

Figure 21: Scaffold Shape Comparison Between PEGDA + BY-2 and PEGDA.

Masson's Trichrome stain was used to visualize the cylindrical shape of the scaffolds. PEGDA+BY-2 scaffolds are showcased at weeks 4 (A), 8 (B) and 12 (C) after the procedure. Similarly, images D, E and F showcase the same timeline for PEGDA only scaffolds, at weeks 4, 8 and 12 respectively. Slides were captured using Zeiss MIRAX MIDI Slide scanner equipped with 20X objective and analyzed using Zeiss ZEN software**.** Scale bar: **A-F** = 0.5 cm.

In addition to these findings, we used three additional stains in synergy with MT to further investigate how the surrounding tissues reacted to the inserted scaffolds. We used H&E staining to assess the histological features

The global view in the figure indicates that the PEGDA+ BY-2, **Figure 22A**, scaffold maintained its structural integrity and porous architecture better than the PEGDA only scaffold, **Figure 23A**. Histochemical staining results reveal that while there are differences between the two scaffold types, we can still see collagen infiltration around the implants with the MT staining (**Figures 22A and 23A**) In examining the H&E staining (**Figures 22B and 23B**), immune cells which typically appear as small darkly stained nuclei from the surrounding tissue, were not observed. This lack of distinct darkly stained nuclei indicative of immune cells suggests an absence of inflammation. Similarly, CD45 (**Figures 22D and 23D**), which specifically labels leukocytes, showed no positive staining in either scaffold type, further confirming the absence of an immune response. The combined lack of immune cells in both H&E and CD45 staining suggests that there was no immune response ongoing at the time of analysis, indicating good biocompatibility of the scaffolds.

This shows that neither PEGDA alone nor the addition of BY-2 elicits a strong immune response. However, despite this, the PEGDA scaffolds showed signs of structural degradation over time, likely due lack of consistent mechanical strength, as discussed in Chapter 2 with Young's modulus analysis. In contrast, the PEGDA+ BY-2 scaffold, depicted in MT-stained images (**Figure 22A**) and close-up images of MT and H&E (**Figures 22C** and **22D**), demonstrated enhanced scaffold still being intact, cell infiltration and tissue integration. These findings indicate that the addition of BY-2 plant cells creates a more hydrogel-like structure, providing better mechanical support and maintaining the scaffold's shape and porosity, as intended by the 3D printing process.

Overall, the PEGDA+BY-2 scaffold has superior performance in maintaining structural integrity and promoting cell infiltration. This is consistent with the hypothesis that the inclusion of

BY-2 cells enhances the scaffold's mechanical properties and biological compatibility, reducing the likelihood of scaffold breakage and degradation. The enhanced mechanical properties of the PEGDA+BY-2 scaffold can be attributed to the hydrogel formation, which improves its durability and functionality. This makes PEGDA+BY-2 a more promising option for tissue engineering applications where long-term scaffold integrity and cell integration are crucial.

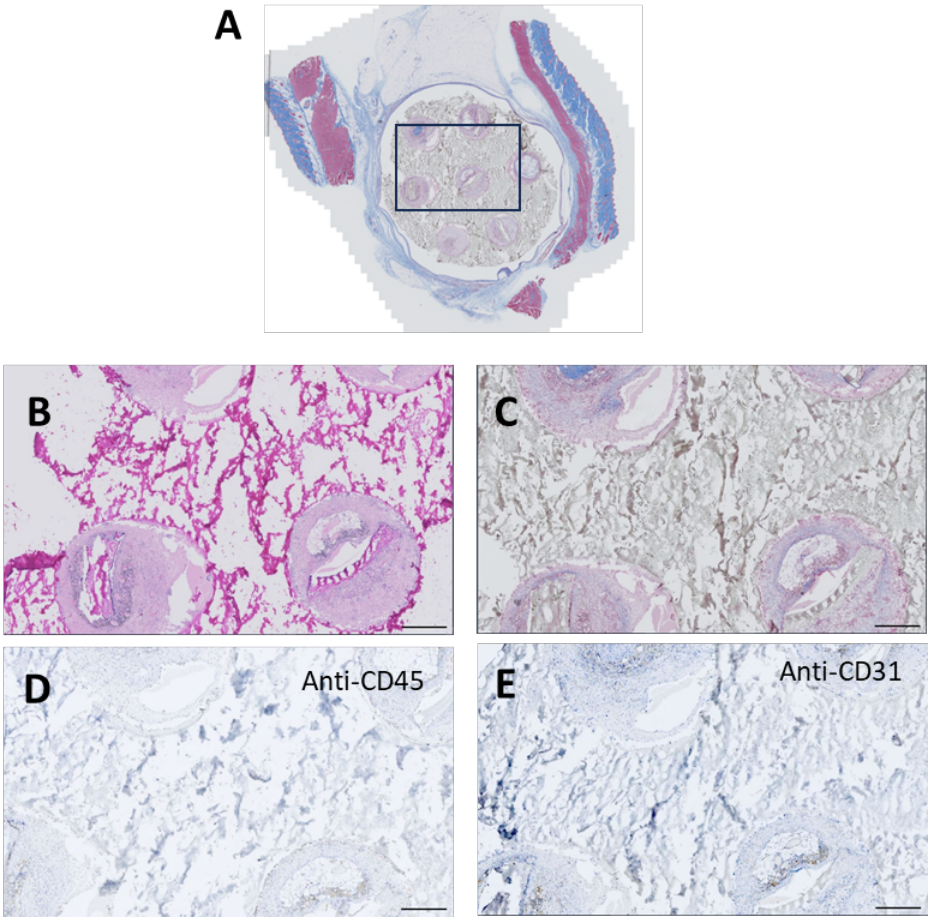

Figure 22: Comparison of **PEGDA + BY-2 scaffold with different staining approaches.**

This figure compares axial sections of representative 3D-printed scaffolds at week 12 post-implantation. Image A shows the PEGDA+BY-2 scaffold stained with MT, with close-up images (B-C) illustrating H&E and MT staining. Image D showcases a zoom-in image stained with anti-CD45 and Image E anti-CD31. Scale bars: B-E = 500 μm.

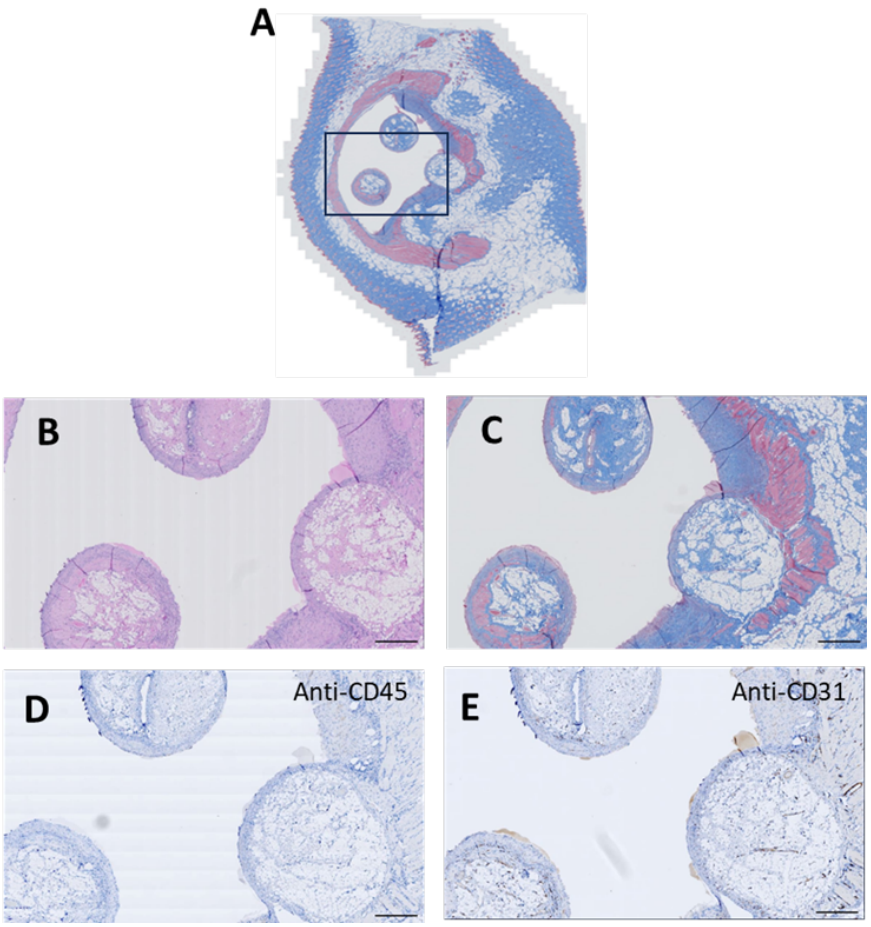

Figure 23: Comparison of PEGDA scaffold with different staining approaches.

This figure compares axial sections of representative 3D-printed scaffolds at week 12 post-implantation. Image A shows the PEGDA scaffold stained with MT, with close-up images (B-C) illustrating H&E and MT staining. Image D showcases a zoom-in image stained with anti-CD45 and Image E anti-CD31. Scale bars: B-E = 500 µm.

4.3.3 Observation of Decellularized BY-2

This section aims to show that the decellularized BY-2 plant cells persist within the scaffold both before and after implantation. **Figure 24** illustrates the presence of these BY-2 shapes in the scaffold through MT staining. **Figure 24A** presents a scaffold that has been paraffin-embedded, sectioned, and stained without implantation, serving as a baseline for comparison. The close-up view in **Figure 24C** highlights the distinct shapes of the BY-2 cells within the PEGDA scaffold. The scale bar in both images provides a reference for the size and distribution of these shapes, confirming that they are indeed the BY-2 cells as we showed in Chapter 1, Figure 7.

After 12 weeks of implantation in the rat, the scaffold was again paraffin-embedded, sectioned, and stained, as shown in **Figure 24B**. The close-up in **Figure 24D** reveals that the BY-2 shapes remain intact within the scaffold, even after prolonged exposure to the biological environment of the rat. The arrows in both **Figure 24C** and **24D** indicate the presence of these BY-2 shapes in both pre-and post-implantation images, with the same scale bar used for reference, confirming that these structures are indeed decellularized BY-2 cells. This observation supports the stability and durability of the BY-2 cells within the PEGDA scaffold, suggesting that they can maintain their structure and potentially contribute to the scaffold's functionality over extended periods *in vivo*.

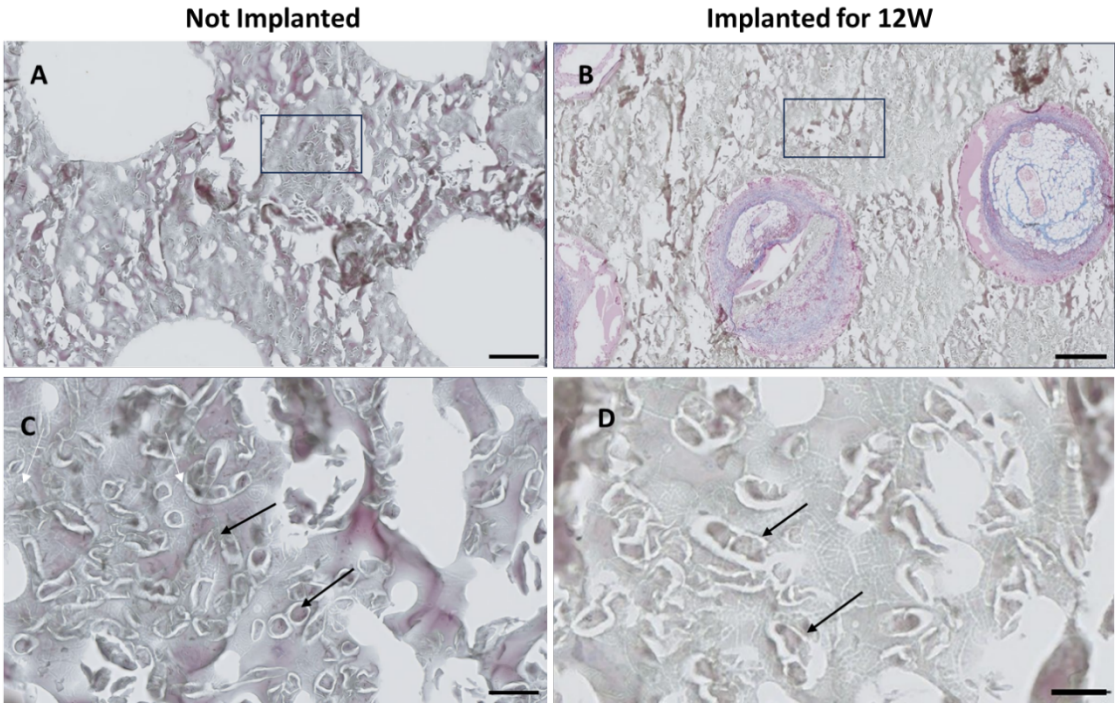

Figure 24: Observation of Decellularized BY-2 in scaffolds before and after implantation.

This figure demonstrates the persistence of decellularized BY-2 after implantation in the rat, with all images stained using MT. Image A showcases a scaffold that has been paraffin-embedded, sectioned, and stained without implantation. Image C provides a close-up of Image A, revealing the BY-2 shapes within the scaffold composed solely of PEGDA and decellularized BY-2. Image B depicts a scaffold implanted in a rat for 12 weeks, then paraffin-embedded, sectioned, and stained. Image D offers a close-up of Image B, showing the BY-2 shapes within the scaffold after 12 weeks in the rat. Arrows in Images C and D indicate the BY-2 shapes. Scale bars: A-B = 500 μm, C-D = 100 μm.

4.3.4 Biocompatibility and Cell Infiltration of the PEGDA+ BY-2 and PEGDA Scaffolds Implants.

Scaffold biocompatibility and cell infiltration were examined using H&E staining of fixed cellulose scaffolds at 4, 8, and 12 weeks following their implantation of the PEGDA scaffold with decellularized BY-2 plant cells, as shown in **Figure 25**.

Global views of the longitudinal sections of representative cellulose scaffolds are displayed in **Figure 25A-25C**. These views reveal that the scaffold maintains its general shape throughout the study timeline, with the porous structure designed for 3D printing remaining clearly visible. **Figure 25D-25F** shows magnified sections of the scaffold perimeter at each time point, corresponding to the highlighted areas in **Figure 25A-25C**. A dense layer of cells infiltrating the scaffold's pores is evident, as indicated by the prominent blue-purple staining.

Interestingly, giant cells, which are typically indicative of a foreign body reaction, were barely observed in the H&E-stained sections[234–238]. Giant cells are multinucleated cells formed by the fusion of macrophages in response to a foreign body. They are a hallmark of chronic inflammation and are often associated with the body's attempt to isolate and degrade a foreign material that it cannot easily phagocytose[239]. The pathologist observed a decrease in giant cells for the PEGDA+ BY-2 scaffold, with more giant cells at week 8 and fewer at week 12. This decrease is normal as the body adapts to the new material[240].

In addition to H&E staining for histological analysis, we performed anti-CD45 staining to evaluate the level of immune cells within the scaffold and the surrounding dermis tissue, as shown in **Figure 25G-I**. If the scaffold were causing adverse immune responses, an increase in leukocyte presence would be expected over time, but this is not observed. This finding, along with the minimal presence of giant cells in the H&E-stained sections, reinforces the favourable biocompatibility of the PEGDA+BY-2 scaffolds.

Figure 26 presents a comparison with PEGDA scaffolds that do not contain decellularized BY-2 plant cells. This figure shows axial sections of representative 3D-printed scaffolds using the same stains as Figure 5 (H&E and anti-CD45). Notably, there are still giant cells after 12 weeks, but it has decreased when we compare them to 4 weeks (evaluated by a pathologist), indicating that the foreign body reaction is getting better over time, similar to the PEGDA + BY-2 scaffold. The key difference lies in the scaffold degradation over time, with the PEGDA scaffold showing more breakdown scaffolds compared to the PEGDA + BY-2 scaffold, which maintains its structure more effectively. This result is consistent with previous findings that PEGDA is non-toxic in the body[241–245]. Since the PEGDA+BY-2 scaffolds also contain PEGDA, any acute toxicity would have been evident in both scaffolds for tissue regeneration.

A pathologist reported that no lymphocytes were observed in the scaffold sections for both the PEGDA and PEGDA + BY-2 scaffolds. This absence of lymphocytes indicates a minimal immune response, suggesting good biocompatibility for both scaffold types.

For the PEGDA scaffold, the pathologist noted the presence of fibrous plugs with dense fibrosis, a few giant cells, calcific material and central acellular material within the implant. Dense fibrosis refers to the thickening and scarring of connective tissue, which is a part of the body's repair mechanism but can sometimes hinder proper tissue integration. This indicates a negative outcome as dense fibrosis can impede the scaffold’s ability to integrate seamlessly with the surrounding tissue, affecting its overall functionality. Calcific material refers to the deposition of calcium salts within the tissue, indicating that there may be ongoing mineralization processes. The body attempts to wall off the scaffold and keep it away from living tissues, essentially trying to reject the scaffold.

The PEGDA + BY-2 scaffold, exhibited multiple fibrous plugs within the implant, along with some calcific material. This response is typical for biomaterials, as the body often recognizes implanted materials as foreign objects and attempts to isolate them[246,247]. The formation of fibrous

plugs and calcific material represents the body's defence mechanism, aiming to protect the surrounding tissues from the foreign scaffold. This process, while indicative of some level of integration, also points to an underlying rejection response[248].

These observations are not uncommon in biomaterial implants and highlight the challenges faced in achieving perfect biocompatibility[249]. While the presence of calcification and fibrosis is not severe, it does indicate that the body is attempting to isolate and eventually remove the scaffold[250]. Therefore, although the PEGDA + BY-2 scaffold shows enhanced structural stability, these findings underscore the need for further research to modify scaffold properties to reduce these negative responses and improve tissue integration.

Overall, these observations suggest that both the PEGDA and PEGDA + BY-2 scaffolds exhibit a biocompatibility profile with minimal severe immune reaction, as evidenced by the lack of lymphocytes and only a few giant cells. However, the presence of calcific material and fibrosis in both scaffold types is an indication of the body’s attempt to reject the implants. The reduced presence of calcific material in some scaffolds of the PEGDA + BY-2 as well as the PEGDA only scaffold, where mineralization The reduced presence of giant cells at later stages (week 12) in the PEGDA + BY-2 and PEGDA scaffolds suggests some degree of long-term biocompatibility and integration. However, the occurrence of calcification and fibrosis indicates that while the scaffolds are not causing severe immune responses, they are still being recognized as foreign bodies that the host tissue is attempting to isolate and remove. This underscores the need for further research to mitigate these negative responses and improve the overall efficacy and biocompatibility of these scaffolds for tissue engineering applications.

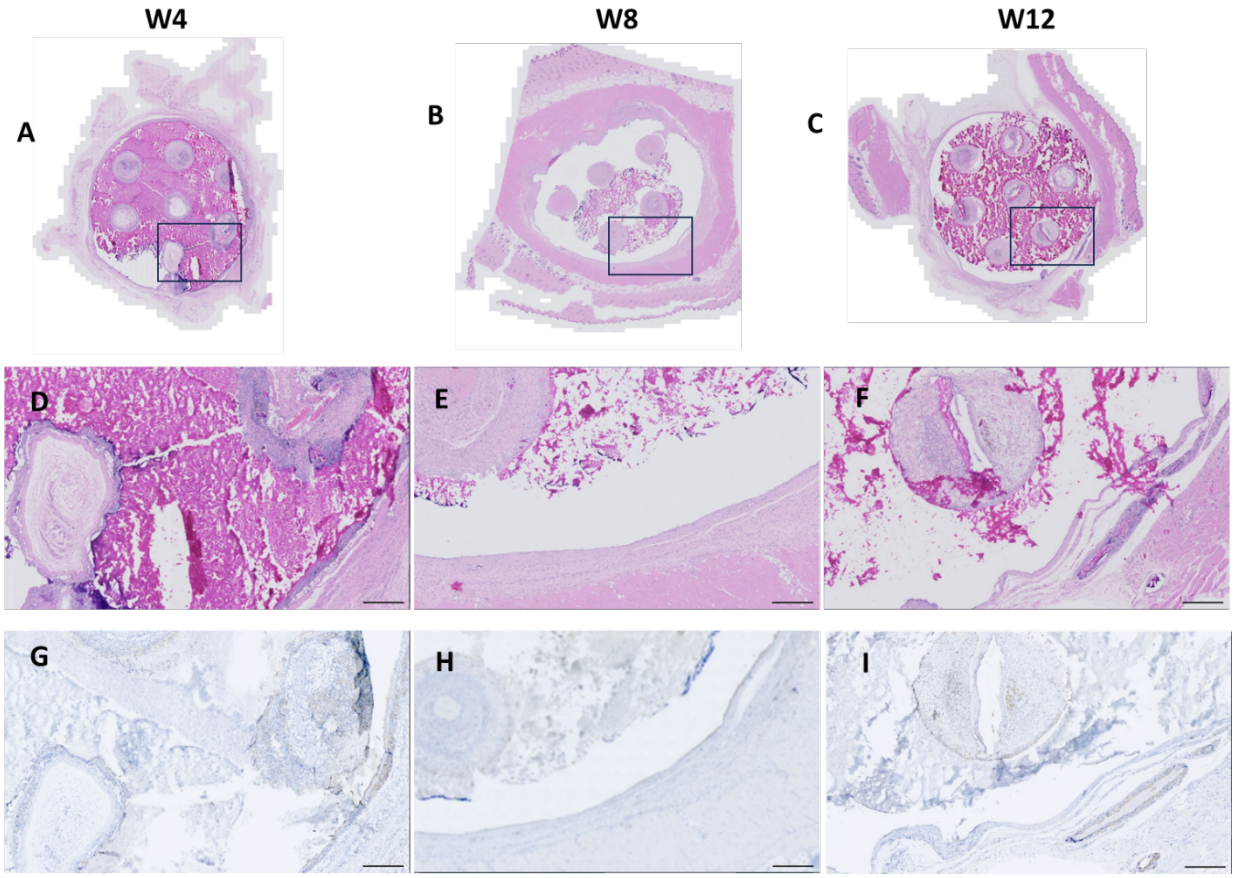

Figure 25: Biocompatibility and Cell Infiltration of the PEDGA+ BY-2 Scaffolds Implants.

This figure presents axial sections of representative 3D-printed cellulose-based scaffolds stained with H&E and anti-CD45 staining. These images illustrate the lack of foreign body reaction at 4 weeks (A) and at 8 weeks (B), followed by assimilation of the cellulose scaffold into the native rat tissue at 12 weeks (C). Higher magnification regions of interest are shown in Image D-F, as indicated in the inset in Image A-C, providing detailed observation of cell population dynamics during biomaterial assimilation processes. The immune response observed with H&E staining is further confirmed using anti-CD45 antibody, a known marker of leukocytes in Image G-I. Scale bars: 500 µm.

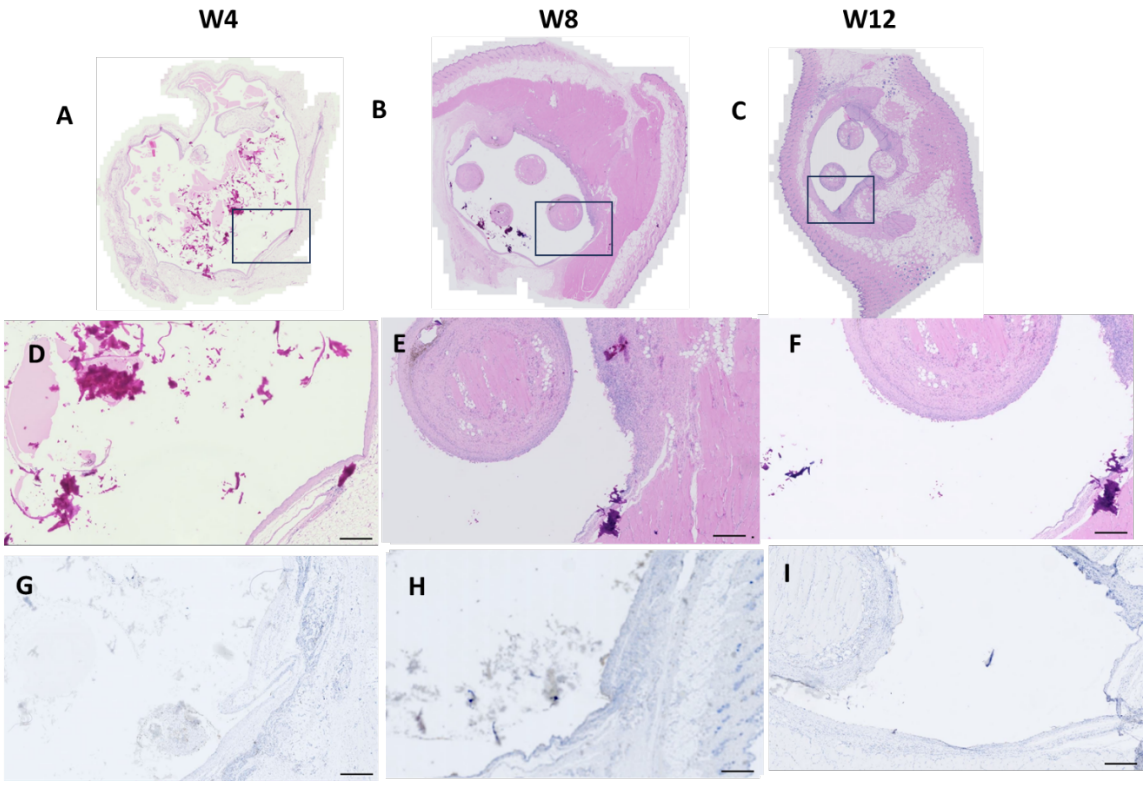

Figure 26: Biocompatibility and Cell Infiltration of the PEDGA Scaffolds Implants.

This figure presents axial sections of representative 3D-printed scaffolds stained with H&E and anti-CD45, highlighting the biocompatibility and cell infiltration of the PEGDA scaffold without decellularized BY-2 plant cells, in contrast to Figure 5. These images illustrate the lack of foreign body reaction at 4 weeks (A) and at 8 weeks (B), followed by assimilation of the scaffold into the native rat tissue at 12 weeks (C). The scaffold integrity decreases over time, with noticeable degradation from week 4 to week 12. Higher magnification regions of interest in Image D-F, as indicated in the inset in Image A-C, provide detailed observation of cell population dynamics during biomaterial assimilation processes. The immune response observed with H&E staining is further confirmed using anti-CD45 antibody, a known marker of leukocytes in Image G-I. Scale bars: D-I = 100 μm.

4.3.5 Vascularization of PEGDA+ BY-2 Scaffold.

Figure 27 illustrates the vascularization associated with the PEGDA + BY-2 cellulose scaffold after 12 weeks of implantation. The presence of blood vessels in the surrounding tissues and around the scaffold, as observed in **Figure 27A**, indicates that the scaffold supports vascular integration with the host tissue. The confirmation of angiogenesis within the cellulose scaffold is demonstrated through multiple vessel cross-sections in the H&E staining (**Figure 27B**) and Masson's Trichrome staining micrographs (**Figure 27C**).

Furthermore, the anti-CD31 staining in **Figure 27D** highlights the presence of endothelial cells within the scaffold, confirming the angiogenesis process. CD31, also known as platelet endothelial cell adhesion molecule (PECAM-1), is a marker specific to endothelial cells that line blood vessels[229,230]. Endothelial cells play an important role in forming the inner lining of blood vessels and are essential for the development of new blood vessels[251]. The brown staining indicates these cells, providing clear evidence of new blood vessel formation within the scaffold. The endothelial cell activity is important for establishing functional vascular networks within engineered tissues, ensuring adequate nutrient and oxygen supply for cell survival and growth[252]. Notably, most of the vascularization occurs within the porous structure of the 3D-printed scaffold, suggesting that the designed porosity significantly enhances blood vessel infiltration and integration.

This robust vascularization within the porous regions underscores the scaffold's potential for supporting tissue regeneration and healing, as the presence of blood vessels is critical for nutrient delivery and waste removal in regenerating tissues. The data suggests that the 3D-printed PEGDA + BY-2 scaffold's design effectively promotes angiogenesis, making it a promising candidate for regenerative medicine applications.

In comparison, **Figures 27E-H** illustrate the same staining techniques applied to the PEGDA scaffold alone. **Figure 27E** shows the surrounding tissues and the PEGDA scaffold on the day of euthanasia. **Figures 27F-H** use H&E, MT, and anti-CD31 staining, respectively, to assess vascularization within the PEGDA scaffold. The comparison reveals a tendency for fewer blood vessels in the PEGDA scaffold compared to the PEGDA + BY-2 scaffold, indicating less vascular integration and angiogenesis. This comparison underscores the importance of the BY-2 cells in enhancing the scaffold's vascularization capabilities, further highlighting the superiority of the PEGDA + BY-2 scaffold in supporting tissue regeneration.

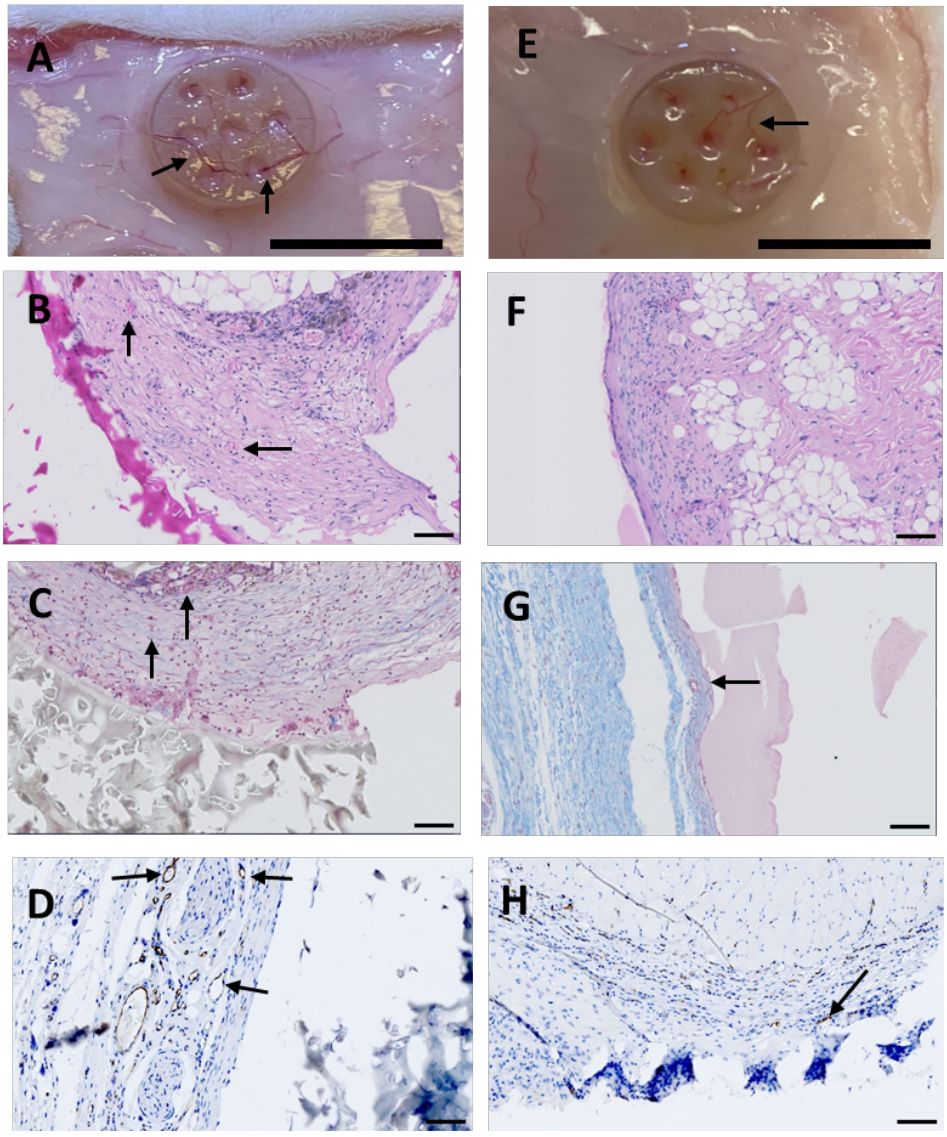

Figure 27: Vascularization of PEGDA + BY-2 scaffold and PEGDA scaffold.

The vascularization of PEGDA + BY-2 scaffolds in **Images A-D** and PEGDA scaffolds in **Images E-H** was assessed 12 weeks post-implantation. **Image A** shows blood vessels around the PEGDA + BY-2 scaffold at euthanasia**. Images B** and **C** confirm angiogenesis within the scaffold via H&E and Masson's Trichrome staining, respectively. **Image D** uses anti-CD31 staining to identify endothelial cells, confirming vascularization. **Images E-H** illustrate the same staining techniques for the PEGDA scaffold, showing fewer blood vessels compared to the PEGDA + BY-2 scaffold. Scale bars: A and E = 1 cm, B-D and F-H = 100μm. Black arrows indicate blood vessels.

4.3.6 Extracellular Matrix Deposition in the Scaffolds

The most abundant protein in the body is collagen[253]. The role of collagen in wound healing is to attract fibroblasts and encourage the deposition of new collagen to the wound bed[254–256]. Collagen dressing technology helps stimulate new tissue growth while encouraging autolytic debridement, angiogenesis, and reepithelialization. Chronic wounds develop excessive matrix metalloproteinases (MMPs) that interfere with the normal wound healing process. Collagen dressings bind and inactivate excessive MMPs found within the extracellular matrix (ECM)[257].

The presence of collagen-processing fibroblast cells led us to question if the cellulose scaffold was acting as a substrate for the deposition of a new extracellular matrix. This was determined using Masson's Trichrome (MT) staining of fixed scaffold slides at each time point following implantation (**Figures 28** and **29**).

Figure 28 illustrates the extracellular matrix deposition in the PEGDA+BY-2 scaffold. At 4 weeks, collagen deposits are scarce but become more prominent by 8 and 12 weeks, coinciding with the presence of collagen-processing fibroblast cells. There is no observable difference in collagen deposition between week 8 and week 12, indicating a plateau in the deposition process (**Figures 28E, 28F, 28H**, and **28I**). The pathologist noted fine collagen plugs in the implant and at the periphery suggesting a well-integrated collagen matrix within the scaffold.

Figure 29 shows the extracellular matrix deposition in the PEGDA scaffold. Similar to the PEGDA+BY-2 scaffold, collagen deposits are scarce at 4 weeks but become more prominent by 8 and 12 weeks. The presence of a collagen network inside the scaffold cavities, coinciding with the presence of fibroblasts, suggests the scaffold's effectiveness in supporting extracellular matrix deposition (**Figures 29E, 29F, 29H**, and **29I**). The pathologist observed focally dense collagen at the periphery of the PEGDA scaffold, which may indicate a localized fibrotic response.

Figure 29, depicting the PEGDA scaffold, shows more intense collagen deposition compared to **Figure 28**, which represents the PEGDA+BY-2 scaffold. This is evidenced by the darker blue staining in Masson's Trichrome, indicating a higher density of collagen fibres and suggesting greater encapsulation. After 8 weeks, the PEGDA scaffold exhibits significant collagen deposition, which remains consistent and similarly dense at 12 weeks post-implantation. This suggests that the scaffold reaches a plateau in collagen infiltration by this time point. The denser collagen network around the PEGDA scaffold points to a more significant fibrotic response, likely due to its scaffold composition and architecture[258].

The observed collagen is primarily deposited through the porous structure of both types of scaffolds, emphasizing the importance of 3D printing technology in scaffold fabrication. The bioprinting process allows for precise control over the scaffold architecture, including pore size and distribution, which facilitates cellular infiltration and subsequent extracellular matrix deposition. This underscores the potential of 3D bioprinted scaffolds in regenerative medicine, as they provide a tailored environment that enhances tissue regeneration. By customizing scaffold porosity, it is possible to optimize collagen infiltration, thereby promoting more effective collagen deposition and improving over tissue repair outcomes.

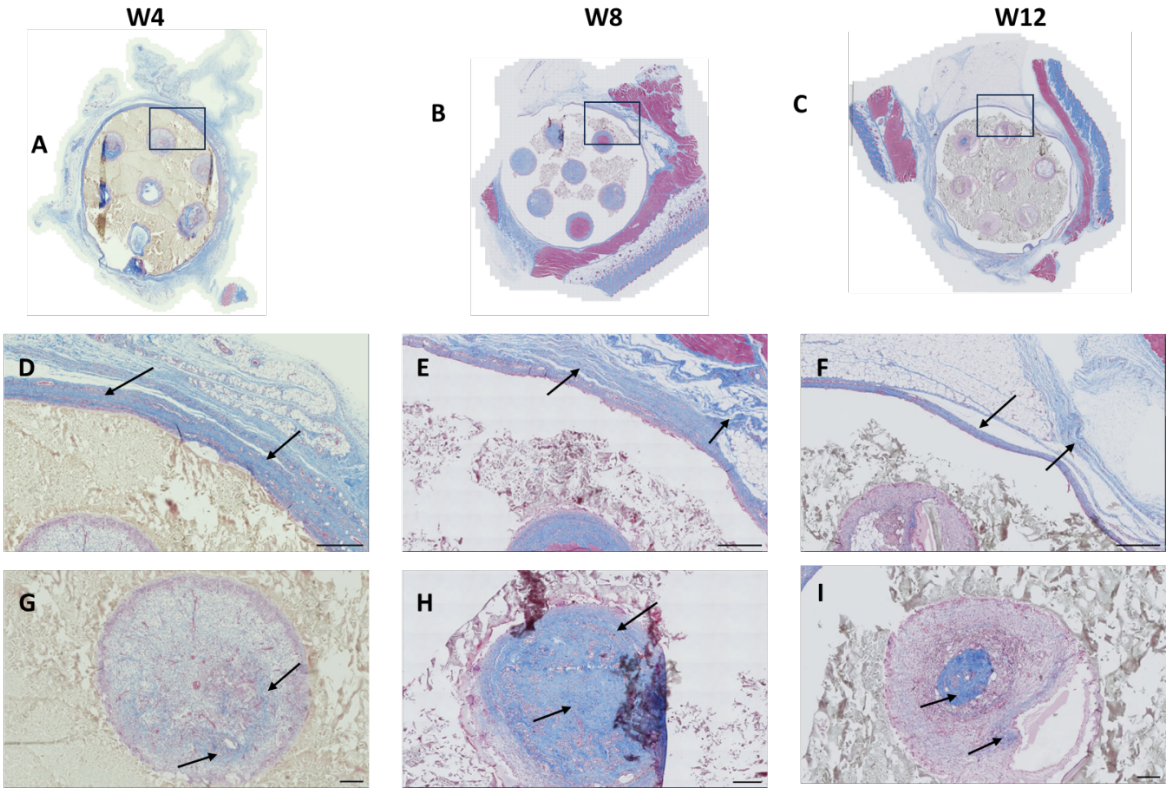

Figure 28: Extracellular Matrix Deposition in the PEGDA+ BY-2 Scaffold.

Cross sections of representative PEGDA+BY-2 scaffolds stained with MT are shown in **Image A-C**. **Image A** shows the full scaffold post-implantation. **Image D** provides a closer view, and **Image G** highlights the porous structure where more collagen is observed. By 8 and 12 weeks (**Images E, F, H, I**), a collagen network is clearly visible inside the cavities, coinciding with the presence of activated fibroblasts. Scale bars: D-F = 500µm and G-I = 200µm. Black arrows indicate collagen.

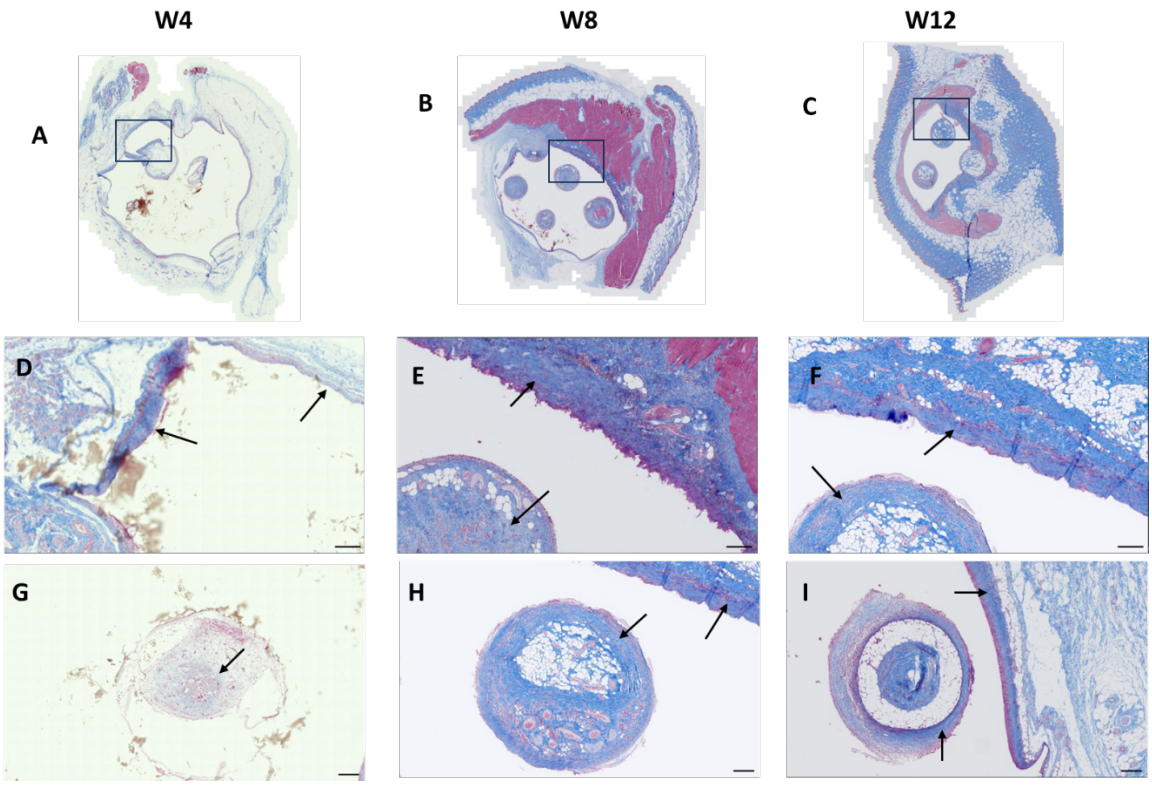

Figure 29: Extracellular Matrix Deposition in the PEGDA Scaffold.

Cross sections of representative PEGDA scaffolds stained with Masson's Trichrome are shown in **Image A-C**. **Image A** displays the full scaffold post-implantation. **Image D** provides a closer view, while I**mage G** focuses on the porous structure of the scaffold where collagen is observed. By 8 and 12 weeks (**E, F, H, I**), a collagen network is clearly visible inside the cavities, coinciding with the presence of activated fibroblasts. Scale bars: D-I = 200µm. Black arrows indicate collagen.

4.4 Conclusion

The comparison of PEGDA and PEGDA + BY-2 scaffolds highlight the potential benefits and challenges of incorporating decellularized BY-2 plant cells into 3D-printed scaffolds. At the 12-week time point, PEGDA + BY-2 scaffolds demonstrated enhanced structural integrity and cell infiltration compared to PEGDA-only scaffolds. H&E staining revealed the presence of calcific material and fibrosis in both scaffold types, indicating the body's attempt to wall off and reject the scaffold. Anti-CD45 staining showed minimal immune reactions and good tissue integration for both scaffold types over the different time points. Additionally, anti-CD31 staining confirmed improved vascularization in the PEGDA + BY-2 scaffolds.

The mechanical strength of the PEGDA + BY-2 scaffolds, attributed to their hydrogel-like structure, maintained their shape and porosity over time, aligning with Young's modulus findings in Chapter 2. The differences in collagen deposition between PEGDA and PEGDA + BY-2 scaffolds, with PEGDA showing more intense and organized collagen networks, emphasize the importance of 3D bioprinting in scaffold design for effective tissue regeneration and extracellular matrix deposition.

Scaffold biocompatibility was further supported by the results of the H&E staining, which showed some cell infiltration and a decrease in foreign body reaction at each time point. The persistence of BY-2 cells within the scaffold, before and after implantation, was confirmed by MT staining, highlighting their structural stability. However, H&E staining also revealed the presence of calcific material and fibrosis, which are hallmarks of the body's attempt to wall off and reject the scaffold.

The presence of calcific material indicates the deposition of calcium salts within the tissue, suggesting ongoing mineralization processes that are not indicative of bone tissue engineering but rather the body's rejection response. While the PEGDA + BY-2 scaffolds have improved

mechanical properties and show potential for tissue engineering applications, the occurrence of calcification and fibrosis highlights the need for further research to address these biocompatibility challenges.

Overall, while the incorporation of decellularized BY-2 plant cells into PEGDA scaffolds enhances mechanical properties and cell integration, the occurrence of calcification and fibrosis suggests that the scaffold is not without challenges. Despite these drawbacks, the PEGDA + BY-2 scaffolds show potential for tissue engineering applications due to their improved structural stability and partial biocompatibility. Addressing the observed negative responses through further optimization will be crucial for fully realizing the potential of these scaffolds in tissue engineering.

Chapter 5

Conclusion

5.1 General Conclusion

This study aimed to assess the integrity, effectiveness and biocompatibility of 3D printed hydrogel scaffold. The particularity of this model lies in its formulation, which includes PEGDA mixed with the remaining structural components of decellularized tobacco plant cells, aiming at enhancing the properties mentioned above. Throughout the chapters, we investigated various aspects of these scaffolds, from their structural properties to their ability to support cell growth and extracellular matrix deposition, with scaffolds formulated of PEGDA only as a control.

5.1.1 Summary of Findings

Chapter 1 provided a general introduction to the importance of tissue engineering, emphasizing the necessity of 3D culture systems for more accurate tissue models. It introduced the concept of scaffolds and the use of the Lumen-X 3D bioprinter, which enables precise control over scaffold architecture, including pore size and distribution. The chapter also discussed the process of decellularizing plant materials, specifically BY-2 cells, to create biocompatible scaffolds that support tissue regeneration.

Chapter 2 focused on the fabrication and characterization of the scaffolds. It was established that the addition of decellularized BY-2 plant cells to PEGDA improved the mechanical properties of the scaffolds, as evidenced by enhanced Young's modulus measurements. The structural integrity of the PEGDA+BY-2 scaffolds was maintained throughout the study, which is crucial for their application in tissue engineering as it ensures the scaffolds can provide stable and consistent support for cellular growth and tissue development.

Chapter 3 explored the *in vitro* biocompatibility of the scaffolds, using NIH 3T3 cells. The results demonstrated that both scaffold types, PEGDA and PEGDA+BY-2, supported cell adhesion and proliferation. However, the PEGDA+BY-2 scaffolds showed superior performance in promoting cell growth and maintaining structural stability, which ensures that the scaffold can withstand the mechanical forces in the body and support the formation of new tissues. The presence of active fibroblasts indicated good biocompatibility.

Chapter 4 extended the investigation to *in vivo* experiments, where the scaffolds were subcutaneously implanted in rats. Over a 12-week period, the PEGDA+BY-2 scaffolds exhibited slightly better cell infiltration and enhanced vascularization compared to PEGDA scaffolds. Histological analysis revealed collagen deposition at the periphery in both scaffold types, with the PEGDA scaffold showing more intense and organized collagen networks. The observed collagen deposition through the porous structure of both scaffold types highlights the potential of the scaffold design. The precise control over scaffold architecture facilitated effective cellular infiltration and extracellular matrix deposition, which is advantageous for tissue regeneration. While we cannot definitively attribute the facilitation of these processes solely to 3D printing, the scaffold design achieved through this technique provides a favourable environment for cellular activities. Importantly, neither scaffold type elicited a significant immune response, confirming their biocompatibility. However, some instances of calcification and fibrosis, which are hallmarks of rejection, were observed in both scaffold types. Despite these occurrences, the overall biocompatibility of the scaffolds remains promising for future tissue engineering applications.

5.1.2 Comparative Analysis

When comparing the PEGDA and PEGDA+BY-2 scaffolds to other studies in the field, several key observations can be made. Traditional PEGDA scaffolds have been extensively studied for their biocompatibility, mechanical properties, and ability to support cell growth[83,86,233,242–244,259].

For instance, PEGDA scaffolds mixed with other materials, such as chitosan or cellulose nanofibers, have demonstrated tunable mechanical properties and high biocompatibility, which aligns with our findings on the PEGDA scaffold's performance[260–262]. However, the addition of decellularized BY-2 cells appears to confer additional benefits.

Studies on scaffolds incorporating plant-derived components, such as decellularized BY-2 cells, are less common but have shown promise in enhancing scaffold properties. The incorporation of BY-2 cells into PEGDA scaffolds in our study improved the mechanical properties, as evidenced by the enhanced Young's modulus. This finding is supported by similar studies that have shown improved mechanical strength and stability when plant-derived components are used in scaffold formulations.

Furthermore, the PEGDA+BY-2 scaffolds exhibited superior cell proliferation and biocompatibility compared to PEGDA-only scaffolds. This suggests that the inclusion of decellularized plant cells provides a more conducive environment for cellular activities, possibly due to the natural micros porous components present in the plant cells. In contrast, PEGDA scaffolds, while effective, may not provide the same level of biological cues needed for optimal cell growth and tissue regeneration.

The enhanced vascularization observed in the PEGDA+BY-2 scaffolds during the *in vivo* experiments is another significant advantage. This aligns with studies that have highlighted the importance of vascularization in tissue engineering, as it ensures adequate nutrient and oxygen supply to the growing tissue. While PEGDA scaffolds alone have shown potential for vascularization, the addition of decellularized BY-2 cells seems to enhance this process, making the PEGDA+BY-2 scaffolds more effective for tissue regeneration applications.

In terms of immune response, both scaffold types did not elicit significant immune reactions, which is a crucial aspect of biocompatibility. This finding is consistent with other studies on PEGDA scaffolds, which have generally shown low immunogenicity. The inclusion of decellularized plant cells did not adversely affect this aspect, further supporting the potential of PEGDA+BY-2 scaffolds for clinical applications.

5.2 Future Work

The observed collagen deposition through the porous structure of both scaffold types underscored the benefits of 3D printing technology. The precise control over scaffold architecture facilitated effective cellular infiltration and extracellular matrix deposition, which are essential for tissue regeneration[73,76,89,221,263,264].

While this study has demonstrated the potential of PEGDA+BY-2 scaffolds in tissue engineering, several avenues for future research remain. Extending the duration of *in vivo* studies beyond 12 weeks would provide more comprehensive data on the long-term biocompatibility and functionality of the scaffolds[265,266]. This could help in understanding the scaffold's behaviour over extended periods and its integration with host tissues. Given the structural integrity and biocompatibility of the PEGDA+BY-2 scaffolds, future research could explore their application in bone tissue engineering. The mechanical properties of these scaffolds make them suitable candidates for supporting bone regeneration[263]. Investigating their performance in bone defect models would be a logical next step. Further studies on the molecular mechanisms underlying collagen deposition and scaffold integration would provide deeper insights into the scaffold's interaction with host tissues[267,268]. This could involve examining the gene expression profiles of cells interacting with the scaffolds to identify key regulatory pathways[269–271]. Additionally, future

in vivo studies could include more complex animal models, such as larger mammals like rabbits or pigs, which provide anatomical and physiological characteristics more similar to humans[272,273]. These models would offer a more accurate representation of human tissue environments, particularly in terms of immune response, vascularization, and tissue regeneration. Such models could help assess scaffold performance under various physiological conditions, including different tissue types and mechanical forces, ultimately providing a more comprehensive evaluation of the scaffold's biocompatibility, durability, and effectiveness for potential clinical applications[274,275]. 3D bioprinting allows for the customization of scaffold properties. Future work could involve optimizing pore size, shape, and distribution to enhance specific tissue regeneration outcomes. Additionally, incorporating bioactive molecules or growth factors into the scaffolds could further improve their regenerative potential[276–279]. In conclusion, the PEGDA+BY-2 scaffolds have shown promising results in supporting regeneration. With further research and optimization, these scaffolds could be developed into effective tools for regenerative medicine, potentially extending their application to bone tissue engineering and beyond.

Reference

1. Mao, A. S. & Mooney, D. J. Regenerative medicine: Current therapies and future directions. *Proceedings of the National Academy of Sciences* **112**, 14452–14459 (2015).
2. Padmalayam, I. & Suto, M. J. 3D Cell Cultures. in 367–378 (2012). doi:10.1016/B978-0-12-396492-2.00024-2.
3. Fontoura, J. C. *et al.* Comparison of 2D and 3D cell culture models for cell growth, gene expression and drug resistance. *Materials Science and Engineering C* **107**, (2020).
4. Jeon, J., Lee, M. S. & Yang, H. S. Differentiated osteoblasts derived decellularized extracellular matrix to promote osteogenic differentiation. *Biomater Res* **22**, (2018).
5. Assunção, M. *et al.* Cell-Derived Extracellular Matrix for Tissue Engineering and Regenerative Medicine. *Frontiers in Bioengineering and Biotechnology* vol. 8 Preprint at https://doi.org/10.3389/fbioe.2020.602009 (2020).
6. Khan, H. M. *et al.* Smart biomaterials and their potential applications in tissue engineering. *Journal of Materials Chemistry B* vol. 10 6859–6895 Preprint at https://doi.org/10.1039/d2tb01106a (2022).
7. Janani, G., Pillai, M. M., Selvakumar, R., Bhattacharyya, A. & Sabarinath, C. An *in vitro* 3D model using collagen coated gelatin nanofibers for studying breast cancer metastasis. *Biofabrication* **9**, 015016 (2017).
8. Joyce, K., Fabra, G. T., Bozkurt, Y. & Pandit, A. Bioactive potential of natural biomaterials: identification, retention and assessment of biological properties. *Signal Transduct Target Ther* **6**, 122 (2021).
9. Ghasemi-Mobarakeh, L., Kolahreez, D., Ramakrishna, S. & Williams, D. Key terminology in biomaterials and biocompatibility. *Curr Opin Biomed Eng* **10**, 45–50 (2019).
10. Song, R. *et al.* Current development of biodegradable polymeric materials for biomedical applications. *Drug Des Devel Ther* **Volume 12**, 3117–3145 (2018).
11. Langer, R. & Peppas, N. A. Advances in biomaterials, drug delivery, and bionanotechnology. *AIChE Journal* **49**, 2990–3006 (2003).
12. Tran, K. T. M. & Nguyen, T. D. Lithography-based methods to manufacture biomaterials at small scales. *Journal of Science: Advanced Materials and Devices* **2**, 1–14 (2017).
13. Müller, F. J. & Fenton, O. S. Additive Manufacturing Approaches toward the Fabrication of Biomaterials. *Adv Mater Interfaces* **9**, (2022).

14. Anseth, K. S. & Burdick, J. A. New Directions in Photopolymerizable Biomaterials. *MRS Bull* **27**, 130–136 (2002).
15. Han, F. *et al.* Tissue Engineering and Regenerative Medicine: Achievements, Future, and Sustainability in Asia. *Frontiers in Bioengineering and Biotechnology* vol. 8 Preprint at https://doi.org/10.3389/fbioe.2020.00083 (2020).
16. Chen, X. *et al.* Functional Multichannel Poly(Propylene Fumarate)-Collagen Scaffold with Collagen-Binding Neurotrophic Factor 3 Promotes Neural Regeneration After Transected Spinal Cord Injury. *Adv Healthc Mater* **7**, 1800315 (2018).
17. Boccafoschi, F., Habermehl, J., Vesentini, S. & Mantovani, D. Biological performances of collagen-based scaffolds for vascular tissue engineering. *Biomaterials* **26**, 7410–7417 (2005).
18. Fauzi, M. B., Lokanathan, Y., Aminuddin, B. S., Ruszymah, B. H. I. & Chowdhury, S. R. Ovine tendon collagen: Extraction, characterisation and fabrication of thin films for tissue engineering applications. *Materials Science and Engineering: C* **68**, 163–171 (2016).
19. Farshidfar, N., Iravani, S. & Varma, R. S. Alginate-Based Biomaterials in Tissue Engineering and Regenerative Medicine. *Mar Drugs* **21**, 189 (2023).
20. Sun, J. & Tan, H. Alginate-Based Biomaterials for Regenerative Medicine Applications. *Materials* **6**, 1285–1309 (2013).
21. Nayak, A. K., Mohanta, B. C., Hasnain, M. S., Hoda, M. N. & Tripathi, G. Alginate-based scaffolds for drug delivery in tissue engineering. in *Alginates in Drug Delivery* 359–386 (Elsevier, 2020). doi:10.1016/B978-0-12-817640-5.00014-5.
22. Hernández-González, A. C., Téllez-Jurado, L. & Rodríguez-Lorenzo, L. M. Alginate hydrogels for bone tissue engineering, from injectables to bioprinting: A review. *Carbohydr Polym* **229**, 115514 (2020).
23. Echave, M. C., Burgo, L. S., Pedraz, J. L. & Orive, G. Gelatin as Biomaterial for Tissue Engineering. *Curr Pharm Des* **23**, (2017).
24. Lukin, I. *et al.* Progress in Gelatin as Biomaterial for Tissue Engineering. *Pharmaceutics* **14**, 1177 (2022).
25. Zheng, H. & Zuo, B. Functional silk fibroin hydrogels: preparation, properties and applications. *Journal of Materials Chemistry B* vol. 9 1238–1258 Preprint at https://doi.org/10.1039/d0tb02099k (2021).
26. Islam, M. M., Shahruzzaman, M., Biswas, S., Nurus Sakib, M. & Rashid, T. U. Chitosan based bioactive materials in tissue engineering applications-A review. *Bioactive Materials* vol. 5 164–183 Preprint at https://doi.org/10.1016/j.bioactmat.2020.01.012 (2020).

27. Prasathkumar, M. & Sadhasivam, S. Chitosan/Hyaluronic acid/Alginate and an assorted polymers loaded with honey, plant, and marine compounds for progressive wound healing—Know-how. *Int J Biol Macromol* **186**, 656–685 (2021).
28. Shukla, S. K., Mishra, A. K., Arotiba, O. A. & Mamba, B. B. Chitosan-based nanomaterials: A state-of-the-art review. *Int J Biol Macromol* **59**, 46–58 (2013).
29. Pellá, M. C. G. *et al.* Chitosan-based hydrogels: From preparation to biomedical applications. *Carbohydr Polym* **196**, 233–245 (2018).
30. Khaing, Z. Z. & Schmidt, C. E. Advances in natural biomaterials for nerve tissue repair. *Neurosci Lett* **519**, 103–114 (2012).
31. Trache, D., Hussin, M. H., Haafiz, M. K. M. & Thakur, V. K. Recent progress in cellulose nanocrystals: sources and production. *Nanoscale* **9**, 1763–1786 (2017).
32. Hickey, R. J. & Pelling, A. E. Cellulose Biomaterials for Tissue Engineering. *Front Bioeng Biotechnol* **7**, (2019).
33. Castro, C. *et al.* Bacterial cellulose produced by a new acid-resistant strain of Gluconacetobacter genus. *Carbohydr Polym* **89**, 1033–1037 (2012).
34. Huang, Y. *et al.* Recent advances in bacterial cellulose. *Cellulose* **21**, 1–30 (2014).
35. Rahman, Md. S. *et al.* Recent Developments of Carboxymethyl Cellulose. *Polymers (Basel)* **13**, 1345 (2021).
36. Chen, H.-H., Chen, L.-C., Huang, H.-C. & Lin, S.-B. In situ modification of bacterial cellulose nanostructure by adding CMC during the growth of Gluconacetobacter xylinus. *Cellulose* **18**, 1573–1583 (2011).
37. Reddy, M. S. B., Ponnamma, D., Choudhary, R. & Sadasivuni, K. K. A comparative review of natural and synthetic biopolymer composite scaffolds. *Polymers* vol. 13 Preprint at https://doi.org/10.3390/polym13071105 (2021).
38. Sonam, S., Chaudhary, H., Arora, V., Kholi, K. & Kumar, V. Effect of physicochemical properties of biodegradable polymers on nano drug delivery. *Polymer Reviews* **53**, 546–567 (2013).
39. Elmowafy, E. M., Tiboni, M. & Soliman, M. E. Biocompatibility, biodegradation and biomedical applications of poly(lactic acid)/poly(lactic-co-glycolic acid) micro and nanoparticles. *Journal of Pharmaceutical Investigation* vol. 49 347–380 Preprint at https://doi.org/10.1007/s40005-019-00439-x (2019).
40. Kiss, É., Kutnyánszky, E. & Bertóti, I. Modification of Poly(lactic/glycolic acid) Surface by Chemical Attachment of Poly(ethylene glycol). *Langmuir* **26**, 1440–1444 (2010).

41. Makadia, H. K. & Siegel, S. J. Poly Lactic-co-Glycolic Acid (PLGA) as Biodegradable Controlled Drug Delivery Carrier. *Polymers (Basel)* **3**, 1377–1397 (2011).
42. Zarrintaj, P., Saeb, M. R., Jafari, S. H. & Mozafari, M. Application of compatibilized polymer blends in biomedical fields. in *Compatibilization of Polymer Blends* 511–537 (Elsevier, 2020). doi:10.1016/B978-0-12-816006-0.00018-9.
43. Modulevsky, D. J., Lefebvre, C., Haase, K., Al-Rekabi, Z. & Pelling, A. E. Apple derived cellulose scaffolds for 3D mammalian cell culture. *PLoS One* **9**, (2014).
44. Adamski, M. *et al.* Two Methods for Decellularization of Plant Tissues for Tissue Engineering Applications. *Journal of Visualized Experiments* (2018) doi:10.3791/57586.
45. Abdul Khalil, H. P. S. *et al.* A Review on Plant Cellulose Nanofibre-Based Aerogels for Biomedical Applications. *Polymers (Basel)* **12**, 1759 (2020).
46. Salimi, S., Sotudeh-Gharebagh, R., Zarghami, R., Chan, S. Y. & Yuen, K. H. Production of Nanocellulose and Its Applications in Drug Delivery: A Critical Review. *ACS Sustainable Chemistry and Engineering* vol. 7 15800–15827 Preprint at https://doi.org/10.1021/acssuschemeng.9b02744 (2019).
47. Huerta, R. R., Silva, E. K., Ekaette, I., El-Bialy, T. & Saldaña, M. D. A. High-intensity ultrasound-assisted formation of cellulose nanofiber scaffold with low and high lignin content and their cytocompatibility with gingival fibroblast cells. *Ultrason Sonochem* **64**, (2020).
48. Zhu, Y. *et al.* Current Advances in the Development of Decellularized Plant Extracellular Matrix. *Front Bioeng Biotechnol* **9**, (2021).
49. Liu, J. *et al.* Hemicellulose-reinforced nanocellulose hydrogels for wound healing application. *Cellulose* **23**, 3129–3143 (2016).
50. Rongpipi, S., Ye, D., Gomez, E. D. & Gomez, E. W. Progress and Opportunities in the Characterization of Cellulose – An Important Regulator of Cell Wall Growth and Mechanics. *Front Plant Sci* **9**, (2019).
51. Zhang, X. *et al.* Three-Dimensional Printed Cell Culture Model Based on Spherical Colloidal Lignin Particles and Cellulose Nanofibril-Alginate Hydrogel. *Biomacromolecules* **21**, 1875–1885 (2020).
52. Coimbra, P. *et al.* Preparation and chemical and biological characterization of a pectin/chitosan polyelectrolyte complex scaffold for possible bone tissue engineering applications. *Int J Biol Macromol* **48**, 112–118 (2011).

53. Hamzah, M. S. A. *et al.* Fabrication and evaluation of polylactic acid/pectin composite scaffold via freeze extraction for tissue engineering. *Journal of Polymer Engineering* **40**, 421–431 (2020).
54. Modulevsky, D. J., Cuerrier, C. M. & Pelling, A. E. Biocompatibility of Subcutaneously Implanted Plant-Derived Cellulose Biomaterials. *PLoS One* **11**, (2016).
55. Phan, N. V., Wright, T., Rahman, M. M., Xu, J. & Coburn, J. M. In Vitro Biocompatibility of Decellularized Cultured Plant Cell-Derived Matrices. *ACS Biomater Sci Eng* **6**, 822–832 (2020).
56. Hickey, R. J., Modulevsky, D. J., Cuerrier, C. M. & Pelling, A. E. Customizing the Shape and Microenvironment Biochemistry of Biocompatible Macroscopic Plant-Derived Cellulose Scaffolds. *ACS Biomater Sci Eng* **4**, 3726–3736 (2018).
57. Hickey, R. J., Leblanc Latour, M., Harden, J. L. & Pelling, A. E. Designer Scaffolds for Interfacial Bioengineering. *Adv Eng Mater* (2022) doi:10.1002/adem.202201415.
58. Holmes, J. T. *et al.* Homemade bread: Repurposing an ancient technology for in vitro tissue engineering. *Biomaterials* **280**, (2022).
59. Mariani, E., Lisignoli, G., Borzì, R. M. & Pulsatelli, L. Biomaterials: Foreign bodies or tuners for the immune response? *International Journal of Molecular Sciences* vol. 20 Preprint at https://doi.org/10.3390/ijms20030636 (2019).
60. Ding, S.-Y. *et al.* How Does Plant Cell Wall Nanoscale Architecture Correlate with Enzymatic Digestibility? *Science (1979)* **338**, 1055–1060 (2012).
61. Zhang, T., Tang, H., Vavylonis, D. & Cosgrove, D. J. Disentangling loosening from softening: insights into primary cell wall structure. *The Plant Journal* **100**, 1101–1117 (2019).
62. Burgert, I. & Fratzl, P. Plants control the properties and actuation of their organs through the orientation of cellulose fibrils in their cell walls. *Integr Comp Biol* **49**, 69–79 (2009).
63. Zhang, T., Zheng, Y. & Cosgrove, D. J. Spatial organization of cellulose microfibrils and matrix polysaccharides in primary plant cell walls as imaged by multichannel atomic force microscopy. *The Plant Journal* **85**, 179–192 (2016).
64. Wang, T., Park, Y. B., Cosgrove, D. J. & Hong, M. Cellulose-Pectin Spatial Contacts Are Inherent to Never-Dried Arabidopsis Primary Cell Walls: Evidence from Solid-State Nuclear Magnetic Resonance. *Plant Physiol* **168**, 871–884 (2015).
65. Abidi, S. M. S., Dar, A. I. & Acharya, A. Plant-Based Polymeric Nanomaterials for Biomedical Applications. in *Nanomaterial - Based Biomedical Applications in Molecular*

Imaging, Diagnostics and Therapy 129–158 (Springer Singapore, Singapore, 2020). doi:10.1007/978-981-15-4280-0_7.

66. REMES, A. & WILLIAMS, D. Immune response in biocompatibility. *Biomaterials* **13**, 731–743 (1992).
67. Moire, L., Rezzonico, E. & Poirier, Y. Synthesis of novel biomaterials in plants. *J Plant Physiol* **160**, 831–839 (2003).
68. Bonferoni, M. C. *et al.* Biomaterials for Soft Tissue Repair and Regeneration: A Focus on Italian Research in the Field. *Pharmaceutics* **13**, 1341 (2021).
69. Tonda-Turo, C. *et al.* Photocurable chitosan as bioink for cellularized therapies towards personalized scaffold architecture. *Bioprinting* **18**, e00082 (2020).
70. Szymański, T. *et al.* Hyaluronic acid and multiwalled carbon nanotubes as bioink additives for cartilage tissue engineering. *Sci Rep* **13**, 646 (2023).
71. Jin, S. *et al.* Recent advances in PLGA-based biomaterials for bone tissue regeneration. *Acta Biomater* **127**, 56–79 (2021).
72. Vasanthan, J. *et al.* Role of Human Mesenchymal Stem Cells in Regenerative Therapy. *Cells* **10**, 54 (2020).
73. Chia, H. N. & Wu, B. M. Recent advances in 3D printing of biomaterials. *J Biol Eng* **9**, (2015).
74. Murphy, S. V. & Atala, A. 3D bioprinting of tissues and organs. *Nature Biotechnology* vol. 32 773–785 Preprint at https://doi.org/10.1038/nbt.2958 (2014).
75. Mobaraki, M., Ghaffari, M., Yazdanpanah, A., Luo, Y. & Mills, D. K. Bioinks and bioprinting: A focused review. *Bioprinting* **18**, e00080 (2020).
76. Wang, M. *et al.* 3D Contour Printing of Anatomically Mimetic Cartilage Grafts with Microfiber-Reinforced Double-Network Bioink. *Macromol Biosci* **22**, (2022).
77. Gao, Q., He, Y., Fu, J., Liu, A. & Ma, L. Coaxial nozzle-assisted 3D bioprinting with built-in microchannels for nutrients delivery. *Biomaterials* **61**, 203–215 (2015).
78. Muir, V. G. *et al.* Sticking Together: Injectable Granular Hydrogels with Increased Functionality via Dynamic Covalent Inter-Particle Crosslinking. *Small* **18**, (2022).
79. GhavamiNejad, A., Ashammakhi, N., Wu, X. Y. & Khademhosseini, A. Crosslinking Strategies for 3D Bioprinting of Polymeric Hydrogels. *Small* **16**, (2020).
80. Jo, S., Lee, J., Lee, H., Ryu, D. & Kim, G. The one-step fabrication of porous hASC-laden GelMa constructs using a handheld printing system. *NPJ Regen Med* **8**, 30 (2023).
81. Lee, J., Lee, H., Jin, E.-J., Ryu, D. & Kim, G. H. 3D bioprinting using a new photo-crosslinking method for muscle tissue restoration. *NPJ Regen Med* **8**, 18 (2023).

82. Parhi, R. Cross-linked hydrogel for pharmaceutical applications: A review. *Advanced Pharmaceutical Bulletin* vol. 7 515–530 Preprint at https://doi.org/10.15171/apb.2017.064 (2017).
83. Eshel-Green, T., Eliyahu, S., Avidan-Shlomovich, S. & Bianco-Peled, H. PEGDA hydrogels as a replacement for animal tissues in mucoadhesion testing. *Int J Pharm* **506**, 25–34 (2016).
84. Magalhães, L. S. S. M. *et al.* Nanocomposite Hydrogel Produced from PEGDA and Laponite for Bone Regeneration. *J Funct Biomater* **13**, (2022).
85. Cristovão, A. F. *et al.* Customized tracheal design using 3D printing of a polymer hydrogel: influence of UV laser cross-linking on mechanical properties. *3D Print Med* **5**, (2019).
86. Patil, S. S., Shinde, V. S. & Misra, R. D. K. pH and reduction dual-stimuli-responsive PEGDA/PAMAM injectable network hydrogels via aza-michael addition for anticancer drug delivery. *J Polym Sci A Polym Chem* **56**, 2080–2095 (2018).
87. Caló, E. & Khutoryanskiy, V. v. Biomedical applications of hydrogels: A review of patents and commercial products. *European Polymer Journal* vol. 65 252–267 Preprint at https://doi.org/10.1016/j.eurpolymj.2014.11.024 (2015).
88. Ahmed, E. M. Hydrogel: Preparation, characterization, and applications: A review. *Journal of Advanced Research* vol. 6 105–121 Preprint at https://doi.org/10.1016/j.jare.2013.07.006 (2015).
89. Mahendiran, B. *et al.* Recent trends in natural polysaccharide based bioinks for multiscale 3D printing in tissue regeneration: A review. *Int J Biol Macromol* **183**, 564–588 (2021).
90. Indurkar, A., Pandit, A., Jain, R. & Dandekar, P. Plant-based biomaterials in tissue engineering. *Bioprinting* **21**, e00127 (2021).
91. Nagata, T., Nemoto, Y. & Hasezawa, S. Tobacco BY-2 Cell Line as the "HeLa" Cell in the Cell Biology of Higher Plants. *Int Rev Cytol* **132**, 1–30 (1992).
92. Nagata, T. & Kumagai, F. Plant cell biology through the window of the highly synchronized tobacco BY-2 cell line. *Methods in Cell Science* **21**, 123–127 (1999).
93. Kovarik, A., Lim, K.-Y., Soucková-Skalická, K., Matyasek, R. & Leitch, A. R. *A Plant Culture (BY-2) Widely Used in Molecular and Cell Studies Is Genetically Unstable and Highly Heterogeneous ADDITIONAL KEYWORDS: Cell Biology-Cell Cycle-Evolution-Instability-Karyotype-Physiology-RDNA-TBY*. *Journal of the Linnean Society* vol. 170 https://academic.oup.com/botlinnean/article/170/3/459/2416196 (2012).

94. Srba, M., Černíková, A., Opatrný, Z. & Fischer, L. Practical guidelines for the characterization of tobacco BY-2 cell lines. *Biol Plant* **60**, 13–24 (2016).
95. Brandizzi, F., Irons, S., Kearns, A. & Hawes, C. BY-2 Cells: Culture and Transformation for Live Cell Imaging. *Curr Protoc Cell Biol* **19**, (2003).
96. Srba, M., Černíková, A., Opatrný, Z. & Fischer, L. Practical guidelines for the characterization of tobacco BY-2 cell lines. *Biol Plant* **60**, 13–24 (2016).
97. Shirtliff, V. J. & Hench, L. L. Bioactive materials for tissue engineering, regeneration and repair. *J Mater Sci* **38**, 4697–4707 (2003).
98. Liu, K., Mihaila, S. M., Rowan, A., Oosterwijk, E. & Kouwer, P. H. J. Synthetic Extracellular Matrices with Nonlinear Elasticity Regulate Cellular Organization. *Biomacromolecules* **20**, 826–834 (2019).
99. Chen, G., Ushida, T. & Tateishi, T. Scaffold Design for Tissue Engineering. *Macromol Biosci* **2**, 67–77 (2002).
100. Hutmacher, D. W., Sittinger, M. & Risbud, M. V. Scaffold-based tissue engineering: rationale for computer-aided design and solid free-form fabrication systems. *Trends Biotechnol* **22**, 354–362 (2004).
101. Ma, P. X. Scaffolds for tissue fabrication. *Materials Today* **7**, 30–40 (2004).
102. Hutmacher, D. W. Scaffolds in tissue engineering bone and cartilage. *Biomaterials* **21**, 2529–2543 (2000).
103. Drury, J. L. & Mooney, D. J. Hydrogels for tissue engineering: scaffold design variables and applications. *Biomaterials* **24**, 4337–4351 (2003).
104. Lu, H., Ying, K., Shi, Y., Liu, D. & Chen, Q. Bioprocessing by Decellularized Scaffold Biomaterials in Cultured Meat: A Review. *Bioengineering* **9**, 787 (2022).
105. Iravani, S. & Varma, R. S. Plants and plant-based polymers as scaffolds for tissue engineering. *Green Chemistry* **21**, 4839–4867 (2019).
106. Chen, F. *et al.* Natural *Flammulina velutipes* -Based Nerve Guidance Conduit as a Potential Biomaterial for Peripheral Nerve Regeneration: In Vitro and In Vivo Studies. *ACS Biomater Sci Eng* **7**, 3821–3834 (2021).
107. Shoichet, M. S. Polymer Scaffolds for Biomaterials Applications. *Macromolecules* **43**, 581–591 (2010).
108. Hasnain, A. *et al.* Plants in vitro propagation with its applications in food, pharmaceuticals and cosmetic industries; current scenario and future approaches. *Front Plant Sci* **13**, (2022).

109. Ornaghi, H. L., Monticeli, F. M. & Agnol, L. D. A Review on Polymers for Biomedical Applications on Hard and Soft Tissues and Prosthetic Limbs. *Polymers (Basel)* **15**, 4034 (2023).
110. Harris, A. F., Lacombe, J. & Zenhausern, F. The Emerging Role of Decellularized Plant-Based Scaffolds as a New Biomaterial. *Int J Mol Sci* **22**, 12347 (2021).
111. Harris, A. F. *et al.* Supercritical carbon dioxide decellularization of plant material to generate 3D biocompatible scaffolds. *Sci Rep* **11**, 3643 (2021).
112. Couvrette, L. J., Walker, K. L. A., Bui, T. V. & Pelling, A. E. Plant Cellulose as a Substrate for 3D Neural Stem Cell Culture. *Bioengineering* **10**, 1309 (2023).
113. Varhama, K., Oda, H., Shima, A. & Takeuchi, S. Decellularized Plant Leaves for 3D Cell Culturing. in *2019 IEEE 32nd International Conference on Micro Electro Mechanical Systems (MEMS)* 226–228 (IEEE, 2019). doi:10.1109/MEMSYS.2019.8870620.
114. Adamski, M. *et al.* Two Methods for Decellularization of Plant Tissues for Tissue Engineering Applications. *Journal of Visualized Experiments* (2018) doi:10.3791/57586.
115. Phan, N. V., Wright, T., Rahman, M. M., Xu, J. & Coburn, J. M. In Vitro Biocompatibility of Decellularized Cultured Plant Cell-Derived Matrices. *ACS Biomater Sci Eng* **6**, 822–832 (2020).
116. Keane, T. J., Swinehart, I. T. & Badylak, S. F. Methods of tissue decellularization used for preparation of biologic scaffolds and in vivo relevance. *Methods* **84**, 25–34 (2015).
117. James, B. D. *et al.* Palm readings: Manicaria saccifera palm fibers are biocompatible textiles with low immunogenicity. *Materials Science and Engineering: C* **108**, 110484 (2020).
118. GILBERT, T., SELLARO, T. & BADYLAK, S. Decellularization of tissues and organs. *Biomaterials* (2006) doi:10.1016/j.biomaterials.2006.02.014.
119. Gilpin, A. & Yang, Y. Decellularization Strategies for Regenerative Medicine: From Processing Techniques to Applications. *Biomed Res Int* **2017**, 1–13 (2017).
120. Schiavoni, C., Genter, J., Borovetz, H. & Kloimwieder, A. Investigating the Decellularization of Plant Tissues Using at-home Kitchen Facilities During COVID. *Journal of Student Research* **11**, (2022).
121. Bilirgen, A. C. *et al.* Plant-Based Scaffolds in Tissue Engineering. *ACS Biomater Sci Eng* **7**, 926–938 (2021).
122. Mahendiran, B. *et al.* Decellularized natural 3D cellulose scaffold derived from Borassus flabellifer (Linn.) as extracellular matrix for tissue engineering applications. *Carbohydr Polym* **272**, 118494 (2021).

123. O'Donnell, N. *et al.* Cellulose-based scaffolds for fluorescence lifetime imaging-assisted tissue engineering. *Acta Biomater* **80**, 85–96 (2018).
124. Modulevsky, D. J. *et al.* Plant Scaffolds Support Motor Recovery and Regeneration in Rat Spinal Cord Injury. doi:10.1101/2020.10.21.347807.
125. Tiedemann, Hohenberg & Kollmann. High-pressure freezing of plant cells cultured in cellulose microcapillaries. *J Microsc* **189**, 163–171 (1998).
126. Rai, R. & Nitin, N. Apple-derived 3D scaffold for improving gastrointestinal viability and in-situ growth of probiotics. *Food Research International* **168**, 112758 (2023).
127. Kafle, A. *et al.* 3D/4D Printing of Polymers: Fused Deposition Modelling (FDM), Selective Laser Sintering (SLS), and Stereolithography (SLA). *Polymers (Basel)* **13**, 3101 (2021).
128. Tomassoni, C. *et al.* 3D Printing of Microwave and Millimeter-Wave Filters: Additive Manufacturing Technologies Applied in the Development of High-Performance Filters with Novel Topologies. *IEEE Microw Mag* **21**, 24–45 (2020).
129. Kim, B. S., Das, S., Jang, J. & Cho, D.-W. Decellularized Extracellular Matrix-based Bioinks for Engineering Tissue- and Organ-specific Microenvironments. *Chem Rev* **120**, 10608–10661 (2020).
130. Kim, S., Lee, H., Choi, H., Yoo, K. Y. & Yoon, H. Investigation on photopolymerization of PEGDA to fabricate high-aspect-ratio microneedles. *RSC Adv* **12**, 9550–9555 (2022).
131. O'Brien, F. J. Biomaterials & scaffolds for tissue engineering. *Materials Today* **14**, 88–95 (2011).
132. Wang, P. *et al.* Electron beam melted heterogeneously porous microlattices for metallic bone applications: Design and investigations of boundary and edge effects. *Addit Manuf* **36**, 101566 (2020).
133. Coenen, A. M. J., Bernaerts, K. V., Harings, J. A. W., Jockenhoevel, S. & Ghazanfari, S. Elastic materials for tissue engineering applications: Natural, synthetic, and hybrid polymers. *Acta Biomater* **79**, 60–82 (2018).
134. Zhang, X. *et al.* Integrating valve-inspired design features into poly(ethylene glycol) hydrogel scaffolds for heart valve tissue engineering. *Acta Biomater* **14**, 11–21 (2015).
135. Rho, J. Y., Ashman, R. B. & Turner, C. H. Young's modulus of trabecular and cortical bone material: Ultrasonic and microtensile measurements. *J Biomech* **26**, 111–119 (1993).
136. A, K. & A, L. Mechanical Behaviour of Skin: A Review. *Journal of Material Science & Engineering* **5**, (2016).

137. Liu, J., Zheng, H., Poh, P., Machens, H.-G. & Schilling, A. Hydrogels for Engineering of Perfusable Vascular Networks. *Int J Mol Sci* **16**, 15997–16016 (2015).
138. Moutos, F. T., Freed, L. E. & Guilak, F. A biomimetic three-dimensional woven composite scaffold for functional tissue engineering of cartilage. *Nat Mater* **6**, 162–167 (2007).
139. COURTNEY, T., SACKS, M., STANKUS, J., GUAN, J. & WAGNER, W. Design and analysis of tissue engineering scaffolds that mimic soft tissue mechanical anisotropy. *Biomaterials* (2006) doi:10.1016/j.biomaterials.2006.02.024.
140. Hollister, S. J. Porous scaffold design for tissue engineering. *Nat Mater* **4**, 518–524 (2005).
141. Bracaglia, L. G. *et al.* 3D printing for the design and fabrication of polymer-based gradient scaffolds. *Acta Biomater* **56**, 3–13 (2017).
142. Wu, D., Isaksson, P., Ferguson, S. J. & Persson, C. Young's modulus of trabecular bone at the tissue level: A review. *Acta Biomater* **78**, 1–12 (2018).
143. Kim, H. Y. & Miyazaki, S. Unique Properties of Metastable Beta Ti Alloys Related to Martensitic Transformation. in *Ni-Free Ti-Based Shape Memory Alloys* 147–180 (Elsevier, 2018). doi:10.1016/B978-0-12-809401-3.00005-7.
144. Vaidya, A. & Pathak, K. Mechanical stability of dental materials. in *Applications of Nanocomposite Materials in Dentistry* 285–305 (Elsevier, 2019). doi:10.1016/B978-0-12-813742-0.00017-1.
145. Hu, T. *et al.* 3D-printable supramolecular hydrogels with shear-thinning property: fabricating strength tunable bioink via dual crosslinking. *Bioact Mater* **5**, 808–818 (2020).
146. Dai, W. *et al.* 3D Bioprinting of Heterogeneous Constructs Providing Tissue-Specific Microenvironment Based on Host–Guest Modulated Dynamic Hydrogel Bioink for Osteochondral Regeneration. *Adv Funct Mater* **32**, (2022).
147. Ko, Y.-G. & Kwon, O. H. Reinforced gelatin-methacrylate hydrogels containing poly(lactic-co-glycolic acid) nanofiber fragments for 3D bioprinting. *Journal of Industrial and Engineering Chemistry* **89**, 147–155 (2020).
148. Morris, V. B., Nimbalkar, S., Younesi, M., McClellan, P. & Akkus, O. Mechanical Properties, Cytocompatibility and Manufacturability of Chitosan:PEGDA Hybrid-Gel Scaffolds by Stereolithography. *Ann Biomed Eng* **45**, 286–296 (2017).
149. Dai, W. *et al.* 3D Bioprinting of Heterogeneous Constructs Providing Tissue-Specific Microenvironment Based on Host–Guest Modulated Dynamic Hydrogel Bioink for Osteochondral Regeneration. *Adv Funct Mater* **32**, (2022).

150. Zennifer, A., Manivannan, S., Sethuraman, S., Kumbar, S. G. & Sundaramurthi, D. 3D bioprinting and photocrosslinking: emerging strategies & future perspectives. *Biomaterials Advances* **134**, 112576 (2022).
151. Li, X., Sun, Q., Li, Q., Kawazoe, N. & Chen, G. Functional Hydrogels With Tunable Structures and Properties for Tissue Engineering Applications. *Front Chem* **6**, (2018).
152. Terborgh, J., Ladd, K. V. & McLeod, G. C. Low Energy Effects of Light on Growth and Pigment Content in a Yellow-in-the-Dark Mutant of *Chlamydomonas reinhardi*. *Plant Physiol* **42**, 1665–1672 (1967).
153. Gilpin, A. & Yang, Y. Decellularization Strategies for Regenerative Medicine: From Processing Techniques to Applications. *Biomed Res Int* **2017**, 1–13 (2017).
154. Yang, J., Xu, Y., Luo, S., Dang, H. & Cao, M. Effect of cryoprotectants on rat kidney decellularization by freeze-thaw process. *Cryobiology* **105**, 71–82 (2022).
155. Abasalizadeh, F. *et al.* Alginate-based hydrogels as drug delivery vehicles in cancer treatment and their applications in wound dressing and 3D bioprinting. *Journal of Biological Engineering* vol. 14 Preprint at https://doi.org/10.1186/s13036-020-0227-7 (2020).
156. Pjura, P. E., Grzeskowiak, K. & Dickerson, R. E. Binding of Hoechst 33258 to the minor groove of B-DNA. *J Mol Biol* **197**, 257–271 (1987).
157. Forry, S. P., Reyes, D. R., Gaitan, M. & Locascio, L. E. Cellular Immobilization within Microfluidic Microenvironments: Dielectrophoresis with Polyelectrolyte Multilayers. *J Am Chem Soc* **128**, 13678–13679 (2006).
158. Custódio, C. A., Reis, R. L. & Mano, J. F. Engineering Biomolecular Microenvironments for Cell Instructive Biomaterials. *Adv Healthc Mater* **3**, 797–810 (2014).
159. Chaudhari, A. *et al.* Future Prospects for Scaffolding Methods and Biomaterials in Skin Tissue Engineering: A Review. *Int J Mol Sci* **17**, 1974 (2016).
160. Elviri, L., Bianchera, A., Bergonzi, C. & Bettini, R. Controlled local drug delivery strategies from chitosan hydrogels for wound healing. *Expert Opin Drug Deliv* **14**, 897–908 (2017).
161. Ji, S. & Guvendiren, M. Complex 3D bioprinting methods. *APL Bioeng* **5**, (2021).
162. Ozbolat, I. T., Peng, W. & Ozbolat, V. Application areas of 3D bioprinting. *Drug Discov Today* **21**, 1257–1271 (2016).
163. Tytgat, L. *et al.* Evaluation of 3D Printed Gelatin-Based Scaffolds with Varying Pore Size for MSC-Based Adipose Tissue Engineering. *Macromol Biosci* **20**, (2020).

164. Freyman, T. M., Yannas, I. V. & Gibson, L. J. Cellular materials as porous scaffolds for tissue engineering. *Prog Mater Sci* **46**, 273–282 (2001).
165. O'Brien, F. J. Biomaterials & scaffolds for tissue engineering. *Materials Today* **14**, 88–95 (2011).
166. Byrne, D. P., Lacroix, D., Planell, J. A., Kelly, D. J. & Prendergast, P. J. Simulation of tissue differentiation in a scaffold as a function of porosity, Young's modulus and dissolution rate: Application of mechanobiological models in tissue engineering. *Biomaterials* **28**, 5544–5554 (2007).
167. Vatankhah, E. *et al.* Artificial neural network for modeling the elastic modulus of electrospun polycaprolactone/gelatin scaffolds. *Acta Biomater* **10**, 709–721 (2014).
168. Zhao, X. *et al.* Photocrosslinkable Gelatin Hydrogel for Epidermal Tissue Engineering. *Adv Healthc Mater* **5**, 108–118 (2016).
169. Schmedlen, R. H., Masters, K. S. & West, J. L. Photocrosslinkable polyvinyl alcohol hydrogels that can be modified with cell adhesion peptides for use in tissue engineering. *Biomaterials* **23**, 4325–4332 (2002).
170. Zhao, X. Multi-scale multi-mechanism design of tough hydrogels: building dissipation into stretchy networks. *Soft Matter* **10**, 672–687 (2014).
171. Sun, J.-Y. *et al.* Highly stretchable and tough hydrogels. *Nature* **489**, 133–136 (2012).
172. Caddeo, S., Boffito, M. & Sartori, S. Tissue Engineering Approaches in the Design of Healthy and Pathological In Vitro Tissue Models. *Front Bioeng Biotechnol* **5**, (2017).
173. Khalili, A. & Ahmad, M. A Review of Cell Adhesion Studies for Biomedical and Biological Applications. *Int J Mol Sci* **16**, 18149–18184 (2015).
174. Taubenberger, A. V., Hutmacher, D. W. & Muller, D. J. Single-Cell Force Spectroscopy, an Emerging Tool to Quantify Cell Adhesion to Biomaterials. *Tissue Eng Part B Rev* **20**, 40–55 (2014).
175. Bettahalli, N. M. S., Arkesteijn, I. T. M., Wessling, M., Poot, A. A. & Stamatialis, D. Corrugated round fibers to improve cell adhesion and proliferation in tissue engineering scaffolds. *Acta Biomater* **9**, 6928–6935 (2013).
176. Carpenter, C. L. Actin cytoskeleton and cell signaling. *Crit Care Med* **28**, N94–N99 (2000).
177. Miyoshi, H. & Adachi, T. Topography Design Concept of a Tissue Engineering Scaffold for Controlling Cell Function and Fate Through Actin Cytoskeletal Modulation. *Tissue Eng Part B Rev* **20**, 609–627 (2014).

178. Dado, D. & Levenberg, S. Cell–scaffold mechanical interplay within engineered tissue. *Semin Cell Dev Biol* **20**, 656–664 (2009).
179. Hutmacher, D. W. Scaffolds in tissue engineering bone and cartilage. *Biomaterials* **21**, 2529–2543 (2000).
180. Mazeau, K. & Wyszomirski, M. Modelling of Congo red adsorption on the hydrophobic surface of cellulose using molecular dynamics. *Cellulose* **19**, 1495–1506 (2012).
181. Yakupova, E. I., Bobyleva, L. G., Vikhlyantsev, I. M. & Bobylev, A. G. Congo Red and amyloids: history and relationship. *Biosci Rep* **39**, (2019).
182. Colvin, J. R. & Witter, D. E. Congo red and calcofluor white inhibition ofAcetobacter xylinum cell growth and of bacterial cellulose microfibril formation: Isolation and properties of a transient, extracellular glucan related to cellulose. *Protoplasma* **116**, 34–40 (1983).
183. Reichhardt, C. *et al.* Influence of the amyloid dye Congo red on curli, cellulose, and the extracellular matrix in E. coli during growth and matrix purification. *Anal Bioanal Chem* **408**, 7709–7717 (2016).
184. Samiey, B. & Dargahi, M. Kinetics and thermodynamics of adsorption of congo red on cellulose. *Open Chem* **8**, 906–912 (2010).
185. Robb, K. P., Shridhar, A. & Flynn, L. E. Decellularized Matrices As Cell-Instructive Scaffolds to Guide Tissue-Specific Regeneration. *ACS Biomater Sci Eng* **4**, 3627–3643 (2018).
186. Zhang, H., Zhou, L. & Zhang, W. Control of Scaffold Degradation in Tissue Engineering: A Review. *Tissue Eng Part B Rev* **20**, 492–502 (2014).
187. Intini, C. *et al.* 3D-printed chitosan-based scaffolds: An in vitro study of human skin cell growth and an in-vivo wound healing evaluation in experimental diabetes in rats. *Carbohydr Polym* **199**, 593–602 (2018).
188. Lee, K.-W., Wang, S., Dadsetan, M., Yaszemski, M. J. & Lu, L. Enhanced Cell Ingrowth and Proliferation through Three-Dimensional Nanocomposite Scaffolds with Controlled Pore Structures. *Biomacromolecules* **11**, 682–689 (2010).
189. Chung, C. A., Yang, C. W. & Chen, C. W. Analysis of cell growth and diffusion in a scaffold for cartilage tissue engineering. *Biotechnol Bioeng* **94**, 1138–1146 (2006).
190. Zhao, C., Tan, A., Pastorin, G. & Ho, H. K. Nanomaterial scaffolds for stem cell proliferation and differentiation in tissue engineering. *Biotechnol Adv* **31**, 654–668 (2013).

191. Uyar, T. *et al.* Segmentation of live and dead cells in tissue scaffolds. in *2018 26th Signal Processing and Communications Applications Conference (SIU)* 1–4 (IEEE, 2018). doi:10.1109/SIU.2018.8404384.
192. Caddeo, S., Boffito, M. & Sartori, S. Tissue Engineering Approaches in the Design of Healthy and Pathological In Vitro Tissue Models. *Front Bioeng Biotechnol* **5**, (2017).
193. Gangolphe, L. *et al.* Electrospun microstructured PLA-based scaffolds featuring relevant anisotropic, mechanical and degradation characteristics for soft tissue engineering. *Materials Science and Engineering C* **129**, (2021).
194. Jing, L. *et al.* Engineered Nanotopography on the Microfibers of 3D-Printed PCL Scaffolds to Modulate Cellular Responses and Establish an *In Vitro* Tumor Model. *ACS Appl Bio Mater* **4**, 1381–1394 (2021).
195. Asim, M. H. *et al.* S-protected thiolated hyaluronic acid: In-situ crosslinking hydrogels for 3D cell culture scaffold. *Carbohydr Polym* **237**, 116092 (2020).
196. Jing, L., Sun, J., Liu, H., Wang, X. & Huang, D. Using Plant Proteins to Develop Composite Scaffolds for Cell Culture Applications. *Int J Bioprint* **7**, 298 (2020).
197. Nowroozi, N., Faraji, S., Nouralishahi, A. & Shahrousvand, M. Biological and structural properties of graphene oxide/curcumin nanocomposite incorporated chitosan as a scaffold for wound healing application. *Life Sci* **264**, 118640 (2021).
198. Shi, J. *et al.* Incorporating Protein Gradient into Electrospun Nanofibers As Scaffolds for Tissue Engineering. *ACS Appl Mater Interfaces* **2**, 1025–1030 (2010).
199. Faucheux, N., Warocquier-Cl&#65533;rout, R., Haye, B. & Nagel, M. D. Cyclic AMP in cells adhering to bioincompatible (Cuprophan) and biocompatible (AN69) substrates. *J Biomed Mater Res* **39**, 506–510 (1998).
200. Li, X. *et al.* Effects of aligned and random fibers with different diameter on cell behaviors. *Colloids Surf B Biointerfaces* **171**, 461–467 (2018).
201. Dede Eren, A. *et al.* Cells Dynamically Adapt to Surface Geometry by Remodeling Their Focal Adhesions and Actin Cytoskeleton. *Front Cell Dev Biol* **10**, (2022).
202. Lema, C., Varela-Ramirez, A. & Aguilera, R. J. Differential nuclear staining assay for high-throughput screening to identify cytotoxic compounds. *Curr Cell Biochem* **1**, 1–14 (2011).
203. Lee, H. M. & Fischer, K. M. Cost-effective synthesis of polyethylene glycol diacrylate-acrylic acid (PEGDA-AA), a tissue engineering hydrogel ideal for C2C12 mouse muscle cells. *The FASEB Journal* **33**, (2019).

204. Li, W. *et al.* Highly interconnected inverse opal extracellular matrix scaffolds enhance stem cell therapy in limb ischemia. *Acta Biomater* **128**, 209–221 (2021).
205. Liebschner, M. A. K. Biomechanical considerations of animal models used in tissue engineering of bone. *Biomaterials* **25**, 1697–1714 (2004).
206. Rashid, S. T., Salacinski, H. J., Hamilton, G. & Seifalian, A. M. The use of animal models in developing the discipline of cardiovascular tissue engineering: a review. *Biomaterials* **25**, 1627–1637 (2004).
207. Bédard, P. *et al.* Innovative Human Three-Dimensional Tissue-Engineered Models as an Alternative to Animal Testing. *Bioengineering* **7**, 115 (2020).
208. Hubrecht & Carter. The 3Rs and Humane Experimental Technique: Implementing Change. *Animals* **9**, 754 (2019).
209. Blakemore, C., Clark, J. M., Nevalainen, T., Oberdorfer, M. & Sussman, A. Implementing the 3Rs in Neuroscience Research: A Reasoned Approach. *Neuron* **75**, 948–950 (2012).
210. Sneddon, L. U., Halsey, L. G. & Bury, N. R. Considering aspects of the 3Rs principles within experimental animal biology. *Journal of Experimental Biology* **220**, 3007–3016 (2017).
211. Herrmann, K. Beyond the 3Rs: Expanding the use of human-relevant replacement methods in biomedical research. *ALTEX* 343–352 (2019) doi:10.14573/altex.1907031.
212. Jin, I. S. *et al.* Replacement techniques to reduce animal experiments in drug and nanoparticle development. *J Pharm Investig* **50**, 327–335 (2020).
213. Langley, G., Evans, T., Holgate, S. T. & Jones, A. Replacing animal experiments: choices, chances and challenges. *BioEssays* **29**, 918–926 (2007).
214. Ribitsch, I. *et al.* Large Animal Models in Regenerative Medicine and Tissue Engineering: To Do or Not to Do. *Front Bioeng Biotechnol* **8**, (2020).
215. de Vries, R. B. M., Buma, P., Leenaars, M., Ritskes-Hoitinga, M. & Gordijn, B. Reducing the Number of Laboratory Animals Used in Tissue Engineering Research by Restricting the Variety of Animal Models. Articular Cartilage Tissue Engineering as a Case Study. *Tissue Eng Part B Rev* **18**, 427–435 (2012).
216. Jennings, M. *et al.* Refinements in husbandry, care and common procedures for non-human primates. *Lab Anim* **43**, 1–47 (2009).
217. Hawkins, P. Refining Housing, Husbandry and Care for Animals Used in Studies Involving Biotelemetry. *Animals* **4**, 361–373 (2014).
218. Anderson, D. K. *et al.* Delayed grafting of fetal CNS tissue into chronic compression lesions of the adult cat spinal cord. *Restor Neurol Neurosci* **2**, 309–325 (1991).

219. Sill, B., Alpatov, I. V., Pacak, C. A. & Cowan, D. B. Implantation of Engineered Tissue in the Rat Heart. *Journal of Visualized Experiments* (2009) doi:10.3791/1139.

220. Guo, Y. *et al.* A simple semi-quantitative approach studying the in vivo degradation of regenerated silk fibroin scaffolds with different pore sizes. *Materials Science and Engineering: C* **79**, 161–167 (2017).

221. Wang, Y. *et al.* 3D-Printing of succulent plant-like scaffolds with beneficial cell microenvironments for bone regeneration. *J Mater Chem B* **11**, 5523–5536 (2023).

222. Zheng Shu, X., Liu, Y., Palumbo, F. S., Luo, Y. & Prestwich, G. D. In situ crosslinkable hyaluronan hydrogels for tissue engineering. *Biomaterials* **25**, 1339–1348 (2004).

223. LaFollette, M. R., O'Haire, M. E., Cloutier, S., Blankenberger, W. B. & Gaskill, B. N. Rat tickling: A systematic review of applications, outcomes, and moderators. *PLoS One* **12**, e0175320 (2017).

224. Fischer, A. H., Jacobson, K. A., Rose, J. & Zeller, R. Hematoxylin and Eosin Staining of Tissue and Cell Sections. *Cold Spring Harb Protoc* **2008**, pdb.prot4986 (2008).

225. Gruber, H. E. Adaptations of Goldner's Masson Trichrome Stain for the Study of Undecalcified Plastic Embedded Bone. *Biotechnic & Histochemistry* **67**, 30–34 (1992).

226. Smith, D. J. Improved Masson Trichrome Stain on Plastic-Embedded Tissue. *J Histotechnol* **4**, 132–133 (1981).

227. Pouyandeh Ravan, A., Ghasemi Basir, H. R., Taheri Azandaryani, M., Azizi, A. & Goudarzi, F. Role of Vaccinium arctostaphylos extract on CCl4-induced chronic liver fibrosis in rats. *Comp Clin Path* **29**, 1051–1060 (2020).

228. Shin, H.-M. *et al.* Characterization of Monoclonal Antibodies against Human Leukocyte Common Antigen (CD45). *Immune Netw* **11**, 114 (2011).

229. Piali, L. *et al.* CD31/PECAM-1 is a ligand for alpha v beta 3 integrin involved in adhesion of leukocytes to endothelium. *J Cell Biol* **130**, 451–460 (1995).

230. Newton, J. P., Hunter, A. P., Simmons, D. L., Buckley, C. D. & Harvey, D. J. CD31 (PECAM-1) Exists as a Dimer and Is Heavily N-Glycosylated. *Biochem Biophys Res Commun* **261**, 283–291 (1999).

231. Hou, Y. *et al.* Photo-Cross-Linked PDMS $_{star}$ -PEG Hydrogels: Synthesis, Characterization, and Potential Application for Tissue Engineering Scaffolds. *Biomacromolecules* **11**, 648–656 (2010).

232. Yang, S., Wang, J., Tan, H., Zeng, F. & Liu, C. Mechanically robust PEGDA–MSNs-OH nanocomposite hydrogel with hierarchical meso-macroporous structure for tissue engineering. *Soft Matter* **8**, 8981 (2012).

233. Sun, D., Liu, W., Tang, A., Guo, F. & Xie, W. A new PEGDA/CNF aerogel-wet hydrogel scaffold fabricated by a two-step method. *Soft Matter* **15**, 8092–8101 (2019).
234. Brodbeck, W. G. & Anderson, J. M. Giant cell formation and function. *Curr Opin Hematol* **16**, 53–57 (2009).
235. Miron, R. J. & Bosshardt, D. D. Multinucleated Giant Cells: Good Guys or Bad Guys? *Tissue Eng Part B Rev* **24**, 53–65 (2018).
236. Chan, J. K. C. The Wonderful Colors of the Hematoxylin–Eosin Stain in Diagnostic Surgical Pathology. *Int J Surg Pathol* **22**, 12–32 (2014).
237. Fischer, A. H., Jacobson, K. A., Rose, J. & Zeller, R. Hematoxylin and Eosin Staining of Tissue and Cell Sections. *Cold Spring Harb Protoc* **2008**, pdb.prot4986 (2008).
238. de Haan, K. *et al.* Deep learning-based transformation of H&E stained tissues into special stains. *Nat Commun* **12**, 4884 (2021).
239. Greigert, H., Genet, C., Ramon, A., Bonnotte, B. & Samson, M. New Insights into the Pathogenesis of Giant Cell Arteritis: Mechanisms Involved in Maintaining Vascular Inflammation. *J Clin Med* **11**, 2905 (2022).
240. Seib, F. P., Berry, J. E., Shiozawa, Y., Taichman, R. S. & Kaplan, D. L. Tissue engineering a surrogate niche for metastatic cancer cells. *Biomaterials* **51**, 313–319 (2015).
241. Brelle, L. *et al.* Biocompatible Semi-Interpenetrating Materials Based on Poly(3-hydroxyalkanoate)s and Poly(ethyleneglycol) Diacrylate. *Gels* **8**, 632 (2022).
242. Rekowska, N. *et al.* Thermal, Mechanical and Biocompatibility Analyses of Photochemically Polymerized PEGDA250 for Photopolymerization-Based Manufacturing Processes. *Pharmaceutics* **14**, 628 (2022).
243. Rekowska, N. *et al.* Biocompatibility and thermodynamic properties of PEGDA and two of its copolymer. in *2019 41st Annual International Conference of the IEEE Engineering in Medicine and Biology Society (EMBC)* 1093–1096 (IEEE, 2019). doi:10.1109/EMBC.2019.8857503.
244. Warr, C. *et al.* Biocompatible PEGDA Resin for 3D Printing. *ACS Appl Bio Mater* **3**, 2239–2244 (2020).
245. Choi, J. R., Yong, K. W., Choi, J. Y. & Cowie, A. C. Recent Advances in Photo-Crosslinkable Hydrogels for Biomedical Applications. *Biotechniques* **66**, 40–53 (2019).
246. Daamen, W. F. *et al.* Tissue response of defined collagen–elastin scaffolds in young and adult rats with special attention to calcification. *Biomaterials* **26**, 81–92 (2005).

247. Wang, X. *et al.* Biofabrication of poly(l-lactide-co-ε-caprolactone)/silk fibroin scaffold for the application as superb anti-calcification tissue engineered prosthetic valve. *Materials Science and Engineering: C* **121**, 111872 (2021).
248. Hernandez, J. L. & Woodrow, K. A. Medical Applications of Porous Biomaterials: Features of Porosity and Tissue-Specific Implications for Biocompatibility. *Adv Healthc Mater* **11**, (2022).
249. Rolfe, B. *et al.* The Fibrotic Response to Implanted Biomaterials: Implications for Tissue Engineering. in *Regenerative Medicine and Tissue Engineering - Cells and Biomaterials* (InTech, 2011). doi:10.5772/21790.
250. Ifkovits, J. L. *et al.* Biodegradable Fibrous Scaffolds with Tunable Properties Formed from Photo-Cross-Linkable Poly(glycerol sebacate). *ACS Appl Mater Interfaces* **1**, 1878–1886 (2009).
251. Naito, H., Iba, T. & Takakura, N. Mechanisms of new blood-vessel formation and proliferative heterogeneity of endothelial cells. *Int Immunol* **32**, 295–305 (2020).
252. Melero-Martin, J. M. *et al.* In vivo vasculogenic potential of human blood-derived endothelial progenitor cells. *Blood* **109**, 4761–4768 (2007).
253. Stefanovic, B. <scp>RNA</scp> protein interactions governing expression of the most abundant protein in human body, type I collagen. *WIREs RNA* **4**, 535–545 (2013).
254. Mathew-Steiner, S. S., Roy, S. & Sen, C. K. Collagen in Wound Healing. *Bioengineering* **8**, 63 (2021).
255. Nyström, A. *et al.* Collagen VII plays a dual role in wound healing. *Journal of Clinical Investigation* **123**, 3498–3509 (2013).
256. Schönborn, K. *et al.* Role of collagen XII in skin homeostasis and repair. *Matrix Biology* **94**, 57–76 (2020).
257. Wang, H. *et al.* An Overview of Extracellular Matrix-Based Bioinks for 3D Bioprinting. *Front Bioeng Biotechnol* **10**, (2022).
258. Barker, T. H. *et al.* Matricellular Homologs in the Foreign Body Response. *Am J Pathol* **166**, 923–933 (2005).
259. Mazzoccoli, J. P., Feke, D. L., Baskaran, H. & Pintauro, P. N. Mechanical and cell viability properties of crosslinked low- and high-molecular weight poly(ethylene glycol) diacrylate blends. *J Biomed Mater Res A* **93A**, 558–566 (2010).
260. Mazzoccoli, J. P., Feke, D. L., Baskaran, H. & Pintauro, P. N. Mechanical and cell viability properties of crosslinked low- and high-molecular weight poly(ethylene glycol) diacrylate blends. *J Biomed Mater Res A* **93A**, 558–566 (2010).

261. Morris, V. B., Nimbalkar, S., Younesi, M., McClellan, P. & Akkus, O. Mechanical Properties, Cytocompatibility and Manufacturability of Chitosan:PEGDA Hybrid-Gel Scaffolds by Stereolithography. *Ann Biomed Eng* **45**, 286–296 (2017).
262. Tang, A. *et al.* Nanocellulose/PEGDA aerogel scaffolds with tunable modulus prepared by stereolithography for three-dimensional cell culture. *J Biomater Sci Polym Ed* **30**, 797–814 (2019).
263. Wang, C. *et al.* Cryogenic 3D printing of dual-delivery scaffolds for improved bone regeneration with enhanced vascularization. *Bioact Mater* **6**, 137–145 (2021).
264. Do, A., Khorsand, B., Geary, S. M. & Salem, A. K. 3D Printing of Scaffolds for Tissue Regeneration Applications. *Adv Healthc Mater* **4**, 1742–1762 (2015).
265. Nie, Y. *et al.* In vitro and 48 weeks in vivo performances of 3D printed porous Fe-30Mn biodegradable scaffolds. *Acta Biomater* **121**, 724–740 (2021).
266. Lin, W. *et al.* Long-term in vivo corrosion behavior, biocompatibility and bioresorption mechanism of a bioresorbable nitrided iron scaffold. *Acta Biomater* **54**, 454–468 (2017).
267. Kulke, M., Geist, N., Friedrichs, W. & Langel, W. Molecular dynamics simulations on networks of heparin and collagen. *Proteins: Structure, Function, and Bioinformatics* **85**, 1119–1130 (2017).
268. Caballé-Serrano, J., Zhang, S., Sculean, A., Staehli, A. & Bosshardt, D. D. Tissue Integration and Degradation of a Porous Collagen-Based Scaffold Used for Soft Tissue Augmentation. *Materials* **13**, 2420 (2020).
269. Tenkumo, T. *et al.* Prolonged release of bone morphogenetic protein-2 in vivo by gene transfection with DNA-functionalized calcium phosphate nanoparticle-loaded collagen scaffolds. *Materials Science and Engineering: C* **92**, 172–183 (2018).
270. Meagher, M. J. *et al.* Acellular hydroxyapatite-collagen scaffolds support angiogenesis and osteogenic gene expression in an ectopic murine model: Effects of hydroxyapatite volume fraction. *J Biomed Mater Res A* **104**, 2178–2188 (2016).
271. Das, P., DiVito, M. D., Wertheim, J. A. & Tan, L. P. Collagen-I and fibronectin modified three-dimensional electrospun PLGA scaffolds for long-term in vitro maintenance of functional hepatocytes. *Materials Science and Engineering: C* **111**, 110723 (2020).
272. Akar, B. *et al.* Large Animal Models of an *In Vivo* Bioreactor for Engineering Vascularized Bone. *Tissue Eng Part B Rev* **24**, 317–325 (2018).
273. Ribitsch, I. *et al.* Large Animal Models in Regenerative Medicine and Tissue Engineering: To Do or Not to Do. *Front Bioeng Biotechnol* **8**, (2020).

274. Slotkin, J. R. *et al.* Biodegradable scaffolds promote tissue remodeling and functional improvement in non-human primates with acute spinal cord injury. *Biomaterials* **123**, 63–76 (2017).

275. Chanchareonsook, N. *et al.* Segmental mandibular bone reconstruction with a carbonate-substituted hydroxyapatite-coated modular endoprosthetic poly(ε-caprolactone) scaffold in *Macaca fascicularis*. *J Biomed Mater Res B Appl Biomater* **102**, 962–976 (2014).

276. Alcazar, C. A., Hu, C., Rando, T. A., Huang, N. F. & Nakayama, K. H. Transplantation of insulin-like growth factor-1 laden scaffolds combined with exercise promotes neuroregeneration and angiogenesis in a preclinical muscle injury model. *Biomater Sci* **8**, 5376–5389 (2020).

277. Quinlan, E. *et al.* Hypoxia-mimicking bioactive glass/collagen glycosaminoglycan composite scaffolds to enhance angiogenesis and bone repair. *Biomaterials* **52**, 358–366 (2015).

278. Kang, M. S., Kim, J.-H., Singh, R. K., Jang, J.-H. & Kim, H.-W. Therapeutic-designed electrospun bone scaffolds: Mesoporous bioactive nanocarriers in hollow fiber composites to sequentially deliver dual growth factors. *Acta Biomater* **16**, 103–116 (2015).

279. Kanczler, J. M. *et al.* The effect of mesenchymal populations and vascular endothelial growth factor delivered from biodegradable polymer scaffolds on bone formation. *Biomaterials* **29**, 1892–1900 (2008).